University of Sheffield

Development of Osteoinductive Coatings for Spinal Implants (Fusion Cages)

José Rui Oliveira Rodrigues

A thesis submitted in partial fulfilment of the requirements for the degree of Doctor of Philosophy

The University of Sheffield
Faculty of Engineering
Department of Materials Science and Engineering

November 2022

Abstract

When conservative treatment fails for more than two years, patients suffering from lower back pain might be subject to spine fusion surgery. The procedure's high chances for post-operative complications explain why it is used as a last resort. If early integration of the fusion cage is achieved, the probability of postoperative complications is lowered. This thesis aimed to improve the osteointegration of spinal fusion cages by developing an osteoinductive coating based on sol-gel chemistry and composed of TiO_2 and Mg and Sr-substituted hydroxyapatite (sHAP).

To reduce variability during the project, the *in vitro* culture of mesenchymal stem cells (MSCs) in serum-free media (SFM) was studied. One commercially available SFM outperformed standard culture conditions and specialised media containing human serum. Changing media once a week was enough for immortalised MSCs to become confluent in 7 days and start showing signs of differentiation in 14 days when cultured in osteogenic media.

Using design of experiments (DoE), the synthesis conditions of Mg and Sr sHAP were optimised, enhancing sHAP's osteogenic potential. The best-performing formulation, synthesised with 10% Mg and 5% Sr substitutions, and 15 ml of ammonia for pH control, significantly increased alkaline phosphatase (ALP) activity in MSCs compared to commercially available sHAP. DoE was also used to improve the synthesis of TiO_2 through sol-gel chemistry, allowing crystallisation at sintering temperatures sustainable by PEEK during the coating process. With optimal reaction temperature, sintering time, and the correct ratio between solvent, reagents, and peptising agent, TiO_2 can reach up to 80% crystallinity when sintered at 250°C.

Finally, this thesis found that a TiO_2/HAP coating can increase the osteogenic potential of different substrates. Using DoE, the optimal coating conditions were found to include the deposition of 5 layers of a TiO_2/sHAP composite, a short and fast dipping process, and a faster heating step during sintering.

Acknowledgements

This work would have not been possible without the support of many individuals, who directly or indirectly helped me get through this arduous but rewarding journey. To start, I would like to thank my supervisors, Prof. Frederik Claeyssens and Prof. Gwen Reilly, for their supervision, guidance, and support during the entirety of my PhD. Thank you for giving me this opportunity, believing in me and wanting me to succeed.

To everyone involved in the SPINNER project, thank you for financing and organising this project, without which none of this work would have been possible. In particular, I want to thank Dr Norman Powell for keeping the machine running and always being available to help whenever it was needed. To the people at Finceramica, particularly Laura Grillini, Riccardo Bendoni, Lucia Forte and Claudio De Luca, thank you for hosting me for 15 months, for your help and for your insight. And to all the ESRs, Denata, Chloé, Jennifer, Marco and Cameron, thank you for the memories and for the support. We truly were in this together.

To everyone at the University of Sheffield, INSIGNEO and IMSB, thank you for expanding my horizons and for making me want to keep learning more. There are too many names to list, but in particular, I want to thank everyone that was a part of Gwen's group, Fred's group, and the C+ 13 and 14 offices, for being with me on this journey, especially when we all just needed to relax and socialise. Thank you for making my time in Sheffield much more interesting.

To all my friends back at home, Anaísa, Catarina and Vanessa, Duarte, Daniela, Lisete, Elsa and Cláudia, Júnior, Xana and Dory. Thank you for keeping me sane even at a distance. Couldn't have done it without your friendship and your support.

To all my family, thank you for all the support you gave me, and my brother, during my time abroad. Particularly, I want to thank my aunt, Mena, for checking on me every single day I am not home. I also want to thank all my cousins, especially Ana, Maria João, Cris, Dudah, Jay, Jö and Afonso, and Salvador, Carlinhos and Clarinha, the young ones, for your love and for being as marvellously chaotic as ever.

To my brother, Gerardo, thank you for holding the fort while I am gone. I could have not done this without knowing our home was in good hands. Know that I am proud of you and that I love you.

Finally, to my parents, thank you for all you taught me, for all you gave me, for all your care and for all your love. Words cannot express how much I miss you both. My only hope is that I have made you proud.

"Enquanto houver estrada pra andar, a gente vai continuar."

- Jorge Palma, in "A gente vai continuar"

Table of Contents

List of Figures

List of Tables

List of Equations

Abbreviations

ACF	Animal component-free
AcOH	Acetic Acid
ALIF	Anterior Lumbar Interbody Fusion
ALP	Alkaline Phosphatase
ANOVA	Analysis of Variance
BAK	Bagby and Kuslich
CAB	Cell assay buffer
CCD	Central composite design
CD	Chemically defined
CDB	Cell digestion buffer
CDM	Chemically defined media
CFU-F	Fibroblastic colony-forming units
DALY	Disability-adjusted life years
DMEM	Dulbecco's Modified Eagle Medium
DNA	Deoxyribonucleic acid
DoE	Design of Experiments
DSC	Differential scanning calorimetry
DSD	Definitive screening design
EM	Expansion Media
EtOH	Ethanol
FBS	Foetal bovine serum
FDA	Food and Drugs Administration
FFD	Full factorial design
FTIR	Fourier-transformed infrared
GBP	Great british pound
HAP	Hydroxyapatite
HBSS	Hank's balanced salt solution
hTERT-MSC	Human-telomerase immortalised mesenchymal stem cell

LBP	Lower back pain
LLIF	Lateral lombar interbody fusion
MSC	Mesenchymal stem cell
NSAID	Non-steroidal anti-inflammatory drug
OM	Osteogenic media
PEEK	Polyether ether ketone
PLIF	Posterior lumbar interbody fusion
pNP	p-Nitrophenol
pNPP	p-Nitrophenyl Phosphate
PRESS	Predicted residual error sum of squares
PS	Penicillin-Streptomycin
PSG	Penicillin-Streptomycin-Glutamine
rcf	Relative centrifuge force
rpm	Revolutions per minute
SF	Serum-free
SFM	Serum-free media
sHAP	Substituted hydroxyapatite
TGA	Thermogravimetral analysis
TLIF	Transforaminal Lumbar Interbody Fusion
TTIP	Titanium isopropoxide
UK	United Kingdom
USA	United States of America
USD	United States dollar
XF	Xeno-free
XRD	X-ray diffraction
YLD	Years lived with disability
α-MEM	Minimum Essential Medium α

I. Introduction

As the average populational age increases, so does the global impact of musculoskeletal disorders, even in developing countries. In fact, by 2019 musculoskeletal disorders were the leading cause of disability worldwide, being responsible for approximately two-thirds of the total years lived with disability [1] (YLD, a metric defined by the number of years a patient lives with a medical condition [2, 3]). In terms of total global disability-adjusted life years (DALY, a metric that estimates the burden of a medical condition as causes of both disability and premature death [3, 4]), musculoskeletal diseases rank tenth in global burden, being the cause of approximately 3% of all DALY [5].

If we look at individual disorders, however, we can identify that, in 2019, lower back pain (LBP) was the leading cause of YLD (approximately 20.6% of YLD) and ninth in terms of DALY (2–2.5% of DALY). Also in 2019, it was estimated that the age-standardised prevalence of LBP was 7%, with it being higher the older the age group is. [1, 5, 6]. LBP is also common during childhood, with studies showing that 37% of adolescents in 28 countries suffered from LBP at least once per month, being slightly more common in girls than boys. Adolescents that suffered from LBP are also twice more likely to develop LBP as adults [7]. From a public health level, disability adds to the already high economic and social impact of LBP, and at a patient level, it significantly affects one's socioeconomic status and quality of life [7, 8]. As such, it is of great importance to prevent or treat LBP as soon as possible.

Surgery is generally the last treatment option given to patients suffering from LBP. The European guidelines for managing chronic nonspecific LBP recommend surgical intervention only after two years of conservative treatments providing no results [9]. The rationale is that surgery might mitigate the degeneration of spinal segments that lead to mechanical pain. As such, surgery can be recommended for patients that show intervertebral disk herniation or degeneration, with spinal fusion being one common procedure [9-12]. Spinal fusion consists of the fusion of adjacent

vertebrae by placing an implant within the intervertebral space, generally a bone graft placed inside a fusion cage [13]. While this procedure has lower rates of postoperative complications than other similar spinal surgeries, they are still high enough for surgery to not be recommended at the early stages of LBP [9, 13]. Nevertheless, research on improved fusion cages continues to this day, aiming to improve success rates and minimise postoperative complications. One possible strategy is the coating of fusion cages with osteoinductive materials, resulting in a cage with improved osteointegration and, consequently, improved fusion rates [10, 11, 14]. The focus of this thesis will be the development of a new osteoinductive coating, aiming to improve the general outcome of spine fusion procedures by improving the osteointegration of fusion cages.

II. Literature Review

2.1. Spine

In the broadest sense, the spine or vertebral column can be seen as an anatomic structure composed of several different bones and soft tissue structures which provide stability to the upper body, protection to the spinal cord and spinal nerve roots, and movement to the trunk [15]. A fully developed spine, as seen in Figure 1, is composed of 24 vertebra and can be divided into three groups: the cervical spine (vertebra C1 to C7), the thoracic spine (vertebra T1 to T12) and the lumbar spine (vertebra L1 to L5), each separated by an intervertebral disk. The vertebra L5 rests on top of a group of 5 fused segments that compose the sacrum, to which the coccis suspends from. Structurally, a healthy spine also shows two kyphosis (curvatures that convex posteriorly) and two lordosis (curvatures that concave posteriorly). These curvatures, alongside the intervertebral disks, help with absorbing and dissipating any load from the spine, including loads derived from walking, running, exercises or carrying objects with the upper limbs [15].

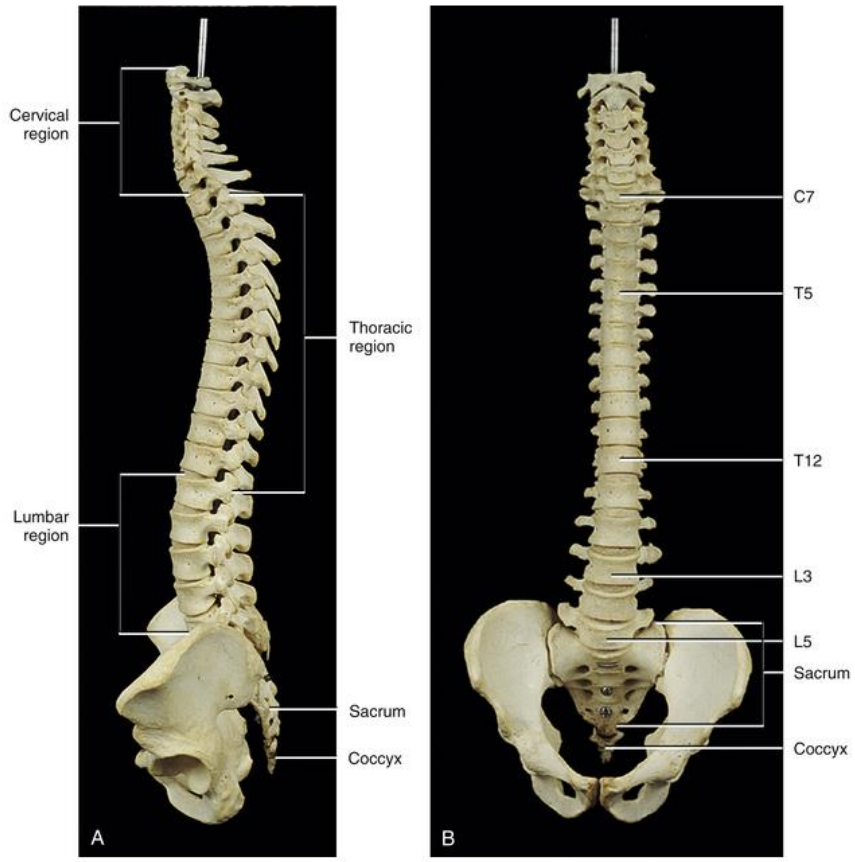

Figure 1 – Structure of the spine. Adapted from [15].

2.2. Lower Back Pain

Described as pain located in the lumbar and sacral spine regions, lower back pain (LBP) is a common symptom associated with a myriad of pathologies. These include disk degeneration or displacement, fractures, tumours, infections, or inflammations, among others. However, for most cases a source for LBP cannot be identified and are, consequently, classified as non-specific [16-18].

LBP can further be divided into acute (lasting less than 6 weeks), sub-acute (between 6 to 12 weeks) and chronic (lasting more than 12 weeks), and while most

cases of LBP are classified as acute, up to 40% of patients can develop symptoms that last longer than 6 weeks [16]. In 2019, it was estimated that 568 million people were affected by LBP globally, which correspond to around 7.3% of the entire world population [1, 5]. While general increasing with age, prevalence of LBP is high even during adolescence, being estimate to be between 18% [7] to as high as 40% [18] in this age group. A study of 402,406 adolescents in 28 countries found that around 37.0% of the participants suffered from LBP, being more prevalent in girls (38.9%, against 35.0% in boys). Moreover, adolescents who have suffered from LBP were found be twice as likely to suffer from it in their adult lives [7].

2.2.1. Social-economic impact of lower back pain

With prevalence being as high as it is, even at early ages, it is no surprise that LBP also has a big socio-economic impact in global populations. As of 2019, LBP was the leading cause of years lived with disability (YLD), contributing to 64.0 million YLD worldwide (approximately 20.6% of all YLD) [1]. Even when those metrics are adjusted to include the effect of premature death (disability-adjusted life years or DALY), LBP still ranked as the 9th highest cause of DALY (approximately 2.5% of all DALY) [6]. When divided by age groups, LBP is still a major cause of disability in all but the early childhood group. In particular, for the age group between 25 to 49 years old, it ranks as the 4th highest cause of DALY, ranking behind road injuries, HIV/AIDS and ischaemic heart diseases [5, 6].

To no surprise, LBP also has an enormous economic burden associated with, being estimated to be around GBP 2.8 billion in the UK and USD 100 billion in the USA, on direct costs alone, including healthcare visits and treatments [17]. Furthermore, there are also significant indirect costs linked to LBP, associated to the loss of industry and household productivity, with estimates for the USA being as high as USD 28.2 billion as early as 1996 [17]. The economic burden of LBP can also be

felt at an individual level, with patients suffering from the condition not only having to accommodate for personal treatment costs, but also being more subject to forced early retirement. These factors have a significant negative economic outcome for those individuals and impede them from accumulating wealth – estimated to be 87% lower compared to those who remain in full-time employment [17, 18].

2.2.2. Available treatments

Considering the high socio-economic impact LBP has at all populational levels, it is important for patients to receive effective treatment as soon as possible. Regardless of the condition being acute, semi-acute or chronic, treatment for LBP traditionally takes form as conservative or pharmacological approaches, even if specific courses of action are more indicated than others for specific cases [7, 9, 16, 17].

When taking a pharmacological treatment approach, medication should be prescribed having the duration, severity, and patient medical history in mind. It is always recommended to start with the weakest medication and progress to stronger agents if necessary. For both acute and chronic patients, it is recommended to prescribe either non-steroid anti-inflammatory drugs (NSAIDs) such as ibuprofen, or muscle relaxants for short-term pain relief. For chronic patients, it is not recommended to keep treatment for more than three months, and weak, slow-absorbing opioids can be considered in these instances. Paracetamol is not shown to have an effect on LBP higher than a placebo, and opioids are not recommended for acute cases [7, 9].

Despite pain-relief medication being an adequate approach for short-term control of LBP, conservative treatment approaches are more indicated for long-term treatments. In particular, regular exercise is shown to be effective in reducing symptoms in both acute and chronic patients, regardless of the type of exercise

being performed and of the patient's own physical capabilities. Spinal mobilisation and manipulation can also be recommended as short-term conservative strategies for pain relief [7, 9].

Finally, a surgical approach can also be considered for the treatment of LBP, with some caveats. Surgery is considered only for the worst cases as a last resort, with European guidelines suggesting it only after two years of conservative and pharmacological treatments not providing a lasting effect on the patient [9]. This is due to high costs, painful recovery, and high revision rates the recommended surgical approach presents. The most recommended procedure for surgical treatment of LBP is spinal surgery, which consists of the restoration of intervertebral space and immobilisation of the spine by promoting the fusion of two or more adjacent vertebra [9-12]. The next subsection details this procedure in more detail.

2.3. Spinal Fusion

Spinal fusion is a surgical procedure that involves the bone fusion of two adjacent vertebra by insertion of a bone graft in the intervertebral space after discectomy [13]. It is used for the treatment of degenerative disk disorder, scoliosis, trauma and tumour reconstruction of the spine, and in selected cases, can be used for the relief of chronic back pain [9-11]. Different methods for this procedure exist, differing from how the graft insertion is approached. These different approaches are represented in Figure 2 and detailed in Table 1.

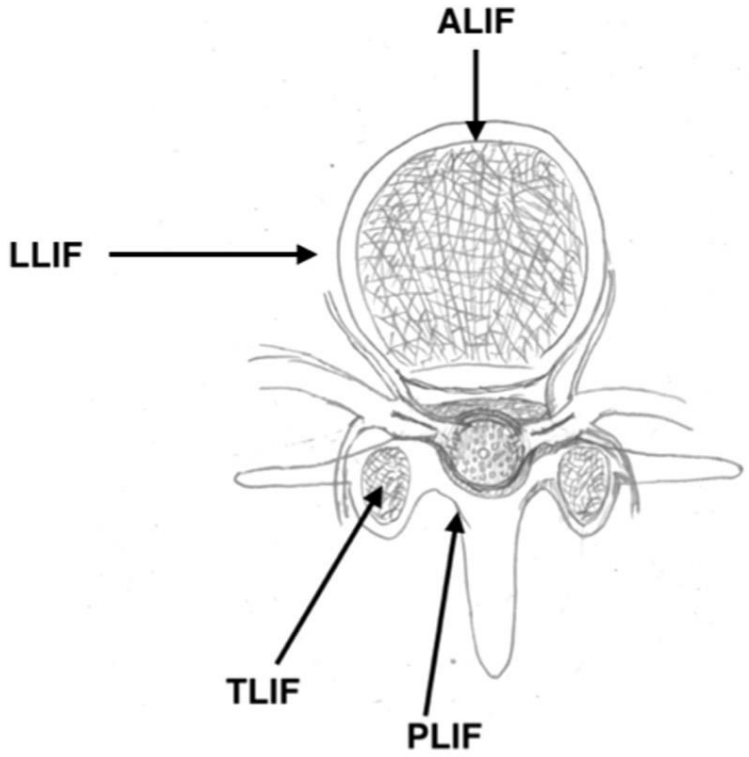

Figure 2 – Different approaches for the spinal fusion procedure. ALIF – Anterior Lumbar Interbody Fusion; LLIF – Lateral Lumbar Interbody Fusion; TLIF – Transforaminal Lumbar Interbody Fusion; PLIF – Posterior Lumbar Interbody Fusion. Adapted from [13].

Initially, this procedure involved the insertion of autologous bone grafting alone at the implant site without any sort of instrumentation. However, this method often leads to prolonged postoperative recovery and complications, while also having low success rates [10, 13]. Even after non-specific spinal instrumentation, such as rods and pedicle screws, was introduced, complications like kyphosis and pseudarthrosis were common, as well as instrumentation failure. It was only after the introduction of fusion cages, which improved the success rate of spinal fusion surgeries, while also reducing the number and severity of postoperative complications, that this sort of procedures became more common for treatment of LBP [10, 11].

Table 1 – Comparison between different spinal fusion approaches. Adapted from [13]

Technique	Entry Point	Advantages	Drawbacks
ALIF	Left paramedian incision	• Direct access to ventral surface of vertebra and disc space; • Preservation of paraspinal muscles and posterior elements of spine; • Shorter, less painful post-op.	• Retraction of iliac vessels – risk of thrombosis; • Retrograde ejaculation in 45% of male patients; • Risk of incisional hernia; • Risk of visceral complications (bowel perforation); • Lower fusion rates.
LLIF	Lateral incision	• Minimally invasive; • Good anterior column support; • No manipulation of major blood vessels; • Lower risk of neurologic injury • Preservation of paraspinal muscles; • No compromise of sexual functions; • Shorter, less painful post-op.	• L4/5 dependent of patient's anatomy; • Risks are approach based; • Risk of injury of the lumbar plexus; • Higher risk of sensory and motor deficits after surgery; • High risk or arthrodesis; • Lower fusion rates.
PLIF	Midline incision	• Avoids vascular injury; • Allows bilateral decompression and interbody fusion with one incision; • Greater surgical exposure; • Restores anatomical alignment; • Low complication rates; • Good fusion rates and clinical outcome;	• Demanding procedure; • Large open incision; • Risk of neurologic complications; • High neurologic deficit after surgery; • High risk of adjacent segment degeneration, graft migration, collapse of intervertebral space; • Revision surgery technically challenging.
TLIF	Midline or paramedian incision	• Avoids vascular injury; • Lower risk of neurologic damage compared to PLIF; • Preserves midline structural supports; • Preferable for revision surgery if ALIF is problematic;	• Significant muscle retraction; • Post-op pain; • Delayed rehabilitation; • Long-tern impaired spinal motion;

2.4. Fusion Cages

2.4.1. History and Design Evolution

Fusion cages were first introduced in 1988 for the treatment of spondylotic cervical myelopathy in horses by Bagby as hollow porous cylinders made in stainless steel [19]. These initial cages were consequently adapted for humans by Kuslich in a design that became known as the Bagby and Kuslich cages (BAK cages) [20]. The first clinical trials occurred in 1992, and by 1996 the FDA approved the first fusion cages to be used as treatment for certain spinal disorders [10, 11].

These initial BAK designs consisted of cylindrical screw cages composed of Ti alloy with thick, perforated walls, and were filled with autologous bone or cancellous bone chips as grafts for bone fusion [10, 11]. Initial results showed better fusion rates when compared to the previous practice of just using a bone graft at the fusion site. However, BAK cages had several drawbacks including low stability to extension and flexion, and a higher rate of subsidence compared to non-threaded cages [10, 11]. As such, research for improved cages continued, with several researchers proposing new designs and materials for the cages [11]. Table 2 summarises the most relevant developments during this initial period.

Table 2 – Design evolution of spinal fusion cages. Adapted from [11]

Designation	Year	Design	Additional Info	Ref
Bagby Cage	1988	Porous cylinder in stainless steel	• Designed for horse treatment	[19]
Bagby And Kuslich (Bak) Cage	1992	Porous cylinder in Ti-6Al-4V alloy	• First designed for human patients • Approved by FDA in 1996	[20]
Cylindrical Mesh Cage	1996	Ti mesh rolled into cylindrical shape reinforced with rings at each end	• Introduced by Harms and Biederman	[21]
Cylindrical Ray Cage	1997	Porous cylinder in Ti-6Al-4V alloy	• Modification of BAK cage with deeper threads • Self-tapping	[22]
Lumbar-Tapered Cage	2000	Trapezoid cages in Ti-6Al-4V or PEEK	• Basis for current designs • Improved performance and stability	[22]
Integral Fixation Cages	2005	Box-shaped cage with integral fixation screw construct in PEEK	• Does not require further instrumentation • Larger size – not suitable for every situation	[23]

Current cages typically appear as non-threaded trapezoid-shaped boxes composed of Ti alloy or polyether ether ketone (PEEK), although other designs are also available. Compared to the initial cylindrical designs, these box-shaped cages perform better in flexion, axial rotation and bending, while also improving lordosis [10, 11, 14]. In fact, the use of box-shaped cages resulted on a higher number of spinal fusion procedures, namely Anterior Lumbar Interbody Fusion (ALIF), to be used for the treatment of chronic back pain [11]. Some examples of modern fusion cage designs can be observed in Figure 3.

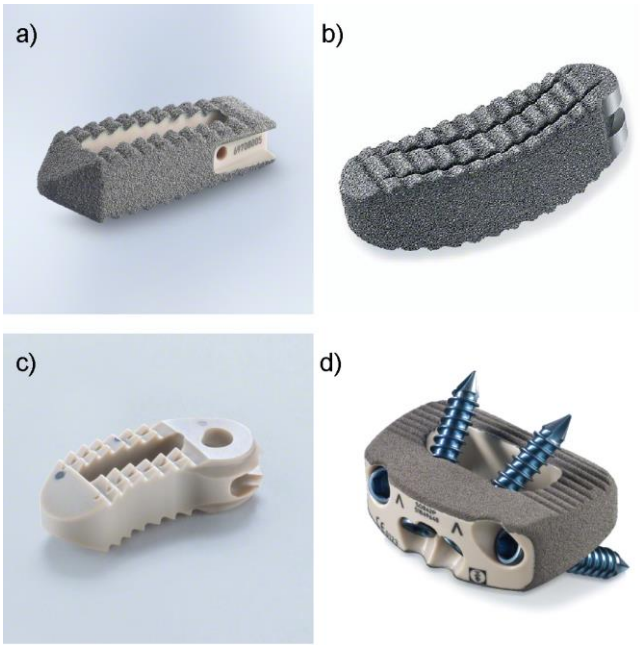

Figure 3 – Example of commercially available fusion cages: a) Ti-coated PEEK cage; b) Ti-6Al-4V cage; c) PEEK cage; d) Ti-coated PEEK cage with integrated fixation system [24].

It also important to mention that fusion cages with integrated fixation systems are also available (Figure 3.d). While these cages have the potential to reduce complications associated with the additional instrumentation used for cage fixation, they are generally larger and as such not suitable to every patient and/or implant site [11, 23].

2.4.2. Composition of Current Fusion Cages

As previously mentioned, current fusion cages are produced using one of two materials: Titanium alloy (more specifically Ti-6Al-4V) or PEEK [10, 11, 14]. As such, it is interesting to study these materials, how they compare with each other, and what drawbacks they might have.

As a material for orthopaedic applications, Ti and its alloys were first introduced in the 1940's, although they only started to be widely explored two decades later, when Branemark *et al* first reported the osteointegration phenomenon Ti implants possess in 1964 [25]. Ti-based implants are shown to become deeply integrated into bone, improving the long-term success of this sort of implants [26]. For most orthopaedic implants, including fusion cages, Ti-6Al-4V is the most commonly used Ti alloy – the presence of aluminium and vanadium in the alloy stabilise its alpha-beta structure, improving the alloy's mechanical properties when compared to commercial pure Grade 4 Ti (Table 3) [26].

Table 3 – Comparison between CP Ti grade 4 and Ti-6Al-4V. Adapted from [26]

Material	Main Alloying Elements (Weight %)	Elastic Modulus (GPa)	Yield Strength (MPa)	Ultimate Strength (MPa)
Ti grade 4	Balance Ti Max 0.5 O	105	692	785
Ti-6Al-4V	Balance Ti 5.5 – 6.5 Al 3.5 – 6.5 V	110	850 – 900	960 - 970

Ti-6Al-4V presents several beneficial properties for spinal fusion cages: it is biocompatible, it has a low density (approximately 4700 $kg.m^{-3}$), a moderate elastic modulus compared to other metallic materials (110 GPa) and is resistant to corrosion due to the spontaneous formation of a TiO_2 layer at its surface. It is also fairly easy to modify the surface of Ti and any of its alloys (including Ti-6Al-4V), which further improves the implant's osteointegration [10, 11, 26]. However, wear and shear resistance are poor for Ti-based implants, and while lower than most metals, the elastic modulus of Ti-6Al-4V is still an order of magnitude higher than that of cortical bone (110 GPa, compared to 10-30 GPa of cortical bone). This difference in stiffness

can lead to stress shielding, which together with the normal local inflammation can cause bone atrophy, subsidence, and implant failure [11, 14, 26].

Introduced in the 1990's by AcroMed as an alternative trying to address the drawbacks of Ti alloy cages [11], PEEK is a semi-crystalline linear polycyclic aromatic thermoplastic first developed in 1978 [27]. The chemical structure of PEEK can be observed in Figure 4. As is possible to observe, PEEK has an aromatic molecular backbone, with combinations of ketone and ether functional groups between the aryl rings. This chemical structure provides PEEK with its physical and chemical stability. The some of the physical properties of PEEK given in Table 4.

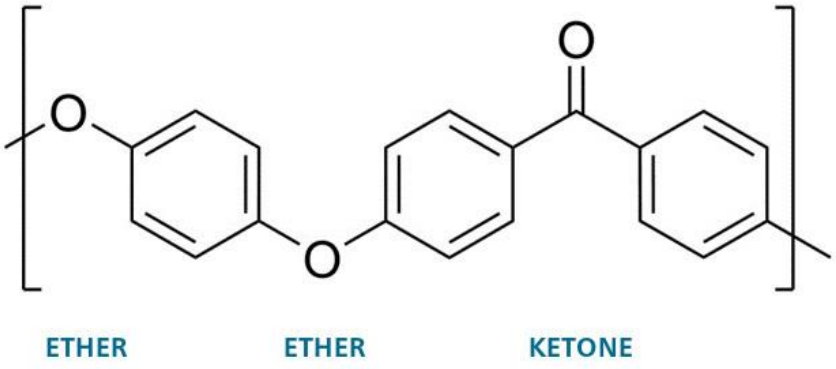

Figure 4 – Chemical structure of Polyether ether ketone [28].

The main advantage of PEEK compared to Ti-6Al-4V for fusion cages is its elastic modulus, which is much closer to bone's (3.6 GPa, with carbon fibre-reinforced PEEK able to reduce the difference ever further) and as such able to prevent subsidence and improve fusion rate [10-12, 14]. PEEK cages are also radiotranslucent and MRI-compatible, meaning that it is possible to evaluate graft integration using imaging techniques [10, 11, 14, 27]. Moreover, PEEK is also wear

resistant, and due to its chemical stability is able to remain unaltered after sterilisation and able to sustain attacks by most substances except concentrated sulphuric acid. It is also shown to be biocompatible with no toxic or mutagenic effects reported [10, 11, 27].

Table 4 – Some of PEEK mechanical properties [29, 30]

Material	Elastic Modulus (GPa)	Yield Strength (MPa)	Ultimate Tensile Strength (MPa)
PEEK	3.6	80 – 160	80 – 160

However, its chemical stability also results in PEEK's major drawback: it is generally a bioinert material, which prevents beneficial biological responses, like osteoinduction and integration. Nevertheless, this problem can be circumvented with appropriate surface modifications and development of PEEK-based composite materials [10, 11, 27].

It is debatable which kind of cage has better performance, although evidence slightly favours PEEK cages. An analysis of different, independent studies has shown that there was no statistical difference between fusion rates in patients using Ti-alloy or PEEK cages, though evidence suggest that Ti-alloy cages might result in better fusion rates in the lumbar spine, while PEEK might perform better in the cervical spine [31]. Moreover, different reports have shown different results when comparing initial restoration of disc height [10], with one showing no difference between Ti-alloy and PEEK in this regard [32], while a different one reporting better clinical outcome when using PEEK cages [33]. However, Ti-alloy cages have been shown to have higher subsidence when compared to PEEK cages in all reports [10, 31]. That is not to say that are no problems associated with PEEK cages either [12],

as one report claimed that operation times with PEEK cages might be longer [34], while another has shown PEEK cages might have higher rates of dislocation [35].

2.4.3. Future Trends

Research on spinal fusion cages has been mostly focusing on improving the osteointegration of PEEK cages or in the research and development of new materials for cage production.

A relatively simple solution for improving PEEK's bioactivity may come from surface modification techniques, with the use of bioactive coatings a very interesting solution. In fact, PEEK cages with porous Ti coatings are already commercially available (figures 2.a and 2.d) with proven enhanced osteointegration when compared to uncoated PEEK cages [36]. More recently, hydroxyapatite coatings have also been shown as potential alternatives for improving the osteointegration of PEEK [11, 14, 37, 38], although the currently available methods for producing HAP coatings need to be revised [39-41]. A different strategy is the development of PEEK-based composites, with solutions based on both Ti and HA having been explored with promising results [11, 14].

Finally, new materials are also being explored for spinal cage production, with silicon nitride and porous tantalum being perhaps the most interesting solutions, although nitinol also shows potential [11, 14]. Silicon nitride implants, which have the added bonus of not requiring a bone graft, are already commercially available (Figure 5), with at least one study reporting similar clinical results to PEEK cages [42].

Figure 5 – Silicon nitride fusion cage. Adapted from [42].

2.5. Osteoinductive Coatings

2.5.1. What is a coating?

In a general way, a coating can be described as a surface modification technique by deposition of a material onto the surface of a different one. The idea is to functionalise the surface of a material without losing its bulk properties. For orthopaedic implants, the main function of a coating is to improve osteointegration, though they can also be used to improve wear resistance and even some antibacterial properties [43].

2.5.2. Hydroxyapatite

Part of the apatite family, hydroxyapatite (HAP) is a crystalline form of calcium phosphate with hexagonal lattice, a formula of $Ca_{10}(PO_4)_6(OH)_2$ and a Ca/P molar ratio of 1.67. What makes HAP very interesting as a biomaterial is its presence as

the main mineral component in bone and teeth, which helps explaining HAP's excellent biocompatibility, osteoconductive behaviour, ability to directly bond with bone and its lack in promoting an inflammatory response [44-46].

Due to its crystalline nature, HAP is a very stable biomaterial with a very slow resorption rate, with some reports claiming it can be maintained *in vivo* at least for up to 3 years, allowing for slow bone ingrowth and cell colonisation [44]. However, bulk HAP is not a reliable biomaterial, especially in wet conditions, mainly due to its poor mechanical performance, and as such, its use is generally limited to small bone defects with low loading conditions [44, 45]. Still, HA can be used as bone fillers, bone scaffolds, soft tissue repairs, delivery systems, and, more interestingly for this project, as bioactive coating for orthopaedic implants [44, 45].

It is important to notice, however, that bone HA is not pure, stoichiometric HAP, but is instead a non-stoichiometric HAP with structural imperfections due to ion substitution [46-48]. In general, these substitutions occur in the following manner [46, 47]:

- Cations usually substitute Ca^{2+} ions
- Anions usually substitute (OH) groups
- SiO_4 can partially replace PO_4
- CO_3^{2-} can substitute OH or PO_4 to form, respectively, A or B-type carbonate HAP

The presence of these substitutions has a great effect on HAP, not only on its degradation rate, but also by improving its bioactive behaviour [46]. As such, researchers have been studying the effects these substitutions might have as to include them in new HA formulations. Table 5 summarises some of the trace elements present in biologic HA that have been discovered, and their bioactive effect.

Table 5 – Possible Hydroxyapatite substitutions [46-48]

Substitution	Effect
Na	• Affects cell adhesion; • Significant role in bone metabolism and osteoporosis.
Mg	• Important role in early stages of osteogenisys; • Stimulates osteoblast proliferation; • Indirectly influences mineral metabolism.
Zn	• Important mineral for the normal growth and development of skeletal system; • Promotes osteoblast activity and inhibits osteoclasts; • Important role in several biological funtions.
Sr	• Stimulates osteoblast differentiation; • Inhibits osteoclast activity and bone resorption; • Stimulates the expression of angiogenic factors.
K	• Influences biomineralisation process and cell adhesion; • Important rule in apatite mineral nucleation process; • Active element in biochemical processes.
F	• Enhances crystallisation of calcium phosphates in bone formation; • Enhanced corrosion resistance.
Cl	• Enable acidic environment that activates osteoclasts
Si	• Promotes synthesis of collagen type I, osteoblast differentiation and bone repair. • Induces higher dissolution rate.
CO_3^{2-}	• Improves biocompatibility and resorbability of HAP

As shown in Table 5, there is a variety of possible HAP substitutions, but two that might be of great interest are Mg and Sr substitutions. In fact, Mg-substituted HAP is already available in the market [49], with Mg playing an important role in early stages of bone development, stimulating the proliferation of osteoblasts, and indirectly influencing mineral metabolism [46, 48]. On the other hand, Sr is shown to both stimulate osteoblast differentiation and inhibit osteoclast activity and bone resorption. It also stimulates the release of angiogenic factors, which play an important role in the vascularisation of tissues [46, 47, 50]. With the roles that both Mg and Sr seem to play in the formation of new bone, it seems of great interest to study the development of HAP formulations containing substitutions with both elements.

As a coating material, HAP is mainly used due to its osteoconductive and bone-bonding abilities, while also shielding metallic implants against corrosion [39, 51]. In general, HA have been used on a wide range of implants, and have a high success rate, with a failure rate of less than 2% [39, 51]. While several techniques are able to produce HA-based coatings, only plasma spraying is widely available and is commercially approved by the FDA, mostly for being regarded as the most cost-effective technique [39, 40]. This technique consists in the use of a high temperature plasma flame (30.000 K at core) that is used to rapidly melt and accelerate the coating material onto a substrate [40, 41]. Plasma spraying does show some considerable drawbacks, however, including poor thickness uniformity, poor adherence to substrate, phase impurity, low crystallinity, and poor mechanical performance (tensile strength, wear resistance, hardness, toughness and fatigue), while also not being adequate for complex geometries [39-41]. As such, it is important to find alternative coating techniques which allow HAP to maintain its properties intact.

2.5.3. Titanium Dioxide

Being the most common oxide of titanium, titanium dioxide (TiO_2) is white metal oxide first discovered in 1791, and widely used in a variety of applications, including as a pigment, as a photocatalyst and photovoltaic agent and as a coating material, among others [52, 53]. TiO_2 is most commonly found in nature in the form of rutile, anatase or brookite, but it is known to exist in at least 11 different crystal forms, as well as in an amorphous state [52, 53]. Figure 6 exemplifies the known crystal forms of TiO_2.

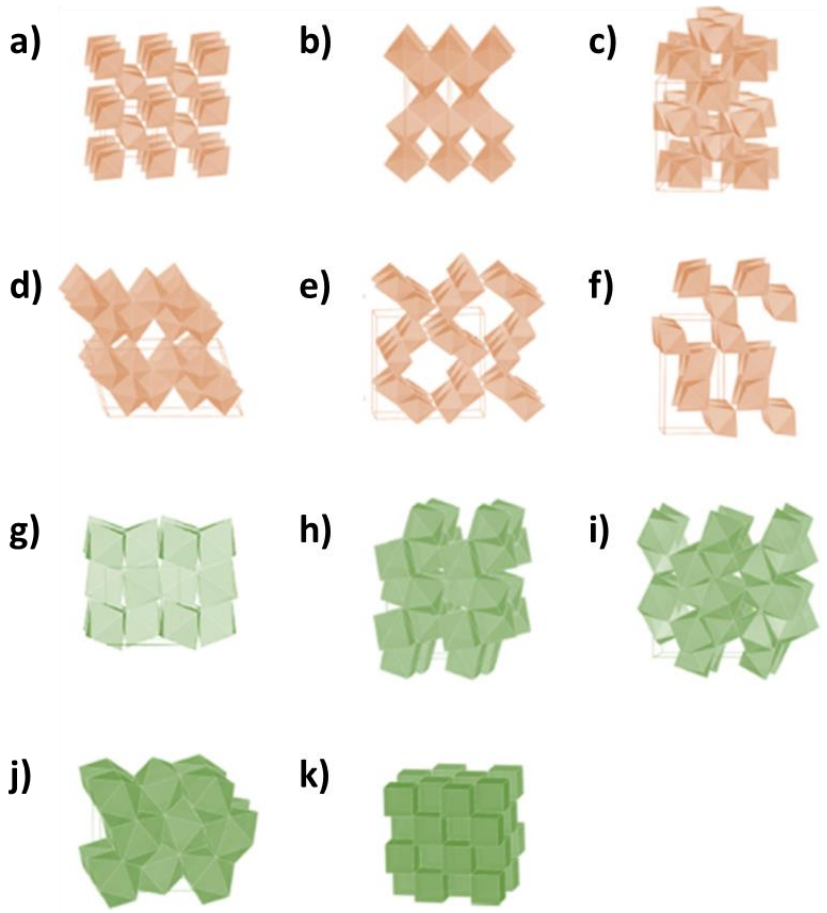

Figure 6 – Structure of the known crystal phases of TiO_2: a) rutile; b) anatase; c) brookite; d) TiO_2(B); e) hollandite-like TiO_2(H); f) ramsdellite-like TiO_2(R); g) columbite-like TiO_2(II); h) baddeleyite-like; i) TiO_2(OI); j) cotunnite-like TiO_2(OII); k) fluorite-like cubic phases. Unit cells are outlined by using thin lines [52].

One interesting aspect of TiO_2 is that it naturally occurs in Ti-based implants and is directly responsible for their biological performance [26, 54, 55]. This natural occurring TiO_2 layer is, however, extremely thin (thickness between 2-6 nm) and amorphous in nature, which limits the beneficial biological effects linked to TiO_2 [56]. Nevertheless, by increasing the thickness and/or crystallinity of this TiO_2 layer, its biological performance can be further improved [57-60].

2.5.4. Sol-Gel Chemistry

In a general manner, sol-gel chemistry can be described as a method for preparing inorganic solids through transformation of liquid organic precursors to a sol, which will then be transformed into a gel [61, 62]. To better understand this process, a sol is defined as a colloidal suspension of solid particles in a liquid phase, while a gel is defined as a non-fluid 3D network that extends through a fluid phase [61, 62]. As such, sol-gel chemistry revolves around the polycondensation of the solid particles present in the sol as to produce a 3D matrix that will form the gel.

While the chemistry involved in the sol-gel process is deeply complex [62], it can be described in the following steps [61, 62]:

- Synthesis of the “sol” from hydrolysis and partial condensation of alkoxides.
- Formation of the gel via polycondensation.
- Syneresis (aging) where condensation continues within the gel network, shrinking it and resulting in expulsion of solvent.
- Drying of gel to form either a dense xerogel (shrunk, collapsed gel) or an aerogel (gel where the liquid phase was replaced by air).
- Calcination at high temperatures (if required).

The use of sol-gel chemistry as a coating technique is illustrated in Figure 7. The process involves the preparation of the gel through the polycondensation of the precursor sols, dipping the substrate into the gel, and then let gel dry (and, if necessary, sinter) on the substrate’s surface [63]. While not strictly necessary, sintering can be an important step in the optimising the coating: in one hand, sintering at lower temperatures and/or shorter time periods result in more porous structures, which are can positively impact cell migration and the osteointegration of the implant [64, 65]; on the other hand, the coating will be more stable and adhere better to the substrate if sintered at higher temperatures for longer periods of time [41].

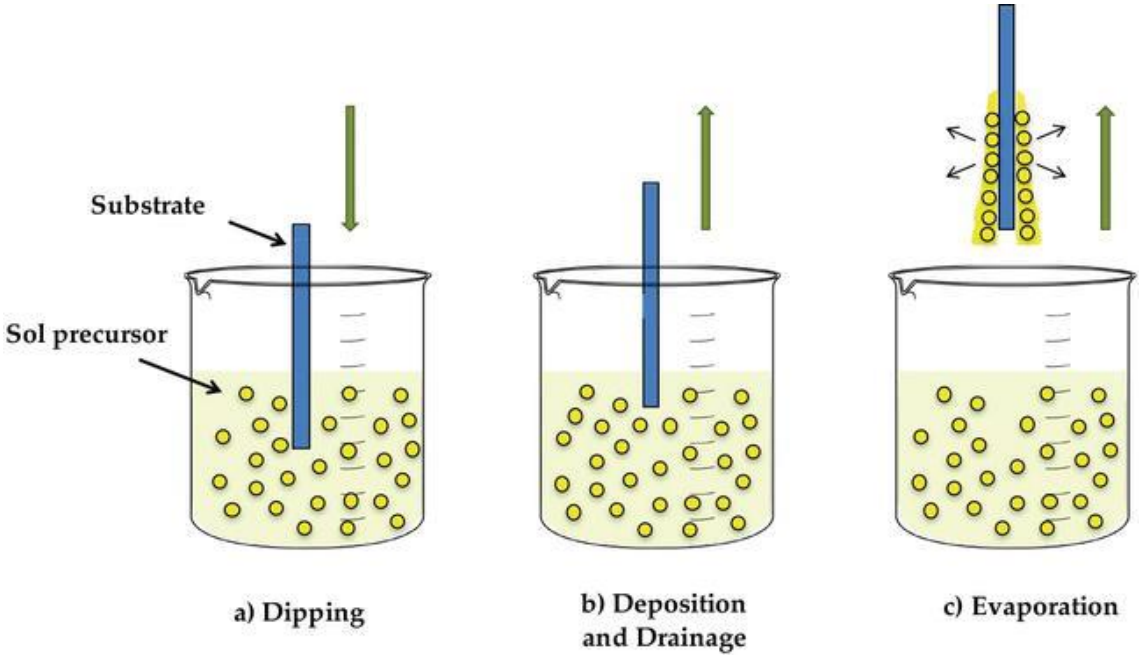

Figure 7 – Illustration of the coating process by sol-gel chemistry [63].

Sol-gel can be very interesting to explore, as it shows several advantages, mainly its simplicity and cost-efficiency for the production of thin, high quality coatings at low temperatures (including sintering) [40]. Other advantages include the excellent adhesion sol-gel coatings generally present, the easiness to coat materials with complex geometries, and its ability to produce high-purity coatings with highly controlled composition [40]. As coatings for biomedical implants, it is important to refer as well the increased bioactivity sol-gel coatings show when compared to coatings with similar compositions but prepared with different methods, due to the presence of hydroxyl groups on the surface of sol-gel coatings [66, 67].

Due to the aforementioned advantages, sol-gel coatings have been widely studied for different biomedical applications, as means to improve integration of the implant, to introduce novel antibacterial properties, and/or to protect the implant from corrosion. Tranquillo and Bollino published a review in 2020 that highlights some of the advancements in this area, which include coatings of HAP and other calcium

phosphates, TiO_2, silica, zirconia, and different composite materials [68]. In particular, sol-gel has also been used to create TiO_2/HAP coatings for orthopaedic implants [66, 69-71]. Of note, no reports on the development of sol-gel coatings that crystallise TiO_2 directly in the surface of polymeric substrates such as PEEK for biomedical applications have been found. However, other fields of engineering have proven that, with the right synthesis conditions, it is possible to directly coat polymeric substrates with crystallised TiO_2 using sol-gel [72-75].

As a final note on sol-gel coatings, several parameters can influence the sol-gel formation and, by extension, coatings produced using this method. These are classified in “respected” and “neglected” parameters and can be found on Table 6. In this case “respected” means the parameters are highly important for the sol-gel process, while “neglected” parameters are ones that, while having an effect on the process, do not require as much attention as the “respected” ones [40].

Table 6 – Parameters that affect the Sol-Gel process [40]

Respected Parameters	• Choice of precursors • Concentration of precursors • Water/alkoxide mol ratio • Type and amount of catalyst • Control of hydrolysis reaction
Neglected Parameters	• Volatile evolution rate in sol • Variation in ambient conditions • Small impurities in sol • Rate of change in viscosity

2.6. In vitro testing of osteoinductive materials

In a general sense, an osteoinductive material can be defined as one which [76]:

1. Recruits mesenchymal stem cells (MSCs) to its surface.
2. Differentiate MSCs into osteoblasts.
3. Induces the formation of ectopic bone when implanted into extra-skeletal locations.

For a material to be considered osteoinductive, it should be able to induce MSC differentiation *in vitro* without the need of osteogenic media [76]. Due to their importance in defining the osteoinductive nature of an implant, MSCs appear as the most relevant cell type for this material.

2.6.1. Mesenchymal Stem Cells

First identified by Friedenstein *et al.* as fibroblast precursors within the bone marrow [77], mesenchymal stem cells (mesenchymal stromal cells or MSCs) are a population of adult stem cells known for their ability to differentiate into different cell types such as osteoblasts, adipocytes and chondrocyte, as shown in Figure 8 [78]. Due to the great variability MSC populations show due to differences in species, tissue source and different *in vitro* culture conditions, the International Society for Cellular Therapy decided to standardise the definition of MSCs as such [76, 78]:

- Heterogeneous population of plastic-adherent cells under standard culture conditions.
- Ability to form colonies when grown at clonal densities (colony-forming units – fibroblasts, or CFU-F).
- Positive expression of the cell surface antigens CD105, CD73 and CD90.
- Negative expression of the cell surface antigens CD34, CD45, CD11b, CD19 and HLA-DR.

- Under standard differentiation conditions (medium supplemented with 10% of Foetal Bovine Serum), able to differentiate into osteocytes, adipocytes and chondrocytes *in vitro* (Figure 8).

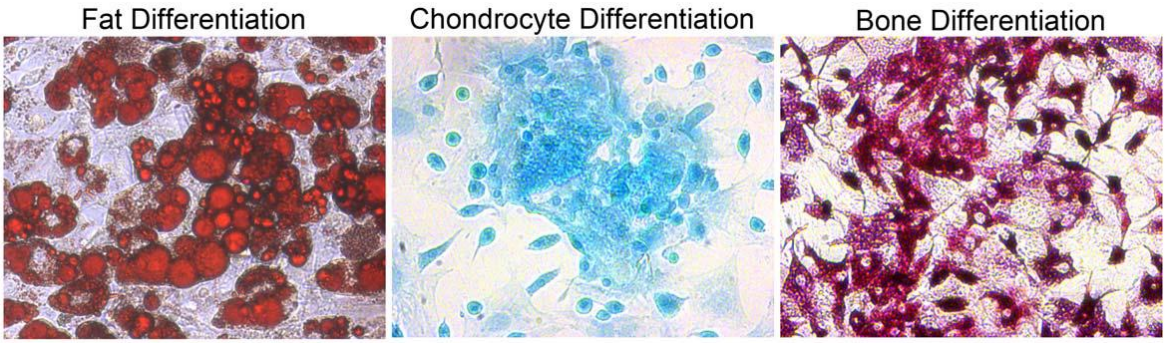

Figure 8 – Tri-lineage differentiation of mesenchymal stem cells [79].

MSCs can be isolated from a variety of different sources, including bone marrow, umbilical cord blood and stroma, placenta, adipose tissue, among others, and *in vitro* expansion starts with an initial lag phase followed by a rapid expansion phase [78].

The classification of MSCs as a stem cell population has been put into question. Unlike other adult stem cell populations, most MSCs display a limited expansion potential *in vitro* (from 5 to 10 passages) and their differentiation potential decreases with increased culture [78]. However, it is not known if this is a true indicator of the “stemness” of this population, or due to sub-optimal isolation techniques and/or cell culture conditions [78].

2.6.2. Primary Cells vs Cell Lines

For any kind of cell culture, cells might have different origins. In a general manner, it is possible to identify cells as coming from two sources: primary sources, which originate primary cells, or cell lines. Finding which one is best suited for any project is of great importance, as the same cell type from different sources might have different properties and as such might be relevant only for specific studies.

Primary cells are cells that are isolated directly from biological tissues [80, 81]. As such, primary cell cultures more closely resemble actual biological tissues and are more representative of an actual *in vivo* environment [81]. As discussed previously, the sources for primary MSCs include bone marrow, umbilical cord blood and stroma, placenta, adipose tissue, among others, with bone marrow being the most common source [78, 82]. However, as representative as they can be, the use of primary cells has several drawbacks. The first major drawback is the inherent variability that primary cells from different donors (or even from different sources from the same donor [76, 78]) exhibit, which may derive from the donors age, gender, lifestyle, genetic factors, among others [81, 83]. This variability might be important for *in vivo* tests of implantable devices or tissue engineering solutions, as to determine the possible clinical relevance of these solutions in different patients. However, it can be a problem while studying different phenomena with consistent results, especially in long-term projects. At the same time, most primary cells rapidly lose or alter their characteristics with extended or repeated culture [81, 83, 84]. As previously discussed for MSCs, this includes their lifespan as well as their differentiation potential [78, 83].

After a primary cell culture has been passaged (or subcultured) at least once, it becomes a cell line. As previously discussed, most of these cell lines tend to lose or alter their characteristics with increasing passages, while also having a limited number of passages [81, 83, 84]. These are named *finite cell lines,* and if specific cells from a cell line are selected to have specific properties, they become a *cell*

strain [81, 84]. If a cell line is able to bypass the control mechanisms that regulate how many times can a cell be passaged (like cell lines derived from cancer cells, or cells that have been immortalised *in vitro*) they become known as a *continuous* or *immortal cell line* (or *continuous cell strain* if cells with specific characteristics are selected) [81, 84].

Considering the specific case of immortal cell lines, these show several advantages to primary cells besides their unlimited passage potential: they are also more cost effective, easier to use, and have less ethical concerns associated [85]. As they represent a pure population of cells, they are also able to provide consistent samples and reproducible results [85]. But despite their numerous advantages, there are still some concerns about their clinical relevance. As previously stated, cell lines have different characteristic than primary cell cultures, and as such might provide different results to those from primary cells [81, 83, 84]. At the same time, the techniques used to immortalise a cell line, which further alter the genome of the cell, further accentuate the differences in cell function and activity between cell lines and primary cultures [83, 85].

In an ideal scenario, both immortal cell lines and primary cells would be used during a long-term project for testing the *in vitro* biologic performance of novel medical solutions. Immortal cell lines are useful for optimisation of culture and testing parameters, as they provide consistent and reproducible results. Moreover, primary cells should be used to validate the optimisations and results obtained with cell lines in an environment that more closely resembles *in vivo* conditions [81-83].

2.6.3. Serum-free cell culture

While some cells are able to be cultured in media without supplementation, most can only be cultured in media which has been supplemented with components such as hormones, growth factors, amino acids, among others [86].

Standard culture media is generally supplemented with animal serum, with the most common being Foetal Bovine Serum (FBS) [86, 87]. FBS is regarded as a good supplement containing all necessary components cells need to survive culture conditions, and culture media is usually supplemented with 10-20% of FBS [86, 87]. However, several drawbacks to FBS are also known, starting with its undefined nature and lot-to-lot variability, which lead to differences in cell culture growth, [86, 87]. FBS can also overstimulate the proliferation of certain cell types such as fibroblasts, which can be a problem in cultures with mixed cell populations [86, 87]. Moreover, FBS shows risk of introducing transmissible diseases such as bovine spongiform encephalopathy (BSE). In fact, it has been reported that between 20% to 50% of commercially available FBS tests positive for viral infections [86, 87]. Availability of FBS can be an issue as well, as it is strictly correlated with the activity of the beef industry [86, 87]. Moreover, on an ethical and animal-rights level, the use of FBS in cell culture can be seen as a major issue, as the collection of FBS requires the slaughter of millions of bovine foetuses annually to supply worldwide demands [86, 87].

Alternatives to FBS and animal serum exist, with one being humanised media containing either human serum (from autologous or allogenic sources), human platelet lysates, thrombin-activated platelet rich plasm or umbilical cord blood plasma [87]. While humanised media is shown to be as or more effective than FBS-containing media for human cell types, it still shows many drawbacks including lack of availability of autologous serum, less efficacy of allogenic serum, risk of disease transmission and lot-to-lot variability (even if lower than with FBS) [87, 88].

Another interesting alternative to FBS is the use of serum-free media (SFM). As the name implies, SFM are a subcategory of media that does not use any sort of serum as supplement, using instead other sources of nutrients and growth factors [87]. The term SFM is often used as a synonym to chemically defined media (CDM). However, while sharing some similarities, SFM and CDM refer to different types of media [87, 89]:

- SFM can be supplemented with purified animal or human-derived components (like albumin, transferrin, insulin, and lipids), which might still be not fully characterised and be sources of variability or contamination (even if less probable than using serum) [87, 89];
- CDM is entirely free of animal or human derived components, with all components being well defined and characterised, and a few being recombinant or synthetic proteins, hormones, cytokines and/or growth factors.

In short, while all chemically defined media are serum-free, not every serum-free media is chemically defined. Distinguishing both terms is important since many commercially available SFM proclaim to be CDM, without disclosing the full media composition, and sometimes containing animal-derived components such as bovine albumin [87, 89]. A more extensive summary of media classification can be observed in Table 7. Regardless, any SFM is less prone to lot-to-lot variability, and has lower probability of contamination with bacteria, virus or mycoplasma, with the chances lowering the more defined the media is [87, 89].

Table 7 – Classification of human-derived cell culture media. Adapted from [89]

Classification	Definition	Supplements
Serum-Containing	• Media supplemented with animal or human serum.	FBS; Human serum.
Xeno-Free	• Media containing only human-derived supplements.	Human serum; Human plasma; Human platelet lysate
Serum-Free	• Media not supplemented with neither serum nor unprocessed plasma.	Platelet lysate Serum fractions Animal/Plant Hydrolysates
Animal Component-Free	• Media containing neither animal nor human-derived components.	Plant hydrolysates Recombinant materials
Chemically Defined	• Media containing only components whose chemical composition and structures are known and all chemical species are specified; • Media containing no components of unknown composition	Recombinant materials
Protein-free	• Media containing no proteins, although it can contain hydrolysed proteins and small peptides with low molecular weight; • Might contain ill-defined components such as native lipids, and as such might not be chemically defined	Hydrolysed proteins Small peptides

In the specific case of MSC culture, it is still not possible to develop a universal SFM for MSCs of all various sources, mostly due to the already great variability that MSCs can show. In fact, MSCs from the same donor and cultured in the same media may differ considerably in proliferation kinetics depending of the extraction site (bone marrow, adipose tissue, among others) [87]. Still, several companies are already commercialising SFM specifically for the culture of MSCs. A list of some of the available SFM media for MSC culture can be observed in Table 8 [87].

Table 8 – List of SFM available for the expansion of MSCs. Adapted from [87]

Name	Cat No.	Company	Classification
StemMACS MSC Expansion Media Kit Xf, Human	130-104-182	Miltenyi Biotec	SF, XF
Mesenchymal Stem Cell Growth Medium DXF	C-28019	PromoCell	SF, XF, CD*
Therapeak MSCGM-CD (Bullet Kit)	190632	Lonza	SF, XF, CD*
MesenCult-XF (Culture Kit)	5429	Stem Cell Technologies	SF, ACF, CD*
MesenGro	ZRD-MGro-500	StemRD	SF, CD
StemPRO Msm SFM (Media Kit)	A10332-01	Life Technologies	SF
StemPRO MSC SFM-XF (Media Kit)	A10675-01	Life Technologies	SF, XF

SF – Serum-free; XF – Xeno-free; CD – Chemically Defined; ACF – Animal Component Free.
* While suppliers claim the media as “defined”, they might not be chemically defined.

Some research groups have used in-house SFM formulations for culturing MSCs, resulting in optimised media to specific in-house donor MSC’s. While the optimisation of these media can be time consuming, they result in higher cell potency and productivity when compared to other specialised media [87].

At the same time, in-house SFM formulations also require an extensive quality control of raw materials, which might suffer from lot-to-lot variability, as well as from issues with the consistency of media preparation, mixing and media hold stability [87]. In contrast, while less optimised for specific MSCs, commercially available SFM support higher cell population growth rates, and have consistent, high-quality formulations, with proven safety and regulatory compliance [87]. Commercial SFM also supports efficient isolation, multi-passage expansion, with maintaining MSC multipotency and acceptable phenotype characteristics [87]. However, market needs still demand media optimised for specific MSCs, and the previously mentioned possible misuse of the terms SFM and CDM can be an issue depending on the specific project needs [87, 89].

2.7. Design of Experiments

Planning an experimental work can be difficult, as an experiment can be affected by different factors and by how they vary. However, some of these factors might impact the outcome of an experiment more significantly than others, making their identification and study more crucial. Moreover, sometimes it is the interaction between any two or more factors that might affect the obtained results. As such, it is important to determine which factors or interaction significantly affect an experiment, and how varying said factors affects the outcome of the experiment to find the optimal response [90-92].

Traditionally, one would vary the levels of one factor at a time, while maintaining all other factors at a constant level [91, 93]. This approach has its problems, however. Specifically, this approach only allows to determine individual effects, not being able to study the interactions between the different levels of all different factors [90, 91, 93]. One could experiment with all possible combinations of factors and levels, but not only would the results obtained from this strategy be harder to analyse, the number of necessary runs could easily become prohibitively high [91]. For example, when exploring 5 factors with 5 levels each, the number of necessary runs would rise to 3125. However, with a properly planned experimental work, it is possible to study how factors and interactions affect an experiment with a minimum number of runs.

This is the goal of Design of Experiments: to use statistical principles to minimise the number of runs necessary to identify factors and interactions that significantly affect an experiment, while also creating a mathematical model able to predict the conditions that result in an optimal response [90-92]. DoE offers an organised approach able to address both simple and complex problems. If well designed, the data obtained using DoE is more useful, precise, and obtained more effectively than data acquired in a traditional fashion. Due to the smaller number of experiments or runs, and the organised nature of DoE, the acquired data also

becomes easier to analyse. Depending on the goal of the design, the resulting mathematical model can then be used to identify the conditions that result in an optimal outcome, or to identify the region where that optimal response might be, which can then be further inspected by a future, more precise design [90, 91].

2.7.1. Design strategies

Depending on the objective of the intended DoE, several different design strategies can be explored. Some strategies are more indicated for screening factors, others for optimisation of the process in study. The number of factors in study can also influence the design approach taken. The next two sections describe the strategies followed during this thesis.

2.7.1.1. Full factorial designs

Full factorial designs (FFD) are the basis of classical DoE and can be used for both screening and optimisation [90, 91]. When using a FFD strategy, for each factor it is set a minimum (– or -1) and maximum (+ or 1) value, with every run being a combination between – and + values of each factor. While not compulsory, it is also useful to set a centre value (0) for each factor, obligatorily equidistant between – and + [90]. The 0 values define the centre point of the design (the combination between all 0 values of each factor), useful to detect the presence or not of curvature in the real response. Moreover, repeat experiments of the centre point can be used to determine the variability of the experimental model [90, 94]. The number of total runs of a design can be calculated using Equation 1. As it is possible to infer, the number of runs can exponentially grow with the number of factors, and usually FFD is recommended for designs with 4 or less factors.

Equation 1 – Number of runs in a Full Factorial Design. Adapted from [90]

$$Runs = 2^n + C$$

n = number of factors
C = number of centre point runs

FFD assumes that each factor and interaction affect the response linearly, and as such can be used to optimise experiments that are shown to behave in a linear fashion. However, if a curved response is detected, this strategy cannot be used for optimisation purposes. Nevertheless, a FFD can be augmented with complementary runs that allow to estimate the curvature of a model [90]. Most commonly, the design is transformed into a Composite Central Design (CCD), which adds *2n* runs to the runs already present in FFD [90]. For each of these new runs, one factor is set to 0, while the others are set either all to + or all to –. This new design will be able to create a model capable of predicting quadratic effects and as such estimate the curvature of the response [90, 91].

2.7.1.2. Definitive screening designs

First developed by Jones and Nachtsheim in 2011 [95], and further optimised by Xiao *et al* in 2012 [96], Definitive Screening Designs (DSD) are especially useful for screening the effect of a large number of factors. In fact, to effectively use a DSD strategy, a minimum of four factors must be in study, and for an *n* number of factors, the number of necessary runs can be calculated by using Equation 2. Because the number of runs grows linearly with the number of factors, contrary to exponentially as in the case of FFD (Equation 1), DSD is a much suitable approach when studying larger numbers of factors. As an example, while a minimum of 64 runs are necessary to study 6 factors using FFD, using DSD one can study those same factors using only 13 runs [96, 97].

Equation 2 – Number of runs in a Definitive Screening Design. Adapted from [96]

$$Runs = 2(n + a) + 1$$

If n equal to 4:
    a = 2
If n equal to odd number:
    a = 1
If n equal to even number:
    a = 0

Defining the settings for each DSD run is not as straight forward as it is for FFD runs. To better understand the process, a few algebra concepts must be first explained:

- **Square matrix:** matrix with the same number of rows and columns.
- **Transpose matrix:** matrix created by turning the rows of a different matrix into columns, and *vice-versa*.
- **Identity matrix:** square matrix in which the values from its main diagonal are all equal to 1 and all remaining values equal to 0.
- **Orthogonal matrix:** matrix which, when multiplied by its transpose, results in an identity matrix.
- **Conference matrix:** square orthogonal matrix in which the values from its main diagonal are all equal to 0, while all remaining values are a combination of 1 and -1.
- **Zero matrix:** matrix in which all values are equal to zero.

The design matrix for a DSD approach is constructed as exemplified in Equation 3 [96, 97]. First, for each factor, –, + and 0 values are set, with 0 equidistant from – and +. Then, a conference matrix with the same number of columns as *n*+*a* (see Equation 2) should be created, as well as a one-row zero matrix, also with *n*+*a* columns. The design matrix can then be created as defined by Equation 3, with each row setting the conditions for each experimental run. The zero matrix defines the conditions for the centre point run.

Equation 3 – Construction of a Definitive Screening Design table

$$D = \begin{pmatrix} C \\ -C \\ 0 \end{pmatrix}$$

D = design matrix
C = conference matrix
0 = zero matrix

If well-constructed, the obtained design matrix should be an orthogonal matrix with *2(n+a) + 1* rows (see Equation 2). The reason why *a = 1* when studying an odd number of factors is to guarantee that the obtained design table is orthogonal. However, when performing the experimental runs, the last column of the design table should be ignored, as it is not setting the conditions for any factor in study. The same reasoning explains why *a = 2* when studying 4 factors, dropping the two last columns in this case [97, 98].

The design matrix being orthogonal explains the advantages of DSD compared to other screening designs. To start, it guarantees that all individual factors are completely independent from one another and from any two-factor interaction. Moreover, not only does this design matrix allow DSD to estimate quadratic effects, but said effects are also orthogonal to main effects and not completely confounded, though correlated, to two-factor interactions. Finally, with 4 to 16 factors, it is possible to estimate the full quadratic model for any combination of 3 or fewer factors. This means that, if only 3 or fewer factors are found to be significant, DSD can be directly used for response optimisation, hence the name *Definitive* Screening Design [97, 98]. Nevertheless, if more than 3 factors are found to be significant, DSD is still useful to find the region where the optimal conditions might be found, even if the obtained model might not accurately predict the optimal response itself [97, 98].

2.7.2. Pre-screening of DoE data

Before creating the mathematical model using data obtained from the DoE's experimental runs, it is important to pre-screen said data, as to determine if a valid model can or cannot be obtained as is, if the data needs to first be transformed, or if it needs to be discarded and the DoE setup re-evaluated. This step is particularly important when using a FFD strategy, to ensure linearity [90].

One fast way to pre-screen the obtained data is by analysing the results distribution with a histogram. The closer the data follows a normal distribution, the higher is the probability that a linear model can be obtained without needing to transform the data before analysis. If not, the shape of the histogram can be used to infer which sort of data transformation might be better suited to ensure linearity, as exemplified in Figure 9 [90, 99].

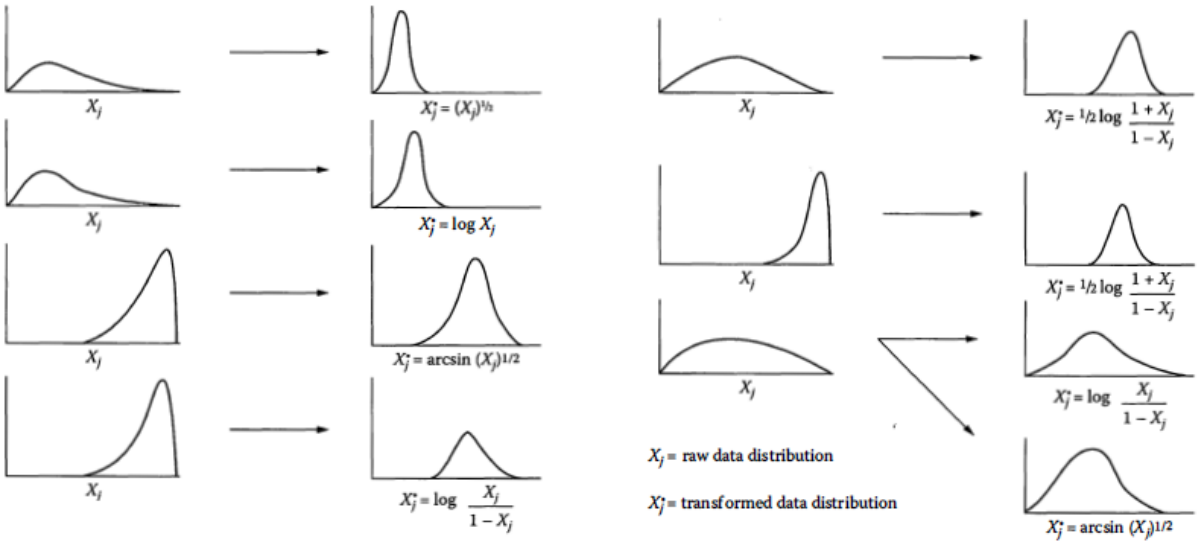

Figure 9 – Suggestions for data transformation based on original data histogram. Adapted from [99].

A simple but more in-depth pre-screening test can be done by analysing the results in a replicate plot, in which the x axis represents each individual run, while the y axis represents the results obtained during the experimental phase [90]. This test is particularly useful when centre point replicates are used. The data has a high probability of resulting in a linear model if it passes all the following criteria:

- The data from all main runs can be easily divided in a top half and bottom half.
- The data from the centre point runs is equidistant from the top half and bottom half of the main run results.
- The variability of the data from the centre point runs is lower than the variability of the data from the main runs.

If the data cannot be easily divided in two halves, it is likely that it needs to be transformed to guarantee linearity. The same is true if the data from the centre point runs is skewed towards either half of the main run results. Moreover, if the data from the centre points is outside the range of either half, it indicates that the real response shows curvature, and that a DoE approach able to calculate quadratic effects is preferable for the experiment in analysis. Finally, if the variability of the centre points is on the same level or higher than the variability of the main runs, this indicates that no valid model can be created using the obtained data, as the variability of the system is too high. If that is the case, the dataset should be discarded, and the entire experimental setup re-evaluated [90].

If the obtained data shows signs that it needs to be transformed, there are several strategies that can be used to ensure linearity, again as exemplified in Figure 9 [90, 99]. Despite not being an easy step, it is important to choose the correct transformation, if deemed necessary. Fortunately, for cases where it is not clear which transformation should be used, most specialised software for DoE analysis are able to predict which transformation should guarantee the best results. In such cases, it is recommended to use said feature.

2.7.3. Creating a DoE mathematical model

If the data obtained during the experimental runs is deemed suitable for creating a valid mathematical model, the next stage from DoE analysis involves creating said model, which take form as multivariable polynomial regressions. Specifically for this work, those models can take shape of either linear or quadratic multivariable regressions. For simplicity, this section will only focus on how to create a linear model. Equation 4 details the general formulation followed when elaborating a linear DoE model.

Equation 4 – General formulation for linear DoE mathematical models

$$Y = \beta_0 + \sum_{i}^{n} \beta_i x_i + \sum_{\substack{1 \le i \le n-1 \\ 2 \le j \le n \\ i<j}} \beta_{i,j} x_i \, x_j$$

Y = modelled response
β_0 = average response
n = number of factors
x_i = value of factor i ($-1 \le i \le 1$)
β_i = main effect coefficient of factor i
$\beta_{i,j}$ = interaction coefficient of factors i and j

The data obtained during the DoE experimental runs is used to calculate the average response β_0 and the main effect and interaction for each factor or pair of factors. The next sub-sections will detail how these can be calculated.

2.7.3.1. Calculating the average response β_0

As the name indicates, β_0 represents the average response of the experimental setup, and is calculated by averaging the results obtained during all runs from the DoE, as indicated by Equation 5.

Equation 5 – DoE average response formulation

$$\beta_0 = \bar{Y} = \frac{\sum_i^r Y_i}{r}$$

$\beta_0 = \bar{Y}$ = average response
r = number of runs
Y_i = response from run i

An interesting caveat about β_0 is that it can also be used as indicator of the linearity of the model. If β_0 is approximately equal to the average of the centre point runs, the model is most likely following a linear distribution.

2.7.3.2. Calculating the main effect coefficient β_n

Equation 6 shows how to calculate the main effect coefficient β_n for linear models.

Equation 6 – DoE main factor coefficient formulation

$$\beta_n = \frac{\overline{Y_{x_n=1}} - \overline{Y_{=x_n-1}}}{2}$$

β_n = main effect coefficient of factor n
x_n = value of factor n
$\overline{Y_{x_n=1}}$ = average response when $x_n = 1$
$\overline{Y_{x_n=-1}}$ = average response when $x_n = -1$

Figure 10 was created to help with better understanding what β_n represents. Considering a generic FFD with two factors A and B, if one wants to calculate β_n for factor A (β_A), the first step is to calculate the average response for when A is equal to – or -1, represented in blue, as well as the average response when A is equal to + or

1, represented in green. What β_A represents is the slope of a linear equation which represents how the average response varies when A is set to any value between – and +. The same is true about β_n for any factor *n*. In conclusion, the higher the magnitude of β_n is, or in other words, the steeper the slope of the line that represents how the average response changes with different values of *n*, the higher will be the effect of factor *n* on the overall DoE model.

Run	Factor	
	A	B
1	-	-
2	+	-
3	-	+
4	+	+

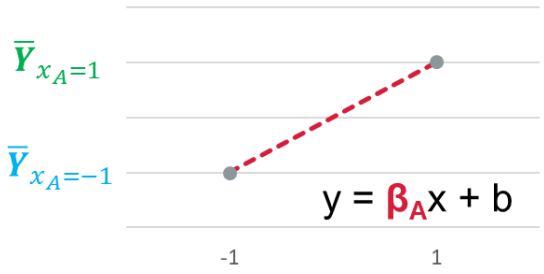

Figure 10 – Visual representation of significance of β_n.

2.7.3.3. Calculating the interaction coefficient $\beta_{m,n}$

The interaction coefficient between two factors *m* and n, $\beta_{m,n}$, is calculated in a similar manner to β_n, as shown in Equation 7.

Equation 7 – DoE interaction coefficient formulation

$$\beta_n = \frac{\overline{Y_{x_m x_n=1}} - \overline{Y_{=x_m x_n-1}}}{2}$$

β_n = main effect coefficient of factor n

x_m = value of factor m

x_n = value of factor n

$\overline{Y_{x_m x_n=1}}$ = average response when $x_m x_n = 1$

$\overline{Y_{x_m x_n=-1}}$ = average response when $x_m x_n = -1$

Likewise, $\beta_{m,n}$ can also be seen as the slope of the line that represents how the average response changes with different combinations of factors *m* and *n*, and the higher the value, the higher the effect of the interaction between said factors. Figure 11 illustrates how these combinations are represented. Essentially, while one point represents the conditions where both factors are at equal levels (both at either – or +), the other point represents the conditions where the value of each factor is at a different level. In other words, when the product of $x_A \cdot x_B$ is either a positive or negative number. Another way to interpret these conditions is to see them as the instances when the factors are in an equilibrium with one another ($x_A \cdot x_B$ is positive) or in non-equilibrium ($x_A \cdot x_B$ is negative), and so $\beta_{m,n}$ represents how the experimental response changes when both factors are in equilibrium or not.

Run	Factor	
	A	B
1	-	-
2	+	-
3	-	+
4	+	+

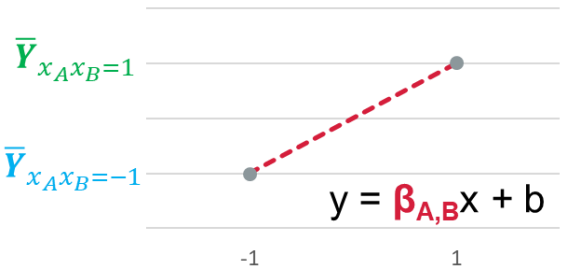

Figure 11 – Visual representation of significance of $\beta_{m,n}$.

2.7.4. Validating the DoE mathematical model

It is necessary to be aware that all models are approximations of reality and never 100% correct. If well designed, however, models obtained using DoE will always be good approximations within the region of factors being analysed. It becomes apparent that model validation is a key necessity when taking a DoE approach. While the best approach would be to compare the model to experimental

data not used for its formulation, a good alternative is to perform a group of four tests known as “Summary of Fit”. In essence, these tests use statistic principals to measure the ability of the model to predict itself and independent data points, the validity of those predictions, and how precise those predictions are. A model can be considered as valid only if it passes all four tests, which are the following [90, 94]:

I. $R^2 - Q^2 < 0.3$

For this test, three statistical concepts must be explained:

- Goodness of Fit (R^2) measures how well the model fits the raw data, or in other words, how well it can predict itself. R^2 can vary between 1 and 0, with 1 representing a perfect model [90, 94]. This is calculated following Equation 8. Alone, R^2 is not a good indicator of the validity of a model, as a model can get closer to 1 the more data points were used to formulate it.

Equation 8 – Goodness of Fit formula

$$R^2 = 1 - \frac{SS_{res}}{SS}$$

SS_{res} = residual sum of squares
SS = total sum of squares

- Predicted Residual Error Sum of Squares (PRESS) is a form of cross-validation which acts as sum of squares between one data point and the predicted response given by a model created without said data point [94, 100]. It is calculated using Equation 9.

Equation 9 – Predicted Residual Error Sum of Squares formula

$$PRESS = \sum_{i=1}^{n} (y - \hat{y}_{i,-i})^2$$

$\hat{y}_{i,-i}$= predicted response of i by model created without i

- Goodness of Prediction (Q^2 or R_{pre}^2) is an estimate of the prediction power of the model [90, 94]. In other words, it estimates how well the model can predict independent data points. Like R^2, a Q^2 value of 1 represents a perfect model, but unlike R^2, Q^2 might reach negative levels if the model is of low quality. This estimate is calculated following Equation 10.

Equation 10 – Goodness of Prediction formula

$$Q^2 = 1 - \frac{PRESS}{SS}$$

SS = total sum of squares

When both R^2 and Q^2 are of high value and the difference between those values is lower than 0.3, it means that the model can predict both itself and data points not used for its formulation.

II. $Q^2 > 0.5$

As it is possible to deduce from Equation 10, Q^2 can be seen as an estimate of the power of a dataset to estimate one of its data points when said point is discarded when creating a model. When Q^2 is higher than 0.5 it indicates that it can accurately predict points not used during its formulation.

III. Validity > 0.25

This statistical test is based on the lack-of-fit test carried out as part of the ANOVA evaluation, and it is calculated using Equation 11 [90, 94]. If the value is higher than 0.25 it means the model passed the lack-of-fit test and that the predicted results should be accurate.

Equation 11 – Validity formula

$$Validity = 1 + 0.57647 * \log(p_{lof}) \quad \left| \; p_{lof} = \text{p-value for lack of fit test.} \right.$$

One important thing to note is that due to how the lack-of-fit test is conducted, it might not be possible to calculate validity when using specific DoE approaches. For example, the design matrix for DSD does not have enough runs for this test to be performed.

IV. Reproducibility > 0.5

This statistical test is based on the pure error test carried out as part of the ANOVA evaluation, and it is calculated using Equation 12 [90, 94]. In DoE, the pure error is calculated by analysing the variation of responses under the same conditions, usually the centre point of the design. If reproducibility is higher than 0.5, it means the pure error of the system is low, and the results obtained are reproducible.

Equation 12 – Reproducibility formula

$$Rep = 1 - \frac{MS_{pure\ error}}{MS_{total\ SS\ corrected}}$$

Rep = Reproducibility
MS = Mean squares, or variance

2.7.5. Optimising the DoE mathematical model

In DoE, model optimisation can be seen as the process of simplifying the obtained mathematical model as to only include the most statistically significant factors and interactions [90, 94]. While the specific process depends on the design strategy chosen, optimising a DoE model should adhere to the following principles [90, 94]:

- The model must pass all Summary of Fit tests.
- The model must include all main factors, interactions and quadratic effects that are deemed statistically significant.
- If the interaction between two factors is deemed statistically significant, the main effect of both factors must be present in the model even if said main effects are not significant.
- If the quadratic effect of one factor is deemed statistically significant, the main effect of said factor must be present in the model even if said main effect is deemed not significant.

The next subsections will detail the methods used to optimise a model for DoE's following a FFD and a DSD strategy.

2.7.5.1. Optimising a Full Factorial Design mathematical model

The process for optimising a Full Factorial Design model is based on the null hypothesis testing obtained from the ANOVA results obtained while analysing the DoE model. If the null hypothesis for any main factor or interaction between factors is rejected, said factors or interactions are deemed statistically significant and must be part of the optimised models. Any other factor should be included only if needed for the model to adhere to the principles set in section 2.7.5. The new model should then be re-evaluated. This process must continue until it is not possible to simplify the model anymore without breaking the forementioned principles [90].

Depending on the software used for DoE analysis, this process might also be available as an easy to interpret graph. For example, when using the software *Minitab*, the null hypothesis is represented as a reference line in the Pareto chart of the standardised effects. If the standardised value of a specific effect is above the reference line, then the null hypothesis for that effect was rejected and can be considered as statistically significant. An example of this analysis can be seen in Figure 12.

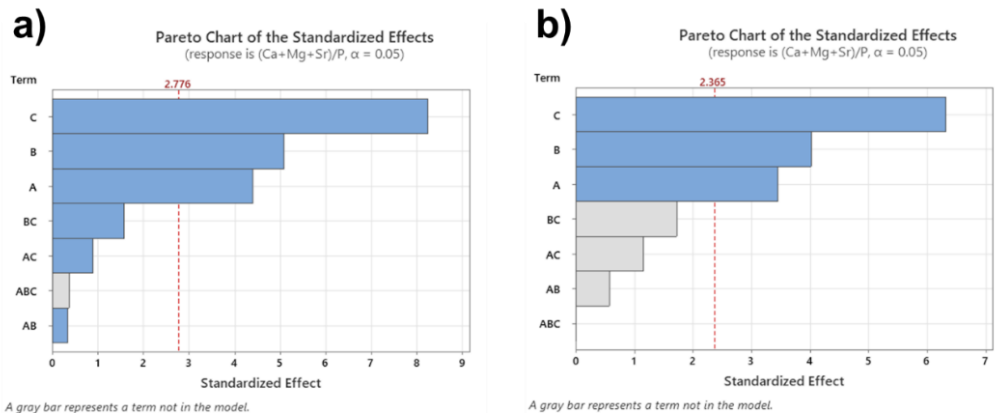

Figure 12 – Full factorial design Pareto chart analysis: a) before model optimisation; b) after model optimisation.

2.7.5.2. Optimising a Definitive Screening Design mathematical model

Like with a FFD model, optimising a DSD model is also based on the null hypothesis results obtained from ANOVA. However, due to the supersaturated nature of DSD, it is not possible to test all effects at the same time [97, 98]. Moreover, during the initial steps of optimisation it might be hard to obtain a model able to pass the three Summary of Fit tests one can perform with a DSD approach (see section 2.7.4), or one in which any of its effects seems to be statistically significant (see Figure 13).

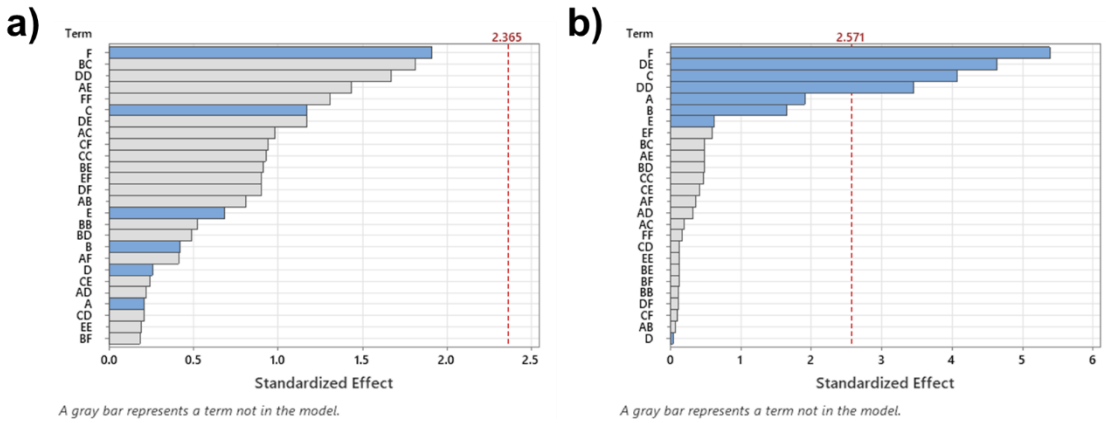

Figure 13 – Definitive screening design Pareto chart analysis: a) initial optimisation step; b) optimised model.

One useful strategy to optimise DSD analysis passes through using a hierarchical approach based on the principle that any interaction and quadratic effect of any factor deemed significant necessitates the presence of the main effect of said factor in the final model. When using the software *Minitab*, the strategy can be summarised as the following [97, 98]:

- Create a model using only main effects.
- Analyse the Pareto chart of standardised effects to determine which quadratic effects might have a significant effect on the final optimised model. Create new model with said quadratic effects.
- Analyse the new Pareto chart. Remove any quadratic effect that, after second inspection, might not have a significant effect. Add any interaction effect that might have a significant effect, without supersaturating the model (if supersaturated, software will not present Pareto chart for all possible effects)
- Optimise model using the same rules stated in 2.7.5.1 for FFD models.

While this strategy is not flawless and might need to be revised during analysis, it still is a reasonably effective strategy for the optimisation of DSD models [97, 98]. Regardless of strategy followed, if the principles set in section 2.7.5 are met, then the DSD model can be considered as optimised. In this project we will use DoE to systematically optimise the coating technology.

III. Project Aims and Objectives

The principle aim of this project was to develop a composite TiO_2/sHAP sol-gel coating for spinal fusion cages, to improve their ability to bond with two adjacent vertebrae and, consequently, improve the outcome of spinal fusion surgery. It was hypothesised this combination of materials and coating technique would amplify their individual strengths and result in a coating with similar or enhanced osteogenic behaviour compared to solutions already available in the market, at lower production costs.

To achieve this aim, the project was divided into the following objectives:

I. Serum-free expansion and differentiation of human mesenchymal stem cells:
   a. Compare serum-free media to serum-containing standards for the expansion of primary human MSCs and an immortalised human MSC line.
   b. Compare serum-free media to serum-containing standards for the osteogenic differentiation of immortalised human MSC line.
   c. Select the most appropriate culture conditions that lead to clear signs of osteogenic differentiation. These conditions will be used to assess the biological performance of the materials developed during objectives II and IV.

II. Synthesis of Mg- and Sr-substituted hydroxyapatite by wet chemical precipitation:
   a. Investigate the window of conditions that allow for the synthesis of sHAP with different substitution degrees.
   b. Use DoE to infer optimal sHAP synthesis conditions, based on real substitution degrees, HAP phase quantification, crystallinity, and in vitro biological performance.

c. Compare the real performance of optimal sHAP to its theoretical performance as predicted by the obtained DoE models.

III. Synthesis of crystalline TiO_2 at low sintering temperatures:
   a. Investigate the window of conditions that allow for controlled synthesis of TiO2 using sol-gel chemistry.
   b. Use DoE to infer optimal synthesis conditions that allow TiO_2 to crystallise into anatase at low sintering temperatures by quantifying the post-sintering organic residues, anatase phase quantification and crystallinity.
   c. Compare the real performance of optimal synthesis conditions to its theoretical performance as predicted by the obtained DoE models.

IV. Development of composite TiO_2/sHAP coatings for spinal fusion cages:
   a. Investigate the window of conditions that allow for the deposition of TiO_2/sHAP layers onto a given substrate using sol-gel chemistry and the dip coating technique.
   b. Explore possible pre-treatments that would improve coating adhesion onto Ti-6Al-4V and PEEK substrates.
   c. Use DoE to infer optimal coating conditions using the optimised TiO_2 settings from objective 3 and commercially available sHAP. Optimisation based on mechanical performance, crystal phase quantification and in vitro biological performance.
   d. Compare the real performance of optimal coating to its theoretical performance as predicted by the obtained DoE models, and to coatings synthesised using the sHAP optimised during objective II.

IV. Materials and Methods

4.1. Materials

All reagents were purchased from Sigma-Aldrich unless stated otherwise. All cell culture plastics, including T75 flasks and well plates, were obtained from Thermo Fisher Scientific.

4.2. Methods

4.2.1. Preparation of expansion and osteogenic media

4.2.1.1. Preparation of α-MEM and DMEM expansion media

To prepare α-MEM and DMEM expansion media (EM), 50 ml of Foetal Bovine Serum (FBS) should be added to the 500 ml media bottle in sterile conditions. This resulted in expansion media supplemented with 10% (v/v) FBS. Penicillin-Streptomycin (PS) antibiotic stock solution was then added to the media to control possible bacterial or fungal contaminations. If the media did not contain glutamine, a PS-Glutamine (PSG) solution should be added instead. The final PS or PSG concentration should be 1% (v/v). The final media was aliquoted in sterile 100 ml cups and stored in the fridge until necessary.

4.2.1.2. Preparation of Serum-free expansion media

Regardless of the supplier, the serum-free media used during this work was shipped as kits with separated bottles for the base media and for the media supplement. To prepare serum-free EM, first, it was necessary to add to the media

its specific supplement in sterile conditions. PS antibiotic stock solution was then added in a final concentration of 1% (v/v). The final media should be aliquoted in sterile 100 ml cups and stored in the fridge until necessary. If required by the supplier's instruction, the media should be stored protected from light, by wrapping the aliquots with aluminium foil.

4.2.1.3. Preparation of human-serum expansion media

As the human serum that serves as its supplement was already included in the media as is, to prepare human serum EM it was only required to add PS antibiotic stock solution in a final concentration of 1% (v/v). The final media should then be aliquoted in sterile 100 ml cups wrapped in aluminium foil to protect the media from light as instructed by the media's supplier. The aliquots should be stored frozen at −20°C up until their first use, after which they should be stored in the fridge.

4.2.1.4. Preparation of osteogenic media

To prepare osteogenic media OM, stock solutions of ascorbic acid 2-phosphate (AA2P, 5 mg/ml), beta-glycerolphosphate (βGP, 0.5 M) and dexamethasone (DEX, 10 μM) should be added to any of the previously prepared expansion media in an EM/AA2P/βGP/DEX ratio of 100/1/1/1 in volume. The OM aliquots should then be stored as instructed by the suppliers of the EM used in the preparation of the new media.

4.2.2. General cell expansion and passaging

Cell expansion started by thawing a vial of cryopreserved cells as required (each vial containing 1 ml cell suspension with 1 million cells), resuspending the cells in 9 ml of FBS-containing media and centrifuging the 10 ml cell suspension for 5 minutes at 1000 rpm. The supernatant should then be discarded, and the cells resuspended once again in the EM of choice. To accommodate their different growth rates, cells from primary sources should be resuspended in 10 ml of EM, while immortalised cells should be resuspended in 20 ml. The new cell suspension should be then transferred to T75 cell culture flasks (10 ml in each T75), which should then be placed in an incubator set to 37°C and 5% CO_2. Cells should expand until ≈ 90% confluent, change media either every 2-3 days if using serum-containing media, or once every week if using serum-free media.

When cells become ≈ 90% confluent, the media should be discarded, the cells washed twice with 10 ml of Hank's Balanced Salt Solution (HBSS) and detached using 5 ml of trypsin-EDTA solution. After 5 minutes, 10 ml of FBS-containing media should be added to stop the effect of the trypsin solution, and the new cell suspension transferred to a 50 ml falcon tube. After counting the cells with a haemocytometer, three routes can be taken:

- Cells should be seeded in new T75 as stated above to continue expansion.
- Cells should be resuspended according to the specifications of the *in vitro* assay being conducted.
- Cells should be resuspended in cryopreservation media (90% FBS, 10% dimethyl sulfoxide) in a cell density of 1 million cells/ml and stored first at −80°C and then in liquid nitrogen until further use.

4.2.3. Protein-based coating of well plates

The wells from a 24-well plate can be coated with either gelatine (0.1% w/v) or bovine fibronectin (10 µg/ml) stock solutions by adding 126.7 µm of the required solution to the intended wells and incubating for at least 30 minutes or 1 hour, respectively. The stock solutions should then be discarded from the coated wells by aspiration.

4.2.4. General *in vitro* testing

In vitro tests were conducted in either 24 or 48-well plates. Unless stated otherwise, cells were seeded in 800 µl of media when in a 24-well plate, or 500 µl in 48-well plates, with the media changes required by each experimental set-up. Cell seeding density depended on the cell type in use: human MSCs from a primary source were seeded with a density of 10000 cells/cm^2, while Y201 hTERT-MSCs [83] were seeded with a density of 4000 cells/cm^2. The seeded plates were placed in an incubator set to 37°C and 5% CO_2 and only removed when necessary for analysis or media change.

4.2.5. Measurement of cell metabolic activity through resazurin reduction assay

To measure the metabolic activity of cells at a specific time point it was first necessary to adjust the volume of cell culture media to 720 µl, then add 80 µl of resazurin salt stock solution (1 mM) to form the working solution. As the assay is light-sensitive, the assay was conducted while covering the culture plates being analysed with aluminium foil. The covered plate should then be placed in an incubator set to 37°C and 5% CO_2 for 2 hours.

After the assay was incubated for 2 hours, the working solution of each condition was added to 96-well plates in 200 µl triplicates in a staggered pattern as exemplified in Figure 14. The plates containing the triplicates were analysed in a plate reader (Tecan infinite 200-pro) and fluorescence was measured at λ_{ex}: 540 nm and λ_{em}: 590 nm. The average metabolic activity was considered as the average fluorescence (arbitrary unit or au) of the triplicates of each condition.

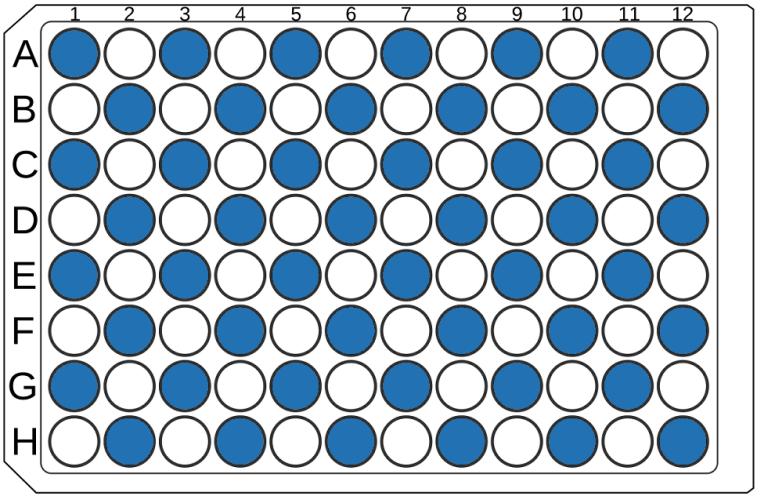

Figure 14 – Staggered pattern for measuring resazurin reduction assay. This pattern reduces excitation from neighbouring wells.

After analysis, the cell plates should be washed twice with HBSS, after which two steps could be taken:

- Add the required volume of media to continue cell culture (see 4.2.4).
- Prepared to be lysed as stated in 4.2.6.1.

4.2.6. Measurement of DNA-adjusted Alkaline Phosphatase activity

4.2.6.1. Preparation of cell lysates

To prepare the cell lysates, first, the cell plates were washed twice with HBSS. The cell digestion buffer (CDB) was prepared by mixing ultrapure water, stock cell assay buffer (CAB) and Triton X-100 in an H_2O:CAB:Triton ratio of 100:10:1 in volume. The volume of CDB added to each well depended on the type of well plate used: 1 ml/well for 24-well plates, and 0.5 ml/well for 48-well plates.

To properly lyse the cells, the plates were stored first in the fridge for 30 minutes, after which they were subjected to at least three freeze/thaw cycles at -80°C and 37°C, respectively. After the last cycle, the lysates were transferred to 1.5 ml Eppendorf tubes, to be stored at -80°C until necessary. Before being analysed, the lysates were thawed at 37°C and centrifuged at 10000 rpm for 5 minutes.

4.2.6.2. DNA quantification

DNA was quantified through colorimetry using a Quant-iT® high-sensitivity dsDNA assay kit. To prepare the assay buffer, the Quant-iT® reagent was diluted in Quant-iT® assay buffer in a reagent:buffer ratio of 1:200 in volume. Then, 10 µl of lysate was added in triplicate to a black 96-well plate, to which 90 µl of assay buffer was added. The analysis was performed by setting the plate reader to shake the plate for 10 seconds with a linear amplitude of 1 mm, incubating for 10 minutes, shake once again for 10 seconds under the same conditions, and finally measuring fluorescence at λ_{ex}: 485 nm and λ_{em}: 535 nm. Fluorescence was converted to ng DNA with a standard curve created using the standard solutions provided by the assay kit.

4.2.6.3. Measuring alkaline phosphatase activity

Alkaline phosphatase (ALP) activity was measured through colorimetry using a Pierce™ pNPP Substrate Kit (Thermo Scientific). The assay buffer was prepared by dissolving one 5 mg para-nitrophenol phosphate (pNPP) tablet per 5 ml of 20 vol% diethanolamine buffer in ultrapure water. Then, 10 µl of lysate was added in triplicate to a 96-well plate, to which 90 µl of assay buffer are added. The well plate is incubated until a colour change from transparent to yellow is noticed or 30 minutes have passed. The assay is conducted in a plate reader set to measure absorbance at 405 nm and 25°C every minute for 30 minutes. Each absorbance unit represents 19.75 nmol of para-nitrophenol (pNP), and total ALP is measured as the slope of the linear regression calculated for the measured results.

To better compare the results from different conditions, ALP activity should be normalised by dividing total ALP by the DNA quantity measured as stated in 4.2.6.2, resulting in DNA-adjusted ALP activity.

4.2.7. Wet chemical precipitation of hydroxyapatite

To synthesise HAP by wet chemistry precipitation, two solutions had first to be prepared, one basic and one acidic.

The basic solution was prepared as follows: in a 1000 ml beaker, calcium hydroxide was added to ultrapure water and kept under strong stirring. If required, the Mg and Sr precursors were added to 100 ml of ultrapure water, in separate 250 ml beakers and kept under stirring. Once the precursors were dissolved, the 100 ml solutions were added to the calcium hydroxide one. If also required, ammonia solution 28% was added to the final solution as well. In the end, the combined volume of ultrapure water and ammonia solution should be 500 ml. The final solution

was then transferred and kept under strong stirring in a closed 4-neck round flask kept in a water bath set to 40°C, as shown in Figure 15.

The acidic solution was prepared by adding orthophosphoric acid to 500 ml of ultrapure water, under stirring. Once all the acid had been diluted, the solution was transferred to a dropping funnel placed in one of the necks of the round flask containing the basic solution, as also shown in Figure 15.

Figure 15 – HAP wet chemical precipitation setup.

Once the internal temperature of the basic solution reached 40±2°C, the dropping funnel was open as to add the acidic solution to the basic one with a rate of 1 drop/sec. Once all the acidic solution was added, the dropping funnel was removed, the respective neck from the round flask closed, the water bath set to 37°C, and the mixture left under stirring overnight. On the following day, the obtained precipitate was submitted to one of the washing processes detailed in sections 4.2.8 and 4.2.9 to remove any traces of ammonia and unreacted reagent. The washed precipitate was then transferred to a large glass petri dish and dried in an oven (FD Series 9010-0082, Binder) overnight at 40°C. Finally, the dried precipitate was collected for further analysis.

4.2.8. Washing with centrifugation

To wash the synthesised HAP using centrifugation, the 4-neck round flask was removed from the water bath and kept without any stirring for up to 24 hours, allowing the synthesised material to precipitate at the bottom of the flask, after which the supernatant was removed.

For the first washing cycle, 45 ml of the precipitate was transferred to 50 ml Falcon tubes, until no precipitate was left. If there was less than 45 ml of the precipitate left, ultrapure water was added to the last tube until 45 ml was reached. The Falcon tubes were then placed in a bench-top centrifuge (XS R-8D, Remi group), programmed to work at 6000 rpm (5070 rcf) for 10 minutes. After centrifugation, the supernatant in each of the falcon tubes was discarded.

For all remaining washing cycles, the Falcon tubes were filled with ultrapure water up to 45 ml and the precipitate was resuspended manually using a spatula and shaking. The new suspensions were then centrifuged as previously stated. After the final washing step, the precipitate was dried as stated in section 4.2.7.

4.2.9. Washing with vacuum filtration

The setup for washing the synthesised HAP through vacuum filtration can be seen in Figure 16. A 2 l Büchner flask was connected to a vacuum pump, and a Büchner funnel with an internal diameter of 125 mm was placed on top of the flask. A paper filter of the same diameter was then placed in the funnel, and an overhead stirrer was carefully placed to not touch the filter. The vacuum pump and overhead stirrer should be turned on before starting the washing process.

Before washing, the HAP suspension should be divided into two batches of 500 ml each. The first washing step involved gradually adding one of the batches to the Büchner funnel and leaving the vacuum pump working until all liquid had been drained from the suspension. Afterwards, the pump was turned off, the filtrated liquid and paper filter discarded, and the precipitated HAP collected and resuspended in 500 ml of ultrapure water in a 1000 ml beaker for 10 minutes under constant stirring.

This washing process was repeated at least three times, always using a new paper filter. After the final washing step, the precipitate was dried as stated in section 4.2.7.

Figure 16 – Vacuum filtration set-up.

4.2.10. Fourier-transformed Infrared Spectroscopy

For the FTIR analysis, 100 mg of KBr was mixed with a sample of the materials being analysed weighing between 0.5 and 1.0 mg. The mixture was then manually ground until a fine powder was obtained and pressed into a disk in a hydraulic press. The disk was then analysed in a FTIR equipment (Smart Omni-Transmission Nicolet IZ10, Thermo Fisher) performing 64 scans with a resolution of 4 cm^{-1} by measuring absorbance.

4.2.11. Cell culture in indirect exposure to hydroxyapatite

To culture cells in indirect exposure to HAP, first, it was necessary to prepare sterile HAP suspensions. These suspensions were prepared in 50 ml falcon tubes by adding HAP which had been sterilised with gamma radiation by an external partner to sterile ultrapure water such as the final concentration equals 10 g/ml. The suspensions were then subjected to cycles of 30 minutes in an ultrasound bath followed by 1 minute in a vortex mixer until a homogeneous suspension is achieved.

The next step was to seed Y201 cells in 24 well plates in 720 µl of serum-free EM, as stated in section 4.2.4. After two or three days from seeding, a well insert with 1 µm pore size (cellQART®) was added to each well and 80 µl of a specific HAP suspension was added to the well insert. This resulted in a HAP concentration of 1 g/ml in each well. Before being added to the insert, the HAP suspension should be vortex mixed for 1 minute to resuspend any possible precipitate. Figure 17 exemplifies the experimental setup. Cell culture should resume as usual, with full media changes once a week.

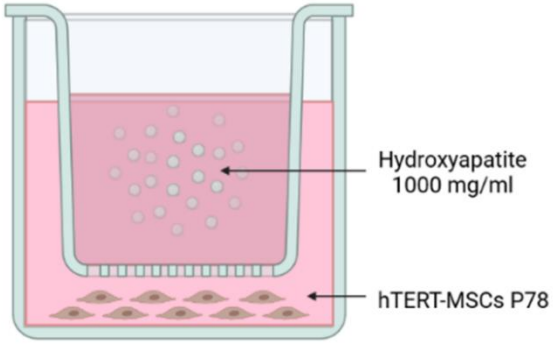

Figure 17 – Schematic for the indirect culture of hTERT-MSCs Y201 exposed to hydroxyapatite. Image created on www.biorender.com.

4.2.12. Sol-Gel synthesis of titanium dioxide

To synthesise TiO_2 by sol-gel chemistry, 3.9 ml of titanium isopropoxide (TTIP) was first added to anhydrous ethanol (EtOH) in a 100 ml beaker and left under stirring for 10 minutes at room temperature, on a hotplate with magnetic stirring. Then, acetic acid glacial (AcOH) was added to the TTIP-EtOH solution and left under stirring for 10 minutes. Ultrapure water was used to start the hydrolysis of TTIP, added drop-by-drop with a Pasteur pipette. The reaction temperature was set and controlled using the hotplate's thermometer adapter and measuring the temperature of 40 ml of ultrapure water on a 50 ml beaker covered with aluminium foil. The sol-gel beaker was also covered with aluminium foil punctured at the centre, and the reaction left to occur under stirring for 24 hours. The experimental setup is shown in Figure 18.

Figure 18 – Set-up for the sol-gel synthesis of TiO_2.

After 24 hours, the sol-gel beaker was uncovered and left to evaporate overnight. After drying, the obtained material was subject to a sintering process. Finally, the sintered material was collected for further analysis.

4.2.13. Waterjet cutting of Ti-6Al-4V and PEEK substrates

Before cutting, two different types of substrates were designed in the software *AutoCAD*. Both designs consisted of a circular region with a diameter of either 15.0 mm or 7.5 mm and a handle with a 1.0 mm width. The circular region was the substrates testing area, while the handle was there to facilitate the coating process, being discarded with the use of a metal-cutting plier. The substrates had a total length of 40 mm, the exception being PEEK substrates with d = 15.0 mm, which had a total length of 30 mm. To facilitate the cutting process, the substrates were arranged in rows, connected with a horizontal bar also with a 1 mm width. Examples of the cut substrates can be found in Figure 19. Plates of Ti-6Al-4V (250 mm x 250 mm x 1 mm) and PEEK (250 mm x 250 mm x 5 mm) were cut using a water jet cutter (ProtoMAX, OMAX) using the built-in specifications for each material. After cutting, the samples were washed with water and dried at room temperature.

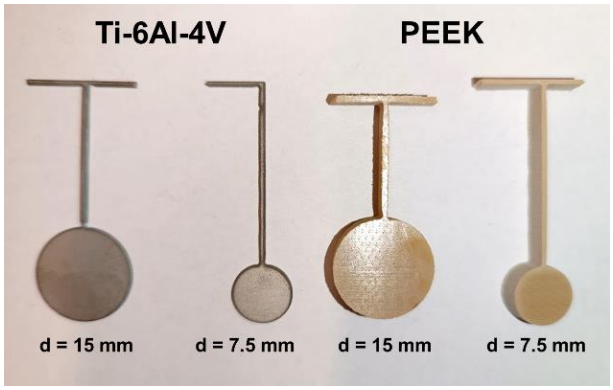

Figure 19 – Examples of substrates cut from Ti-6Al-4V and PEEK plates with a water jet cutter.

4.2.14. Air-plasma treatment of Ti-6Al-4V and PEEK substrates

Before being submitted to an air-plasma treatment, the Ti-6Al-4V and PEEK substrates were cleaned with a 70% isopropanol wipe and dried at room temperature. The cleaned substrates were then placed in the chamber of an air-plasma equipment (Zepto, Diener). The vacuum pump connected to the equipment was then turned on, letting pressure inside the chamber decrease to 0.2 mbar, being then adjusted to 0.8 mbar. Next, the power (maximum 100 W) and timer (in seconds) required were set, and the plasma turned on, which automatically shuts down when the timer runs out. Finally, the vacuum pump was turned off, ventilation turned on and the samples removed from the equipment's chamber. The treated substrates were kept covered in aluminium foil until required.

4.2.15. Dip coating different substrates with TiO_2/hydroxyapatite sol-gel composite

The first step of the dip coating process was to prepare the TiO_2/HAP sol-gel composite. This was done by following the protocol set in 4.2.12, with the following adjustments:

- Before starting hydrolysis, the required amount of HAP was added to the solution and left under stirring until all HAP has been suspended. If necessary, the suspension could be submitted to as many 15-minute ultrasonic baths as required for the HAP to fully disperse.
- After the 24-hour incubation period, the volume of the obtained sol-gel composite was adjusted to 40 ml with EtOH and then transferred to a 50 ml Falcon tube until necessary.

Before coating, the substrate was cleaned with 70% isopropanol wipes and submitted to an air-plasma treatment (see 4.2.14). The substrate was then submitted to the required number of coating cycles, with each cycle involving:

1. Dipping in a 100 ml beaker containing the 40 ml TiO_2/HAP composite, for up to 5 minutes.
2. Drying on a hotplate set to 70°C for 5 minutes.
3. Consecutive dipping in two 100 ml beakers containing 60 ml of ultrapure water for 1 minute.
4. Drying on a hotplate set to 70°C for 5 minutes.

Each cycle resulted in one coating layer being deposited into the substrate. The coating process was performed manually or using a robotic arm (Tinkerkit Braccio, Arduino), as seen in Figure 20. The robot arm was programmed using the software *Arduino IDE* according to the specifications set by the experimental protocol. The coated substrates were then sintered at 250°C for six hours in an oven (LHT 6/30 + 3016 controller, Carbolite Gero) at specific heating rates. Finally, the sintered coated samples were cleaned first in an ultrasonic bath while immersed in 25 ml of ultrapure water inside a 50 ml falcon tube, then with a 70% isopropanol wipe and left to dry at room temperature.

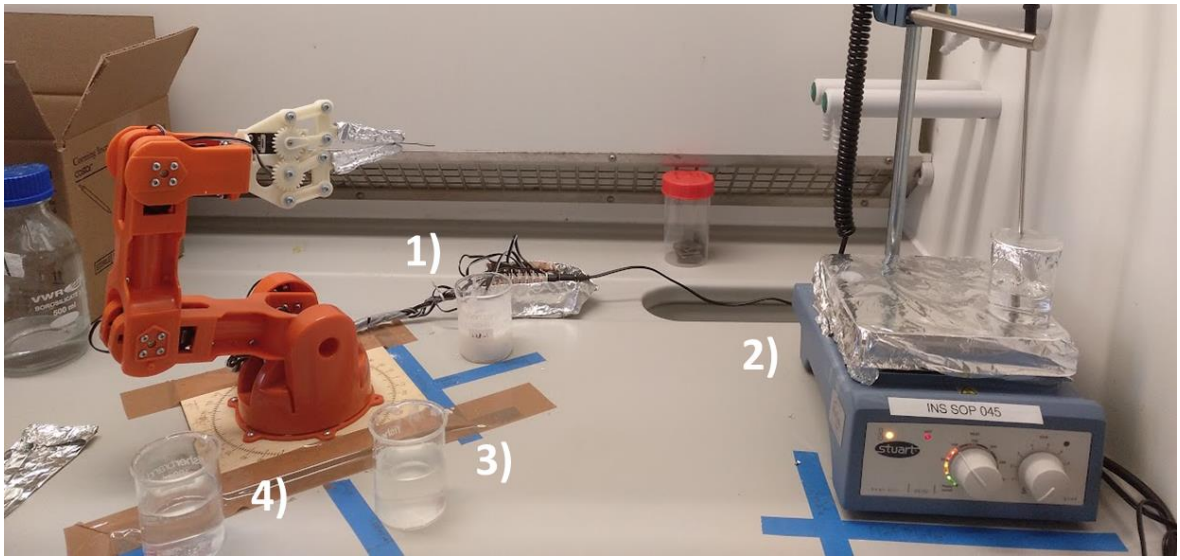

Figure 20 – Automatic coating set-up: 1) TiO_2/HAP composite dip; 2) first and second drying steps; 3) first washing step; 4) second washing step.

4.2.16. Thermogravimetric Analysis with Differential Scanning Calorimetry

This method was used in sol-gel TiO_2 samples synthesised and analysed at Fin-ceramica Faenza SpA. TGA and DSC were performed in a TGA/DSC 3+ STAR^E System (Mettler Toledo), with the ability to automatically analyse up to 33 different samples. Before analysis, each sample pan was tared using the equipment's software, after which 10 to 20 mg of sample were added. The equipment was set to analyse each sample with pans without lids, in a pure oxygen atmosphere, with nitrogen used as a cooling atmosphere. Both atmospheres had their airflow set to 80 ml/min. Analysis occurred between 30 to 550°C with a heating rate of 10°C/min. Before analysis, the equipment was set to analyse an empty pan, as to detect any possible problem. As results, it was obtained a sample weight (mg) curve from TGA, and a heat flow ($W \cdot g^{-1}$) curve, obtained from DSC. The results were analysed using the *TA Universal Analysis* software to identify and quantify weight loss steps, as well as to identify heat flow peaks.

4.2.17. Thermogravimetric Analysis

This method was used in sol-gel TiO_2 samples synthesised and analysed at The University of Sheffield. TGA was performed in a Q500 TGA equipment (TA Instruments), which can analyse one sample at a time. Before each analysis, the sample pan was tared using the equipment's software, after which 15 to 50 mg of sample were added. The equipment was set to analyse the sample in two atmospheres: in nitrogen from 30 to 50°C, and in oxygen from 50 to 550°C. For both atmospheres, heating rate was set to 20°C/min, and air flow to 80 ml/min. Before analysis, the equipment was set to analyse an empty pan, as to detect any possible problem. As results, it was obtained a weight (%) curve and a derivate weight (%/°C) curve, both from TGA. The results were analysed using the *TA Universal Analysis* software to identify and quantify weight loss steps, as well as to identify derivate weight peaks.

4.2.18. X-Ray Diffraction and calculation of crystallinity

This method was used in samples synthesised and analysed at The University of Sheffield. XRD analysis was performed in an Aeris Benchtop XRD System (PANalytical), with the ability to automatically analyse up to 6 samples. Powdered samples were placed in metallic sample holders. The Incident optics were the following: Cu tube 30 kV 40 mA; ¼° divergence slit; 0.15 mm Ni filter; 0.02 Rad Soller slits. The data was analysed using the software *Profex 4.3* and *Origin 2019b*, and crystallinity determined as the ratio between the sum of the area below the identified crystalline peaks and the total area below the obtained XRD graph.

4.2.19. Cell culture in Ti-6Al-4V and PEEK substrates

The Ti-6Al-4V or PEEK substrates, previously sterilised by immersion in 70% ethanol, were left to dry in sterile conditions, after which they were placed in a non-treated 24-well plate and immersed in 800 µl of serum-free EM for a minimum of 30 minutes in a cell incubator at 37°C and 5% CO_2. During this time, a Y201 cell suspension was prepared as to have all necessary cells for each substrate in a specific volume of media (80 µl for substrates with d = 1.50 cm; 40 µl for substrates with d = 0.75 cm). As a reminder, seeding density should be of 4000 cells/cm^2 for Y201 cells. After the incubation time was over, the media was removed from the wells and the seeding media was carefully added to only cover the surface of the substrate, as seen in Figure 21. The seeded plates are placed once again in the cell incubator and checked every 15 minutes for 45 minutes, topped with half of the seeding volume of EM if required. Then, the wells were topped with 800 µl of EM, as also represented in Figure 21, for 2 days.

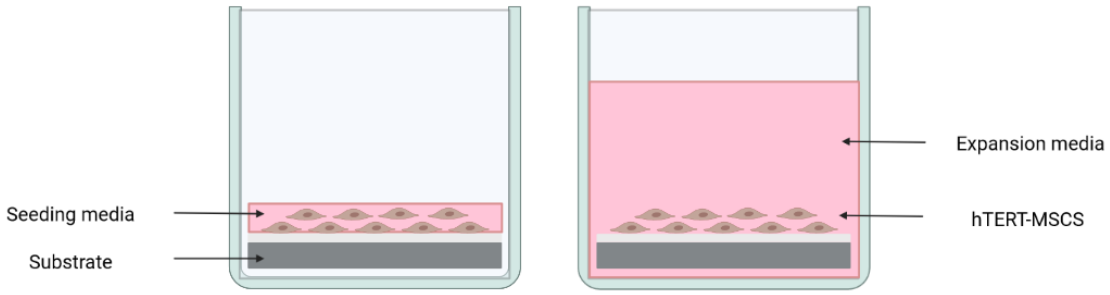

Figure 21 – Schematic of the Y201 seeding process in Ti-6Al-4V and PEEK substrates. The seeding media only occupies the surface of the substrate. Expansion media is added 45 minutes after initial seeding. Image created on www.biorender.com.

Two days after seeding, the substrates were transferred to a different non-treated 24-well plate and topped once again with 800 µl of EM. Cell culture should resume as usual, with full media changes once a week.

V. Serum-free expansion and differentiation of human mesenchymal stem cells

5.1. Introduction

By definition, an osteoinductive material is able to recruit mesenchymal stem cells (MSCs) into its surface and induce their differentiation into osteoblasts, leading to bone formation regardless of where it is implanted [76]. With said definition in mind, it becomes clear that MSCs present themselves as the most relevant cell type for testing the biological performance of possible osteoinductive solutions *in vitro*. MSCs are, however, a difficult cell type to culture, due to their heterogeneous nature, variability of sources from within the same individual and loss of differentiation potential with increasing cell passage [78, 101]. As such, it is of utmost importance to find MSC culture conditions that minimise any problem derived from the cell type and increase the quality of the obtained results.

One main issue when defining culture conditions for MSCs is finding the correct cell culture media for both MSC expansion and differentiation. The heterogeneous nature of MSCs makes it difficult to find a culture media which can perform similarly even with cells from the same donor but different extraction sites [87], a problem which can be further amplified by the inherent variability that occurs in traditional cell culture conditions, in which culture media is supplemented with foetal bovine serum (FBS) [86, 87]. In fact, despite being considered a good supplement for cell expansion, its undefined nature means that FBS from different sources can lead to different results during *in vitro* cell work [86, 87, 102]. FBS can, however, be substituted by serum-free alternatives which present better-defined compositions and, as such, result in much more reproducible culture results [87, 89]. These serum-free media (SFM) can be supplemented with well-characterised nutrients alongside purified proteins, hormones, cytokines and growth factors of animal, human or recombinant sources [87, 89]. There even are SFM specifically formulated to minimise variability in MSC culture [87].

Another possible issue stems from the source of the cells themselves, generally derived from primary sources or immortalised cell lines [81, 83, 84]. While better representations of the *in vivo* environment, primary cells from different donors or sources can behave differently to the same culture conditions and are prone to lose their characteristics with increasing passage number [78, 81, 83, 87]. These issues can lead to non-reproducible *in vitro* results. On the other hand, immortalised cell lines retain their characteristics regardless of passage number, allowing for much more reproducible results to be obtained. However, the mechanisms that allow these cells to keep their characteristics also make them less representative of healthy *in vivo* environments [81, 83, 84]. Nevertheless, their less variable behaviour makes these cells useful for projects of long duration, even if testing with primary cells should always be considered as a final step for *in vitro* biological evaluation [85].

Due to the necessity for cell-culture conditions that lead to consistent results for the duration of the entire PhD period, the work presented in this chapter aims to study the use of both SFM and an immortalised MSC line for studying the *in vitro* biologic performance of the various materials developed during the present thesis.

5.2. Aims and Objectives

This chapter aimed to develop a general cell culture protocol for serum-free expansion and osteogenic differentiation of an immortalised MSC line, to serve as the basis for the *in vitro* biological testing of the materials developed in Chapters VI and VIII. Different serum-free media will be compared to standard FBS-containing media as well as specialised media for MSC expansion supplemented with human serum. The different media will be tested in both primary and immortalised cells, with a larger focus on optimising the culture conditions of the immortalised cell line. To achieve this goal, the following objectives were addressed:

I. Studying the expansion of human MSCs from primary sources in different cell culture media and substrates.
II. Studying the expansion of immortalised human MSCs in different cell culture media and media change protocols.
III. Optimising the osteogenic differentiation conditions of immortalised MSCs in serum-free media.

5.3. Materials and Methods

The following Materials and Methods are specific to this chapter. For general details please check Chapter IV.

5.3.1. Expansion of human MSCs in different cell culture media and substrates

Human MSCs from a primary source (obtained from Lonza) stored at passage 3 were initially expanded in T75 flasks using BM1 media (see Table 9) as detailed in 4.2.2. The expanded cells were then resuspended and seeded in three different 24-well plates, each following one of the following conditions:

- **N/C –** well plate without protein-based coating.
- **GEL –** well plate coated with gelatine (see section 4.2.3)
- **FIB –** well plate coated with bovine fibronectin (see section 4.2.3)

For each well plate, the human MSCs, now on passage 4, were seeded in 24-well plates with a cell density of 10000 cells/cm^2 in triplicates for 7 days using some of the cell culture media detailed in Table 9:

- Two α-MEM supplemented with FBS from different suppliers (BM1 and BM2).
- Two serum-free media from different suppliers (CD1 and CD2).
- One media supplemented with human serum (HSM).

For all conditions, the media was fully changed every two or three days. Note that CD1, CD2 and HSM are all xeno-free media (no animal-derived components in their composition) and are specialised media for the expansion of human MSCs.

Table 9 – Expansion media composition and classification

Media	Composition	Classification
BM1	α-MEM (Lonza) 10% FBS (Labtech)	SC
BM2	α-MEM (Lonza) 10% FBS (Gibco)	SC
BM3	DMEM (Gibco) 10% FBS (Gibco)	SC
CD1	StemMACS MSC Expansion Media Kit XF, human (Miltenyi Biotec)	SF, XF
CD2	Mesenchymal Stem Cell Growth Medium DXF (PromoCell)	SF, XF, CD*
HSM	Human Mesenchymal-XF Expansion Medium (Merck)	SC, XF

SC – Serum Containing; SF – Serum-free; XF – Xeno-free; CD – Chemically Defined.
* While suppliers claim the media as “defined”, it might not be chemically defined.

Cell expansion was monitored using light microscopy and cell metabolic activity was measured on day 7 using resazurin reduction assay, as stated in 4.2.5.

5.3.2. Expansion of immortalised human MSCs in different cell culture media and media change protocols

Human MSCs immortalised with the human telomerase reverse transcriptase gene (hTERT-MSCs Y201) [83], provided by the University of York and stored at passage either passage 76 or 77, were initially expanded in T75 flasks using BM3 (see Table 9) as detailed in 4.2.2 and until passage 78 was reached. The cells were then seeded in two 48-well plates, divided as such:

- **EM –** cells in media without osteogenic supplementation (expansion media).
- **OM –** cells in media with osteogenic supplementation (osteogenic media, see section 4.2.1.4).

The Y201 cells at passage 78 were seeded in 48-well plates with a cell density of 4000 cells/cm^2 for 21 days using some of the cell culture media detailed in Table 9: DMEM supplemented with FBS (BM3), CD1 and HSM. Regardless of plate and media used, cells were seeded with EM in triplicates and following the media changes conditions detailed in Table 10. In the OM plate, for conditions F1 and H1 the osteogenic supplementation was initially added to the media 2 days after seeding, and for condition H3, the first media change was done with EM, adding the osteogenic supplementation afterwards. For condition F3, the seeding EM was fully replaced with OM during the first media change.

Table 10 – Media change conditions

Condition	Definition
F1	1 full media change/week
F3	3 full media changes/week
H1	1 half media change/week
H3	3 half media changes/week

Cell expansion was monitored by measuring cell metabolic activity on days 7, 14 and 21 using resazurin reduction assay, as stated in 4.2.5.

5.3.3. Optimising the osteogenic differentiation of immortalised human MSCs in serum-free media and different supplementation profiles

Y201 cells were expanded to passage 78 as detailed in 5.3.2, albeit with CD1. The cells were then seeded in three different 48-well plates, each one representing one time point: day 7, day 14 and day 21. For all time points, cells were seeded using only CD1 and following conditions F1 and H3 of Table 10. For each condition, cells were also cultured following three different supplementation profiles:

- **EM** – No osteogenic supplementation.
- **OM1 –** Ascorbic acid 2-phosphate (AA2P) added during the first media change, and beta glucose phosphate (βGP) and dexamethasone (DEX) during the second media change (days 2 and 5 for condition F1, respectively).
- **OM2 –** All osteogenic supplements added during the first media change (day 2 for condition F1).

For each plate, expansion was monitored using light microscopy, and at its corresponding time point ALP activity was measured using p-Nitrophenyl phosphate colorimetry as stated in 4.2.6.3.

5.4. Results

5.4.1. Serum-free media can be a good substitute to serum-containing media for the expansion of human MSCs from a primary source

Figure 22 shows the metabolic activity of human MSCs of a primary source on passage 4 after 7 days of culture in different media and substrates, with full media changes every 2 or 3 days. As it is possible to see, while HSM is the overall best media for these cells, CD1 was also able to perform significantly better than all other media, including the other serum-free option. On the other hand, not only does CD2 generally perform similarly to BM1 and BM2 in most instances, but it also performed significantly worse than BM2 in the gelatine-coated substrates. CD2 was also the only media that did not show an increase in metabolic activity when cells were cultured in coated well plates. For all other media, coating the substrate with either gelatine or fibronectin had a positive impact on metabolic activity, with both coatings performing similarly to one another.

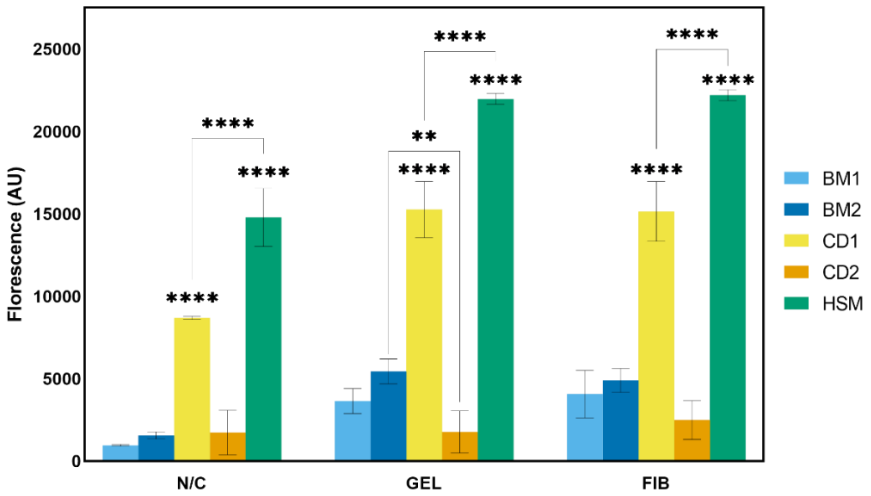

Figure 22 – Metabolic activity of human MSCs from primary sources at day 7, cultured in different media and substrates (mean + standard deviation, n = 3; ** p < 0.01; **** p < 0.0001).

Figure 23 shows the morphology of the human MSCs at day 7 and how they expanded when cultured in different media and substrates. Bearing in mind that MSCs are a heterogeneous cell population [78, 101], all cells cultured in all conditions seem to possess the general morphologies typically associated with the cell type [101]. These results seem to indicate that, despite the differences in cell density detected both by microscopy and by measuring their metabolic activity, all cells present healthy phenotypes. As expected, cell density appears larger when cultured in CD1 and HSM, being in line with the results presented in Figure 22. Furthermore, cells in these conditions seem to be distributed in spiral-like patterns, which are typical for healthy MSCs at high confluence levels [103, 104]. Alongside metabolic activity, these results confirm that both CD1 and HSM are the best-performing media for the expansion of human MSCs in this study. Furthermore, while it is not noticeable in cells cultured in CD1 and HSM, due to the high confluence levels regardless of substrate, it is possible to see that cell density is higher for cells cultured in BM1 and BM2 and coated substrates compared to their respective uncoated counterparts. As expected from the metabolic activity results, CD2 shows a cell density closer to that of BM1 and BM2 and similar between all three substrates.

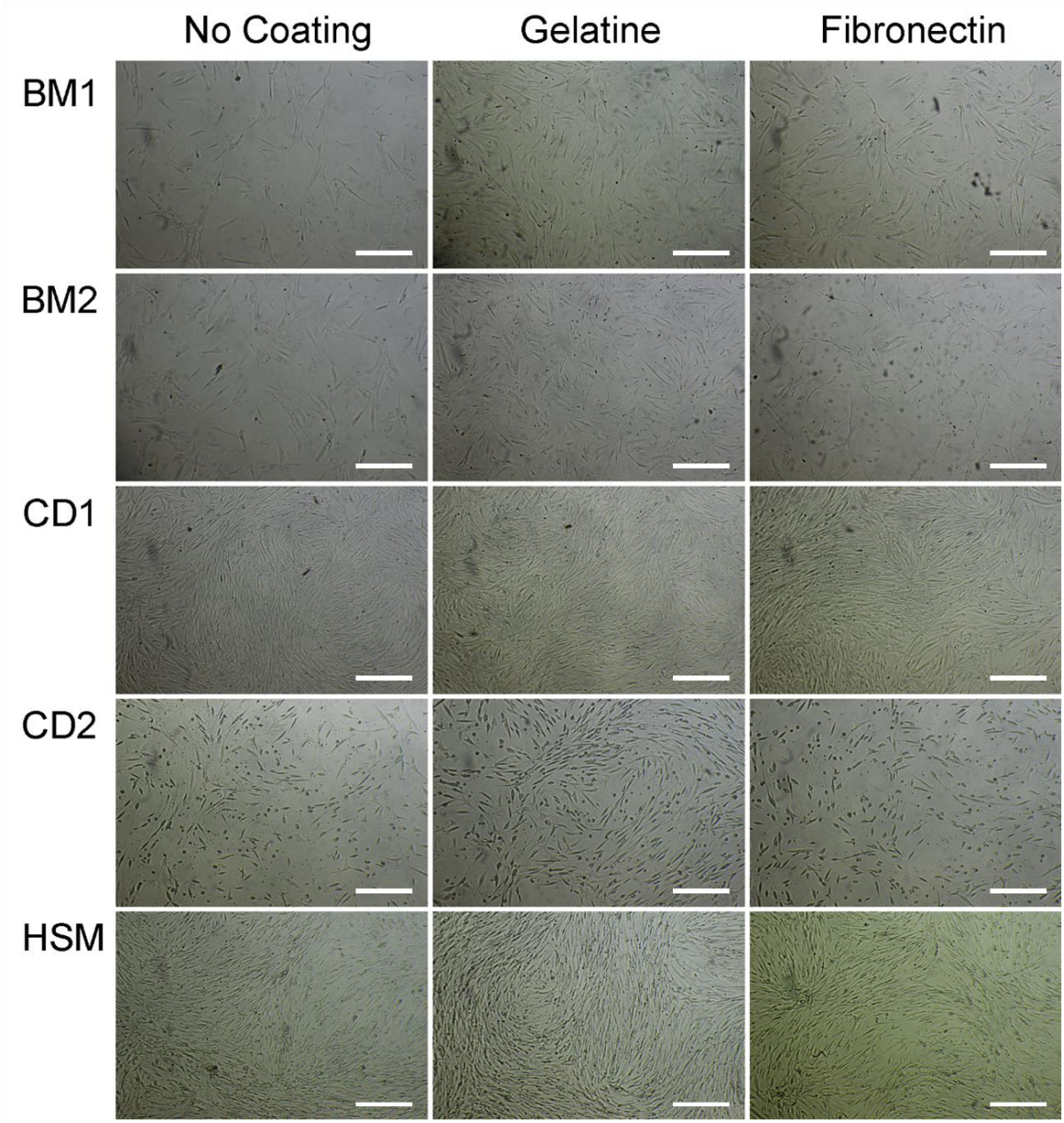

Figure 23 – Morphology and expansion of human MSCs from primary source at passage 4 in different media and substrates (scale bar = 500 µm).

5.4.2. Serum-free cell culture conditions are optimal for Y201 cells

Figure 24 details the metabolic activity at each time point of Y201 cells cultured in different media, media change conditions and without osteogenic supplementation. As it is possible to see, the serum-free media CD1 shows itself as the best media for Y201 expansion, significantly outperforming all other media at day 7 and keeping, for the most part, the same levels of metabolic activity up to 21 days of culture. BM3 can only reach similar levels of metabolic activity on day 14, and HSM surprisingly shows itself as the worst-performing media, only potentially reaching similar levels on day 21.

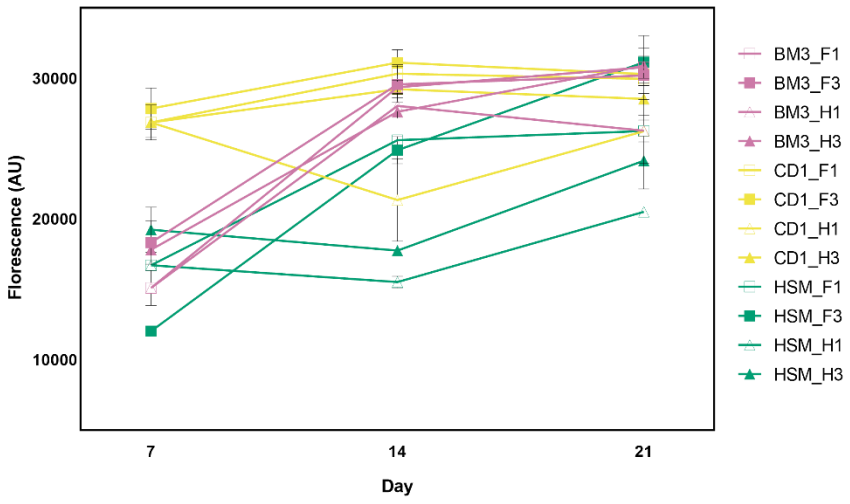

Figure 24 – Evolution of metabolic activity of Y201 cells in different cell culture expansion media and media change conditions (mean + standard deviation, n = 3).

The media change condition can influence metabolic activity, however. For example, for condition CD1_H1 (1 half media change/week), metabolic activity drops considerably from day 7 to day 14, and a similar effect can be observed in BM3_H1,

albeit from day 14 to day 21. For HSM, both conditions with half media changes perform considerably worse when compared to full media changes. These results could potentially indicate an inadequate cell culture environment when using said supplementation profiles, be it due to a lack of nutrients and/or an inadequate environmental pH. Nevertheless, the supplementation profile F1 (1 full media change/week) was always one of the best performing conditions for all media. As this condition uses less media than F3 and H3 (3 full and half media changes/week, respectively), the results indicate that it might be possible to keep cells viable for up to 21 days while minimising media usage.

The results obtained with osteogenic media (Figure 25) are similar to those obtained with expansion media, favouring CD1 and presenting HSM as possibly the least indicated option for Y201 cells. Interestingly, cells in BM3 do not seem to reach the same maximum metabolic activity values in OM compared to EM. This could be an indicator that the cells in OM are indeed differentiating: since proliferation slows down while cells are differentiating, the increase in metabolic activity tends to be slower when culturing cells in differentiation media [105]. Also interestingly, cells cultured in osteogenic CD1_F1 and CD1_F3 had very similar metabolic activity, which could indicate that, during differentiation, there is no difference between changing media once or three times a week, again pointing towards a possibility to use less media during each experiment.

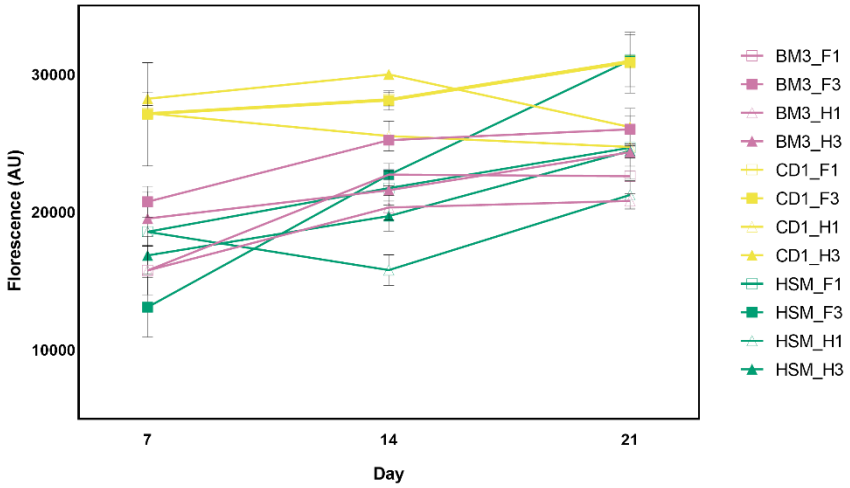

Figure 25 – Evolution of metabolic activity of Y201 cells in different cell culture osteogenic media and media change conditions (mean + standard deviation, n = 3).

5.4.3. The osteogenic differentiation of Y201 cells can be detected after 14 days of culture in osteogenic media

Figure 26 details how Y201 cells look after culturing for 21 days in CD1 serum-free media, different osteogenic supplementation profiles, and media change conditions. Two things are noticeable in the figure. First, the dark particles in Figure 26 b) and c), representing OM1_F1 and OM2_F1 respectively (see Table 10 and section 5.3.3), are a sign of mineral deposition, indicating that the Y201 cells in these conditions are differentiating into their bone-like lineage. The same signs of mineral deposition were not present at previous time points. Second, cell density is much lower in Figure 26 d), e) and f), which represent all conditions with three half media changes per week. These results were due to the cells becoming overconfluent and detaching from the wells. For each condition it was possible to obtain one well without cellular detachment, and these also showed signs of mineralisation when cultured with osteogenic media. Nevertheless, these results suggest that one full media change is enough to guarantee mineralisation in Y201 cells and,

consequently, their osteogenic differentiation, while also minimising the risk of cellular detachment.

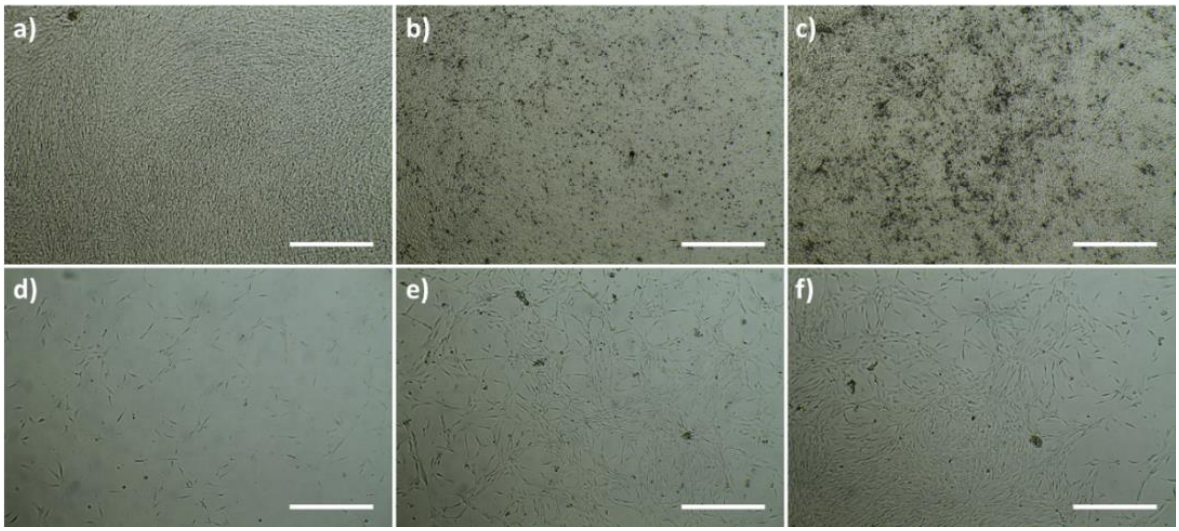

Figure 26 – Morphology, distribution, and mineralisation of Y201 cells cultured in CD1, and different media change conditions and supplementation profiles: a) EM_F1; b) OM1_F1; c) OM2_F1; d) EM_H3; e) OM1_H3; f) OM2_H3 (scale bar = 500 µm).

Overall, it is possible to see a general increase in average ALP activity between time points (Figure 27). This is expected both due to cell expansion and, most importantly, increasing differentiation of the cells with time. Moreover, it is possible to see that, for the conditions where media was changed once every week (conditions F1), the average ALP activity starting at day 14 is higher in Y201 cultured with osteogenic media compared to those cultured in expansion media. As an increase in ALP activity is an early indicator of osteogenic differentiation [106], these results indicate that, although mineralisation is only detectable after 21 days of culture, it is possible to detect the osteogenic differentiation of cells in just 14 days. Moreover, both supplementation profiles, OM1 and OM2 are shown to perform similarly at this time point.

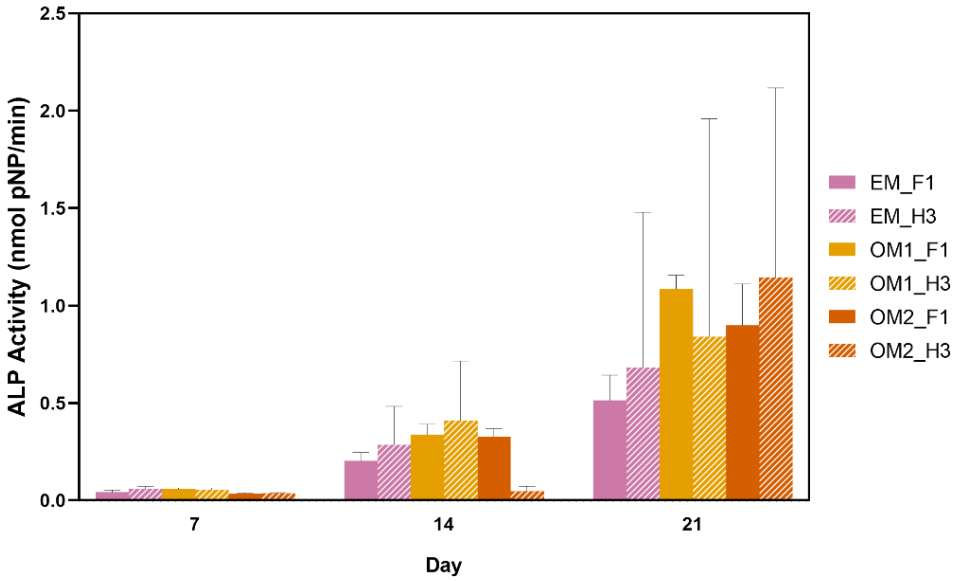

Figure 27 – ALP activity of Y201 cells at different time points and culture conditions (mean + standard deviation, n = 3).

For conditions with 3 half media changes per week (H3), either the ALP measured was surprisingly low (OM2_H3 at day 14) or its variability was too high for any significant change to be detectable. These results could also derive from the cell detachment problems previously detected: the lower the number of cells that are present in one well, the lower the concentration of ALP will be in their respective lysate, which consequently lowers the measured ALP activity. Regardless, these results, like those obtained through microscopy, point towards 1 full media change every week being the preferred method to avoid cell detachment during the experimental period.

5.5. Discussion

This chapter aims to develop a protocol to study the osteogenic differentiation of immortalised human MSCs in serum-free conditions, to serve as a basis for the *in vitro* biological assays conducted in Chapters VI and VIII. This protocol would allow to reduce possible issues with variability that could derive both from using standard cell culture media supplemented with FBS [86, 87, 102] and from MSCs derived from primary sources [78, 81, 83, 87].

Human MSCs from a primary source were still initially used for two reasons. First, due to the immortalised cell line used for the remaining of the chapter not being available at the start of the project. Second, because it would still be important for future work to identify serum-free media that could work both for immortalised and primary MSCs, to have their culture conditions as close as possible. As a reminder, despite possible variability in results that primary cells from different sources could introduce, *in vitro* testing with these sorts of cells is still an important step as they are more representative of the *in vivo* environment. The two serum-free media tested at this stage, CD1 and CD2 (see Table 9 for supplier) were chosen mainly due to being both specially formulated for the culture of MSCs and for being similarly priced to HSM. In turn, HSM is a specialised media for MSC expansion supplemented with human serum, which was shown to perform significantly better than standard media supplemented with FBS [107]. BM1 and BM2 were two α-MEM-based media supplemented with FBS from different suppliers, as to show the differences that FBS from different sources could make in cell culture. Finally, while MSCs by definition are a plastic-adhesive cell population [76, 78], since the supplier instructions for CD2 specifically mention the need for fibronectin coating when using said media [108], it was decided to study the effect that coating the well-plates with fibronectin could have in all media, and whether its effects could be similar to a gelatine coating, which is more easily available than fibronectin.

As seen in Figure 22, while HSM was still the best-performing media in all three substrates, CD1 was also able to significantly improve the expansion of human MSCs from a primary source, with the metabolic activity being up to 8 times higher when compared to BM1 and BM2, which represent standard cell culture media. Moreover, as seen in Figure 23 and just like in HSM, cells become confluent in just one week of culture in CD1, presenting the morphologies and patterning associated with healthy MSCs [103, 104]. On the other hand, CD2 either performed similarly to the FBS-containing media, or in one case, significantly worse than BM2. These results were surprising because CD2 was supposed to be a specialised media for MSC growth. These results could have been justified had it only occurred in uncoated well-plates, as the supplier's instruction did mention that the media requires a fibronectin coating to work effectively [108]. However, the performance of cells in CD2 was not only similar regardless of substrate, it was the only media which did not see an increase in metabolic activity in coated substrates. As for both media containing FBS, metabolic activity is slightly higher in BM2 in all substrates, compared to BM1. While the difference is not as significant as others have reported [102], it still shows the effect different FBS can have on cellular response. Overall, these results do show that serum-free expansion of MSCs from a primary source is valid and can significantly outperform standard culture conditions, even if it might be necessary to choose the correct media for the cells in use (CD1 in this case).

Because the performance of CD2 was of the same level as BM1 and BM2, it was discarded as a media when studying the expansion of Y201 cells. BM1 and BM2 were also replaced by BM3, as DMEM is the standard media recommended for that cell line [83]. As BM2 was the best performing of the FBS-containing media, BM3 was supplemented with the same FBS as BM2. Finally, it was decided to only use non-coated plates, as while the gelatine and fibronectin coatings did have a beneficial effect on MSC expansion, it was also found not necessary for the cells to attach and proliferate.

What is immediately evident when analysing Figure 24 is that, unlike the previous cells, CD1 is not just a viable option for Y201 expansion, but actually the best-performing media, with metabolic activity reaching its highest levels in just 7 days, maintaining those levels in all but one media change condition (1 half media changes/week, or H1). Interestingly, unlike the cells from primary sources, HSM seems to be the worst-performing media, only reaching the same levels of metabolic activity as CD1 after 21 days. These results show why choosing the best media for a particular cell line is important: different media can perform differently in cells from different sources. Similar results were obtained with osteogenic media, meaning that it is possible to keep cells in CD1 for up to 21 days of culture in both expansion and osteogenic media. This is important, as it allows to keep both negative (EM) and positive (OM) osteogenic controls for as long as future experiments might need.

The obtained results also point towards the difference between cells that have been immortalised compared to those that have not: immortalised cells, like cancer cells, proliferate at much faster rates than normal healthy cells. In fact, many continuous cell lines derive from cells collected from cancer patients. It is also important to notice the cell passage of both cell sources: while primary MSCs generally do not reach passages longer than 10, the Y201 cells used during this work were at passages 76 to 78. Y201 cells are expected to keep their properties up to at least passage 80 [83].

Having found CD1 as a suitable media for the expansion of both cells from a primary source and Y201 cells, the osteogenic differentiation of the immortalised cell line was studied only in this media. Media change conditions H1 and F3 were also dropped due to H1 resulting in a decrease in metabolic activity after 14 days, and F3 resulted in similar metabolic activity as H3 and F1, while also using, respectively, twice and three times as much media. Two different supplementation profiles were also tested to see if introducing the supplements at different times can enhance MSC differentiation, as others have shown [107]. The first indicator that F1 might be the best media change condition regardless of supplementation profile was that, contrary

to H3, F1 was shown to both induce cell mineralisation and avoid cell detachment. The issue with cell detachment also explains the high variability in ALP activity present in most H3 samples after 14 days: the levels measured are not just dependent on Y201's osteogenic differentiation, but on the number of cells that have been lysed as well. The cells in H3 might be more differentiated than those in F1, but cell detachment makes the assessment more difficult. There are ways to take into account different growth rates, such as normalising the measured ALP activity to the DNA quantity present in the same lysate, a measure that will be taken in Chapters VI and VIII.

Finally, although the ALP levels are shown to be at their average maximum at day 21, the same time when mineralisation starts being detected, it is possible to observe a difference between samples in EM or OM as soon as 14 days, indicating that the osteogenic potential of any material tested in Chapters VI and VIII can be measured in just 14 days during *in vitro* studies. Furthermore, no difference was detected between supplementation profiles. While this might contradict previous research [107], it should be noticed that said studies were conducted on MSCs from a primary source, not on immortalised MSCs such as the Y201 cell line. For practical reasons, it was decided to use OM2 as supplementation in any future experiments, as all supplements are added at the same time in these conditions.

5.6. Summary

In this work, a serum-free protocol was developed for the expansion and osteogenic differentiation of human MSCs from both primary or immortalised sources. It was found that the serum and xeno-free media *StemMACS MSC Expansion Media Kit XF, human*, from Miltenyi Biotec, performed better than standard conditions and comparable to specialised MSC media containing human serum which was previously found to enhance the culture of primary MSCs, with or without any protein-based coating for cell attachment. It was also found that hTERT-

MSCs Y201 can be successfully expanded and differentiated towards their osteogenic lineage while performing one single full media change every week and that introducing the different osteogenic supplements at different times does not alter ALP activity of Y201 cells and, as such, their osteogenic differentiation in a significant manner. While cells can be cultured in both EM and OM for up to 21 days, it is possible to detect differences in ALP activity between both kinds of media in just 14 days of cell culture. Furthermore, the supplementation profiles studied were not shown to affect the osteogenic differentiation of Y201 cells. The results obtained from this chapter were then used to inform how the *in vitro* biological assays from Chapters VI and VIII should be conducted.

VI. Synthesis and *in vitro* biologic performance of Mg and Sr substituted hydroxyapatite by wet chemical precipitation

6.1. Introduction

As the basis of bone mineral, hydroxyapatite (HAP) has been extensively researched as a material for bone regeneration [44-46]. While its mechanical properties are not adequate for it to be used as the main structure of an orthopaedic implant, it has seen great success when applied as bone fillings or as osteoinductive coatings [44, 45]. When in contact with HAP, mesenchymal stem cells (MSCs) can differentiate into the osteogenic lineage and, as such, stimulate the growth or regeneration of bone tissue [109, 110].

Stochiometric HAP is represented by the formula $Ca_{10}(PO_4)_6(OH)_2$. However, biological hydroxyapatite is in general not stochiometric, presenting different ionic species that can substitute any of the original ions present in the HAP structure. These substitute ions can have several beneficial effects on bone biology, potentially affecting cell adhesion, stimulation and inhibition of specific cells, and the release of any factors that influence all aspects of bone biology [46-48]. By knowing the effects different ionic substitutions can have on bone repair, it is possible to synthesise hydroxyapatite tailored for different applications and needs.

Two substitutions of interest are magnesium and strontium, as Mg has been shown to stimulate the proliferation and differentiation of osteoblasts, the cells responsible for bone mineralisation, while Sr is involved in inhibiting osteoclasts, the cells responsible for bone resorption [47, 48]. Moreover, Mg is shown to affect mineral metabolism and Sr in the secretion of angiogenic factors that increase vascularisation [47, 48]. Mg-substituted HAP is already commercially available for medical applications [49], showing better biological performance than stochiometric

HAP [111], and Sr-based medication has been successfully used for the treatment of osteoporosis [112], although new evidence raises concerns about its effects on patients with cardiovascular issues [113, 114]. As such, it is speculated that a HAP formulation that includes both ions in its structure will have increased biological performance when compared to stochiometric HAP and HAP which includes only one of these particular ions in its structure.

Due to the benefits that substituted hydroxyapatite (sHAP) presents compared to its stochiometric counterpart, and considering the biological effects both ions are shown to have, this chapter will focus on the development of sHAP substituted with both Mg and Sr.

6.2. Aims and objectives

The aim of this chapter was to assess the optimal conditions to synthesise Mg and Sr sHAP with optimal *in vitro* biological performance using wet chemical precipitation. These results were used to obtain the sHAP required for the final coatings developed in Chapter VIII. To achieve this aim, the following objectives were addressed:

I. Pre-screen of different sHAP formulations with different substitution degrees, and of different sHAP synthesis and washing conditions.
II. Assess using DoE what conditions allow sHAP to be synthesised with the theoretical substitution levels, high crystallinity, and good biological performance.

6.3. Materials and methods

The following Materials and Methods are specific to this chapter. For general details please check Chapter IV.

6.3.1. Pre-screening the synthesis of Mg and Sr substituted hydroxyapatite

Following the protocol present in 4.2.7, six different HAP samples were synthesised, following the specifications from Table 11. The basic solution was stirred using a magnetic stirrer bar, and no ammonia solution was used while synthesising these samples. In theory, the synthesised sHAP should have the physicochemical properties described in Table 12.

Table 11 – sHAP pre-screening formulations

Formulation	Basic solution						Acid solution	
	Ca - $Ca(OH)_2$		Mg - $Mg(NO_3)_2 \cdot 6H_2O$		Sr - $Sr(NO_3)_2$		P - H_3PO_4	
	mol%	weight (g)	mol%	weight (g)	mol%	weight (g)	mol%	weight (g)
C0	100	40.91	0	0	0	0	100	37.03
C4	90	36.81	5	6.92	5	5.71	100	37.03
C5	85	34.76	5	6.92	10	11.43	100	37.03
C6	85	34.76	10	13.85	5	5.71	100	37.03
C7	80	32.72	10	13.85	10	11.43	100	37.03
C8	85	34.76	7.5	10.38	7.5	8.56	100	37.03

Table 12 – Theoretical physicochemical properties of sHAP for each formulation

Formulation	Ca/p	$\frac{Ca+Mg+Sr}{P}$	Mg %	Sr %
C0	1.66	1.66	0	0
C4	1.49	1.66	5	5
C5	1.41	1.66	5	10
C6	1.41	1.66	10	5
C7	1.33	1.66	10	10
C8	1.41	1.66	7.5	7.5

The samples were washed by centrifugation as stated in 4.2.8. The final samples were analysed by FTIR, as stated in section 4.2.10.

6.3.2. Synthesis of sHAP while controlling reaction pH

sHAP was synthesised following formulation C6 from Table 11. The reaction pH was measured every 5 minutes using pH indicator paper (range 1 – 14) during the synthesis. Whenever the pH dropped below 10, the addition of the acidic solution was stopped, and the pH was adjusted to a value within the 10 – 12 range by adding 28% ammonia solution. After adding all the acidic solution, the pH continued to be monitored every 5 minutes for 1 hour, with the pH adjusted as previously described whenever it dropped below 10. The synthesised material was washed and analysed as described in section 6.3.1.

6.3.3. Comparison of sHAP washing methods

sHAP was synthesised following formulation C6 from Table 13. Compared to Table 11, the updated formulations more closely follow those used by the project's industrial partner. However, the theoretical physicochemical properties remain the same as those from Table 12. 50 ml of 28% ammonia solution was used to create the basic solution, meaning that for a total volume of 500 ml, 450 ml of ultrapure water was used for this solution.

Table 13 – Final sHAP formulations

Formulation	Basic solution						Acid solution	
	Ca - $Ca(OH)_2$		Mg - $MgCl_2 \cdot 6H_2O$		Sr - $Sr(NO_3)_2$		P - H_3PO_4	
	mol%	weight (g)	mol%	weight (g)	mol%	weight (g)	mol%	weight (g)
C4	90	89.97	5	13.03	5	13.96	100	90.51
C5	85	84.96	5	13.03	10	27.93	100	90.51
C6	85	84.96	10	26.06	5	13.96	100	90.51
C7	80	79.97	10	26.06	10	27.93	100	90.51
C8	85	84.96	7.5	19.54	7.5	20.94	100	90.51

The synthesis was kept under stirring using an overhead mechanical stirrer. After the overnight incubation period, the synthesised material was divided into four samples, each one washed using one of the methods from Table 14 (see 4.2.8 and 4.2.9). All filters were obtained from Whatman®.

Table 14 – sHAP washing methods

Method	Description
1	6x Centrifugation (6000 rpm, 10 min)
2	3x Vacuum filtration (paper filter pore size 25 µm)
3	3x Vacuum filtration (paper filter pore size 6 µm)
4	3x Vacuum filtration (paper filter pore size 2.5 µm)

The pH was measured before and after each washing step using paper indicator (range 1 – 14), and the dried samples were analysed by FTIR, as stated in 4.2.10.

6.3.4. Synthesis of Mg and Sr sHAP – design of experience approach

The synthesis of Mg and Sr sHAP with different substitution levels was studied using a full factorial design. Table 15 describes the factors studied, while Table 16 summarises the design used.

Table 15 – Synthesis of Mg and Sr sHAP: factor description

Factor	Description	–	0	+
A	Mg substitution degree (%)	5	7.5	10
B	Sr substitution degree (%)	5	7.5	10
C	Ammonia solution 28% volume (ml)	15	32.5	50

Table 16 – Synthesis of Mg and Sr sHAP: design summary

Standard Order	Run Order	A	B	C	Formulation
1	7	–	–	–	C4
2	4	+	–	–	C6
3	8	–	+	–	C5
4	10	+	+	–	C7
5	1	–	–	+	C4
6	5	+	–	+	C5
7	3	–	+	+	C6
8	2	+	+	+	C7
9	9	0	0	0	C8
10	6	0	0	0	C8
11	11	0	0	0	C8

For each run, sHAP was synthesised following the run order and conditions described in Table 16. The materials and quantities described in Table 13 were used during the synthesis. The obtained samples were washed following method 4 from Table 14. Before and after each washing step, the pH of each sample was measured

using indicator paper (range 1 – 14). The final samples were analysed by ICP-OES, and XRD analysis on all samples was performed by an external contractor (Specialchimica s.a.s – Merada, Italy). Finally, the powders were tested *in vitro* as stated in section 4.2.11, measuring metabolic activity at day 7 and day 14, and DNA-adjusted ALP activity at day 14 (4.2.5 and 4.2.6.3, respectively). Cells cultured in expansion media, in osteogenic media, and when exposed to Mg-enriched HAP, provided by the industrial partner, were used as control groups for comparison.

The DoE was analysed using the software *Minitab 20.0*. As tentative design responses, the following results were used:

- Ca/P ratio, (Ca+Mg+Sr)/P ratio, Mg substitution % and Sr substitution %, obtained by ICP-OES.
- HAP phase % and HAP crystallinity, obtained by XRD.
- Cell metabolic activity and DNA-adjusted ALP activity, obtained through *in vitro* biological testing.

6.4. Results

6.4.1. pH can affect the synthesis of substituted hydroxyapatite

Figure 28 shows the FTIR spectrum obtained when analysing HAP synthesised by following formulation C0 from Table 11 during the pre-screening experiments. This represents the spectrum of pure HAP and will serve as a reference when analysing all sHAP samples. Overall, it shows all the expected peaks for HAP [115].

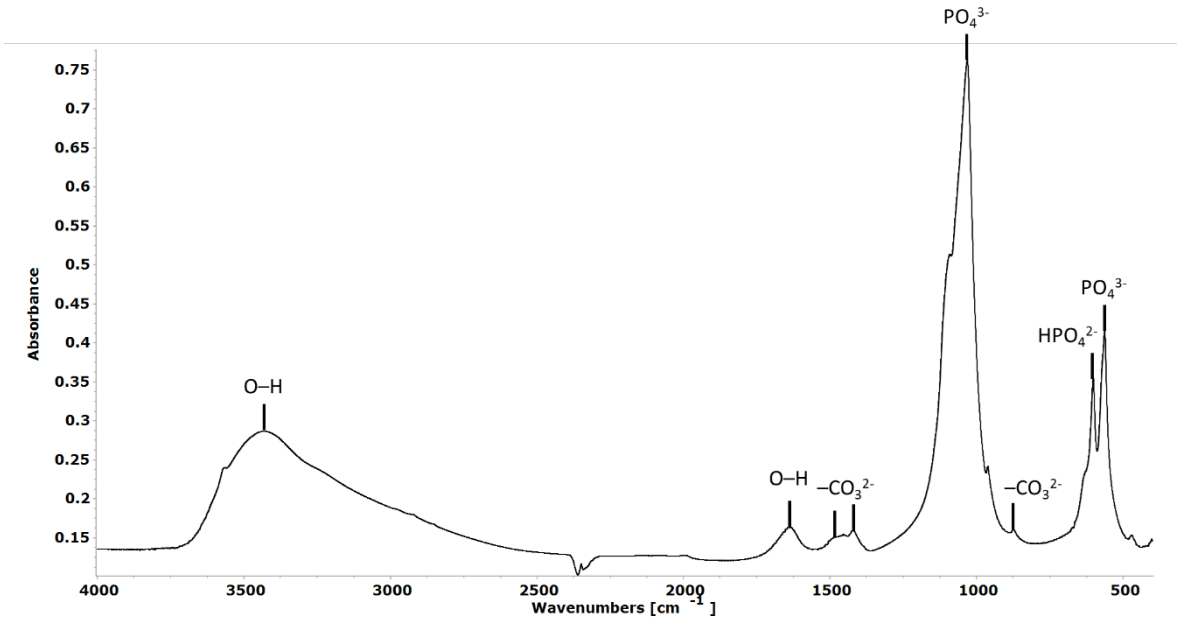

Figure 28 – FTIR spectrum of pure HAP C0, with relevant peaks identified.

Figure 29 compares the FTIR spectrum of pure HAP with the spectra obtained from sHAP samples following formulations C4 to C8 (see Table 12) from the same pre-screening experiments. As it is possible to observe, only formulation C4 shows a spectrum close to that of pure HAP, suggesting that only this formulation was successful in the synthesis of sHAP. In fact, instead of HAP, the spectra from all other samples are closer to that of brushite, a different calcium phosphate mineral with the formulation $CaHPO_4 \cdot 2H_2O$ [116].

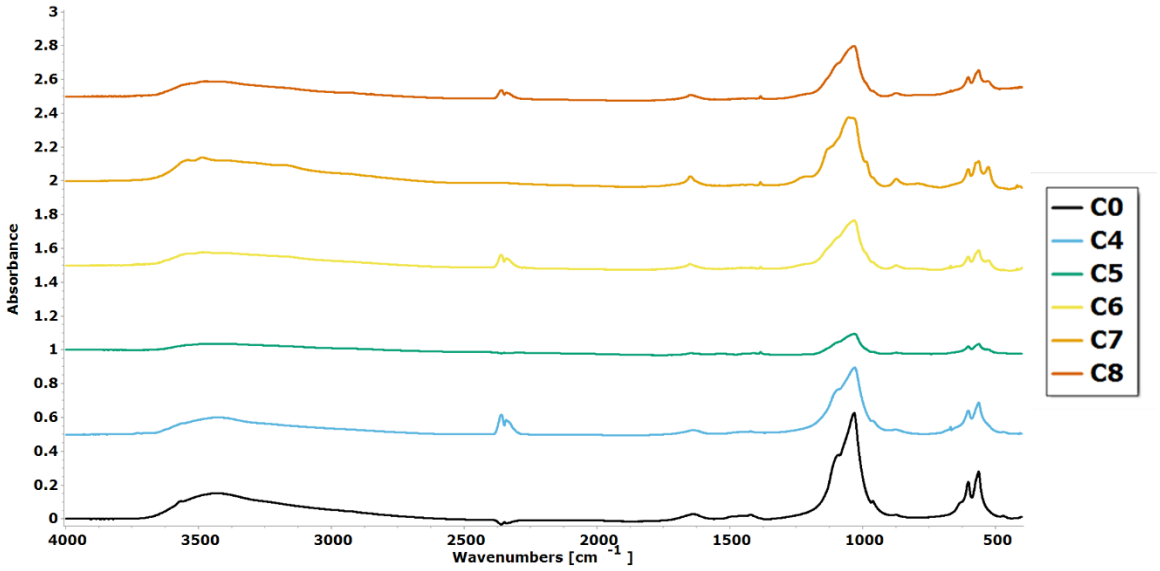

Figure 29 – FTIR spectrum of pre-screening sHAP samples.

It was suspected that the synthesis problems might have been due to a suboptimal pH during the reaction between reagents. Synthesis of HAP is shown to be optimal when the pH is at a 10-12 range [117, 118]. The experiments detailed in section 6.3.2 were conducted to test this theory. Table 17 shows that, while pH remained within the optimal range during the first 45 minutes of synthesis, it did drop to 6 at minute 50. 7 ml of ammonia solution 28% were added at the same time, allowing the pH to rise to 9.5. However, the pH dropped once again 15 minutes after the first addition of ammonia solution. This time, 11 ml of ammonia solution was added, and pH remained within the ideal range both until the synthesis ended and during the first hour of incubation. In total, 33 ml of 28% ammonia solution were added, 18 ml during the synthesis phase, and 15 ml during the incubation phase.

Table 17 – Evolution of pH during sHAP synthesis following formulation C6

Time (min)	Synthesis		Incubation	
	pH	Action	pH	Action
5	12		10	2 ml Ammonia 28% added
10	12		10	3 ml Ammonia 28% added
15	12		10	
20	12		10	
25	12		10	
30	12		10	5 ml Ammonia 28% added
35	12		11	
40	12		11	
45	10		10	
50	6	7 ml Ammonia 28% added	10	
55	9.5		10	
60	9.5		10	5 ml Ammonia 28% added
65	7	11 ml Ammonia 28% added	10	Left overnight under stirring
66	10 – 12	All acidic solution added	N/A	

Comparing the FTIR spectrum of the pH-controlled C6 sHAP to the one obtained without adding ammonia (Figure 30), these newer results are closer to those from pure HAP (see Figure 28), suggesting that when pH is kept within the optimal range, formulation C6 can be used to synthesise HAP instead of brushite as seen previously.

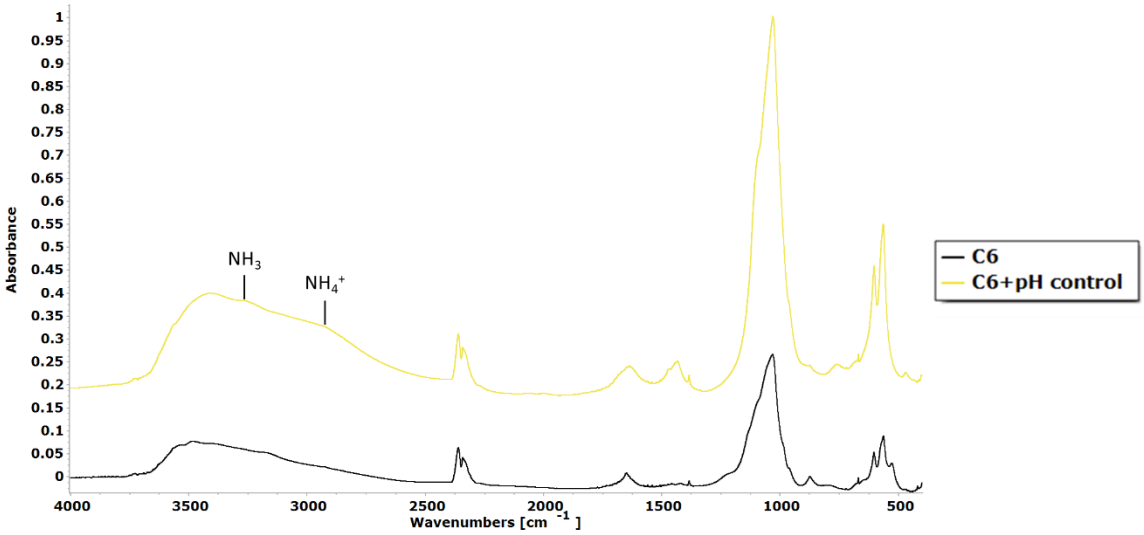

Figure 30 – Comparison between FTIR spectrum of pure HAP and sHAP C6 with or without pH control.

It is important to notice the subtle peaks at 3300 and 2900 cm^{-1} in the C6 + pH control FTIR spectrum from Figure 30, indicative of traces of ammonia still being present in the sample analysed [119]. The same curvatures are not present in the spectrum for C0, for example. This indicates that a more efficient washing method is required than what was previously used (three centrifugation steps).

6.4.2. Vacuum filtration can be used to eliminate ammonia residues from hydroxyapatite samples

As can be seen in Figure 31, by increasing the number of centrifugation steps to six it was possible to eliminate the subtle peaks attributed to ammonia. This indicates that the new washing step was successful. However, this led to a more time-consuming washing process.

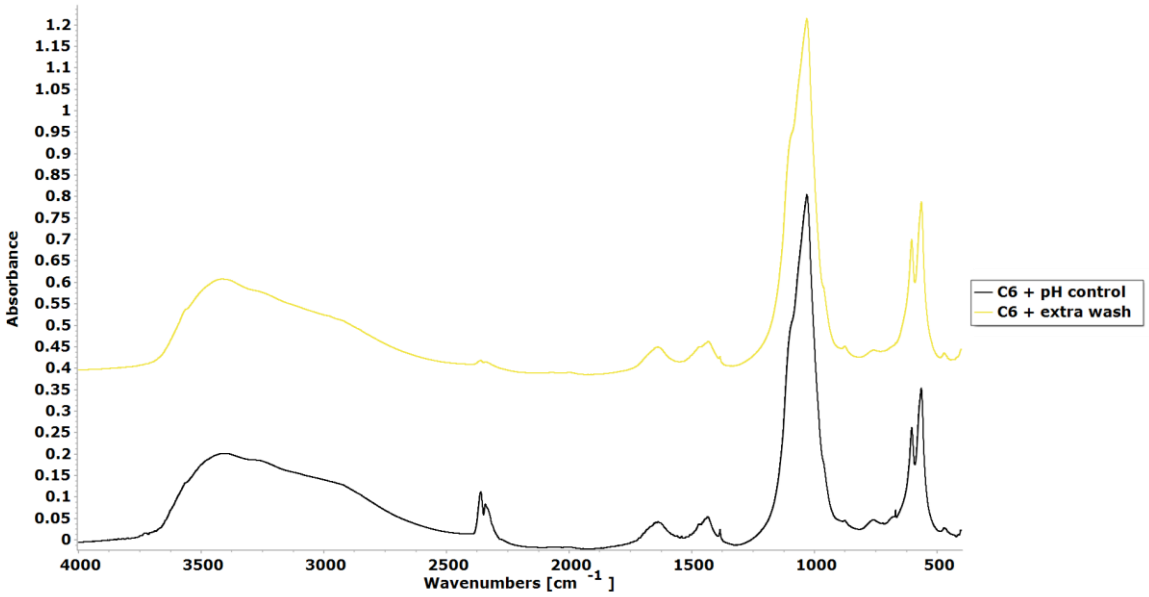

Figure 31 – Comparison between FTIR spectra of pH-controlled C6 before and after extra centrifugation washing steps.

The next step was to compare six centrifugation steps with vacuum filtration using filters with different pore sizes to see if the latter could be a more efficient alternative. As Figure 32 shows, all methods were able to successfully remove ammonia from the samples synthesised, as they lack the curvatures related to the presence of ammonia. Moreover, all methods based on vacuum filtration were able to remove any trace of ammonia in just three washing steps, instead of the six needed for the centrifugation method, confirming that vacuum filtration is indeed a less time-consuming method to effectively wash post-synthesis sHAP.

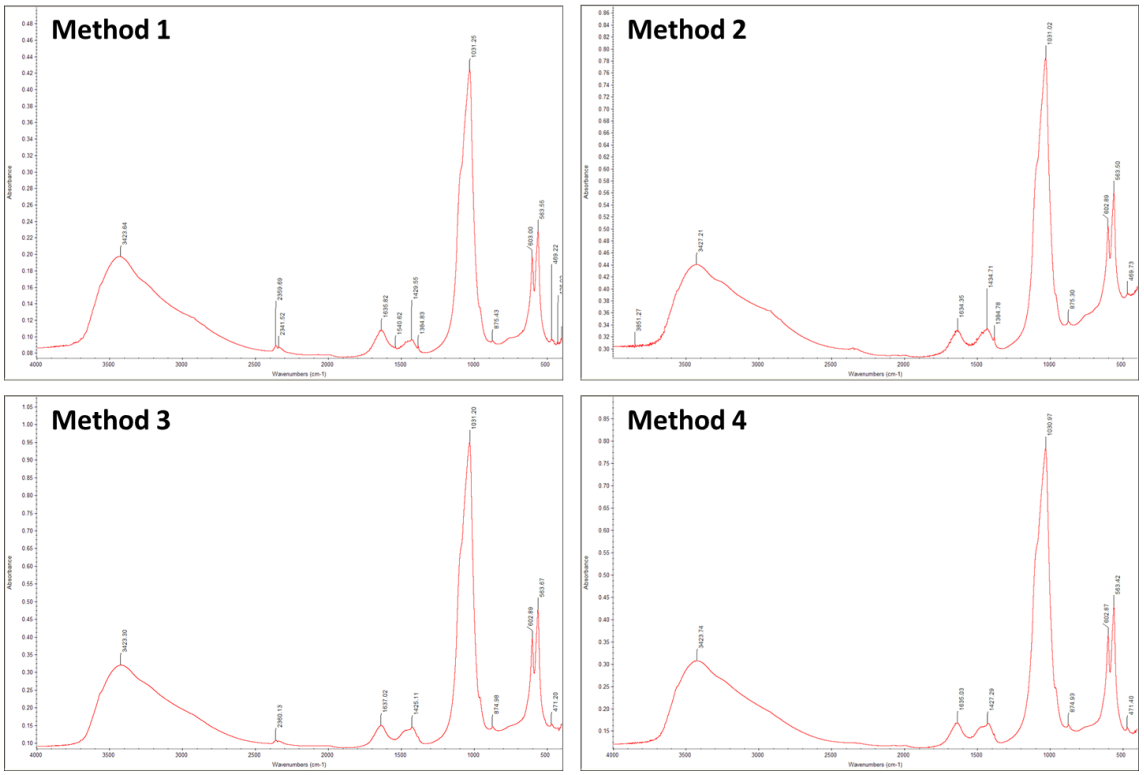

Figure 32 – FTIR spectrum of sHAP C6 synthesised with 50 ml of ammonia solution and washed using different methods (see Table 14).

There is one caveat with using vacuum filtration as the sHAP washing process, as the pore size of the paper filter used can influence the final sHAP yield. As shown in Figure 33, when using filter paper with pore size equal to 25 µm, the filtered liquid appears cloudy right from the start of the filtration process. This indicates that sHAP is being lost during the washing process due to the use of a paper filter with inadequate pore size. On the contrary, when using filter paper with a pore size as low as 6 µm the filtrate appears fully transparent even at the end of each washing step, indicating that there is no significant material loss when using these filters.

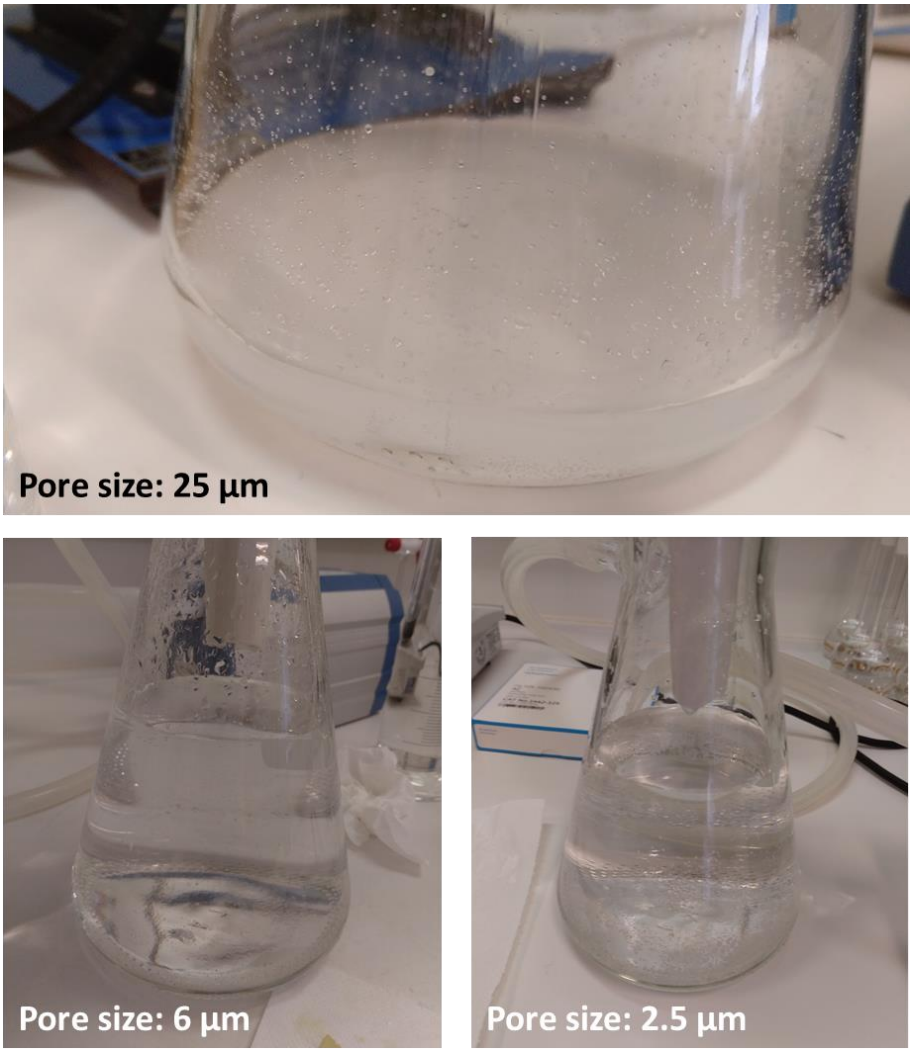

Figure 33 – Filtrate from first vacuum filtration using paper filters of different pore sizes.

6.4.3. Design of experiments can be used to model how the synthesis conditions affect the physicochemical properties of sHAP

Table 18 summarises the results obtained by measuring the pH before washing each of the sHAP samples synthesised following the conditions and order set by Table 15 an Table 16, as well as the results obtained from ICP-OES and XRD analysis.

Table 18 – Physicochemical characterisation of sHAP synthesised with Design of Experiments

Standard Order	Formulation	pH	Ca/P	$\frac{Ca+Mg+Sr}{P}$	Mg %	Sr %	HAP phase %	Crystallinity %
1	**C4**	6–7	1.46	1.60	4.09	4.81	97.4	18.19
2	**C6**	7	1.36	1.53	6.49	4.89	93.5	20.02
3	**C5**	7–8	1.34	1.51	2.49	8.79	97.0	18.48
4	**C7**	8	1.24	1.42	3.98	8.82	80.1	14.53
5	**C4**	10	1.48	1.66	5.97	4.99	100.0	20.13
6	**C6**	9–10	1.38	1.63	10.32	4.92	92.4	23.19
7	**C5**	10	1.39	1.63	5.59	9.63	100.0	19.22
8	**C7**	9	1.27	1.58	10.34	8.87	90.0	22.93
9	**C8**	9	1.38	1.61	7.35	6.82	91.4	22.56
10	**C8**	9	1.34	1.57	7.68	6.87	90.7	32.90
11	**C8**	9	1.34	1.57	7.77	6.90	95.6	32.40

At a first glance, Table 18 reveals a change in the physicochemical characteristics of sHAP synthesised following the same formulation but with different ammonia solution volumes and, consequently, pH values. Overall, when pH is higher than 9, the physicochemical properties of sHAP follow their theoretical values closer than sHAP synthesised at lower pH (see Table 12).

Each set of results was then evaluated using replicate plots to determine if they can be used to create linear models following DoE. The results can be seen in Figure 34. For all sets, the main runs can be easily divided into two halves, passing the first criteria for DoE modelling. However, for crystallinity %, the variability within the centre points is of the same magnitude as the variability within the main runs, indicating that this response cannot be modelled by the conditions set by the DoE in use (see Table 15 and Table 16). Moreover, while the centre points for Ca/P, (Ca+Mg+Sr)/P and Sr% are equidistant from the two halves of main runs, the same cannot be said for Mg% and HAP phase %. This indicates that the latter results, while showing the possibility to be modelled, might need to be transformed to guarantee linearity.

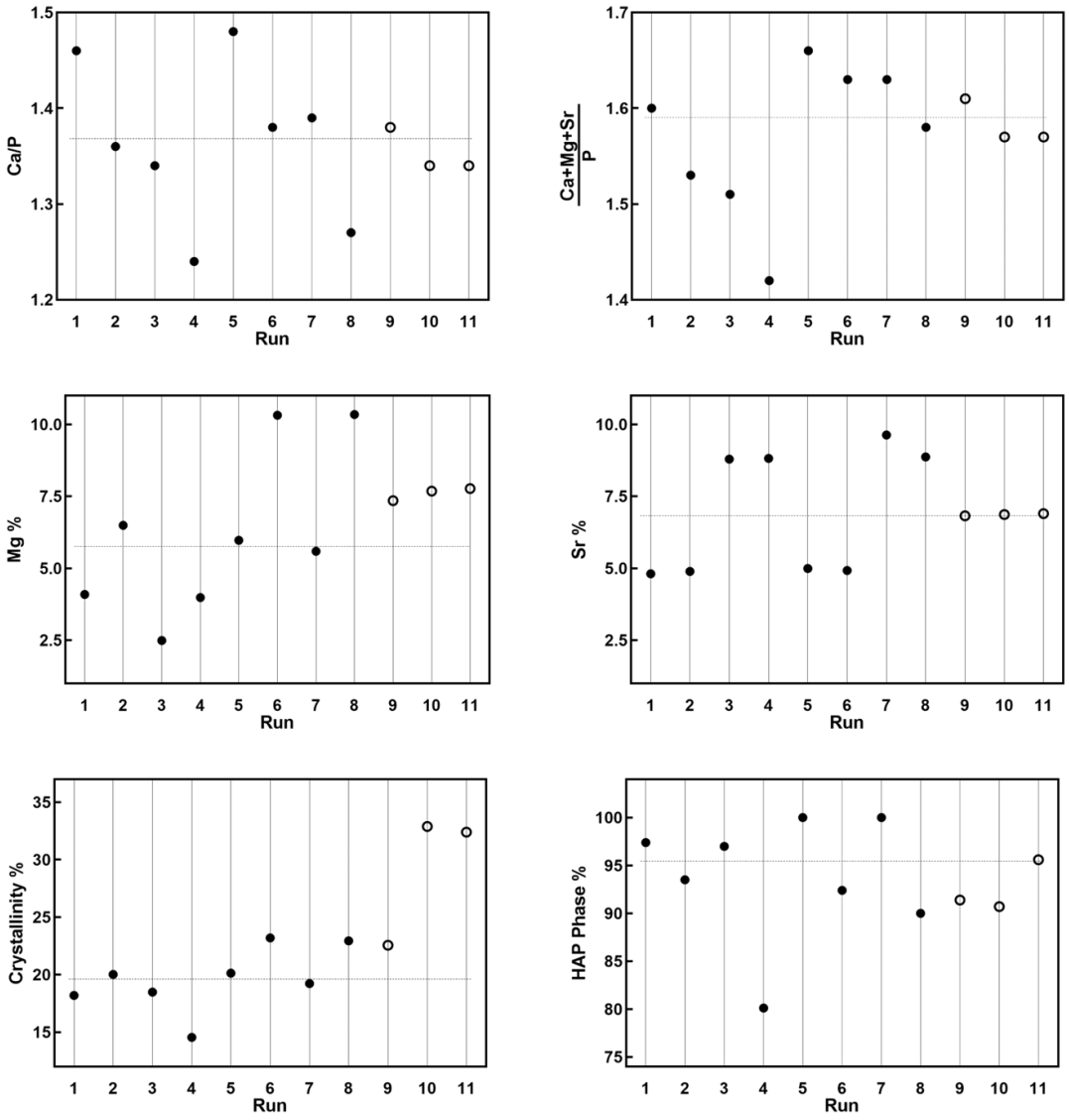

Figure 34 – Replicate plots for the physicochemical characterisation of the synthesised sHAP (black dots – main runs; white dots – centre points).

Minitab 20.0 was used to analyse each set of results, helping to formulate the optimised models represented by Equation 13 to Equation 17, including any possible data transformation necessary to ensure linearity. The summary of fit results for each model, as well as their respective Pareto charts of standardised effects, are found in Figure 35 to Figure 39.

Equation 13 – Optimised Model for Ca/P (factor description in Table 15)

$$\frac{Ca}{P} = 1.3618 - 0.0525A - 0.0550B + 0.0150C$$

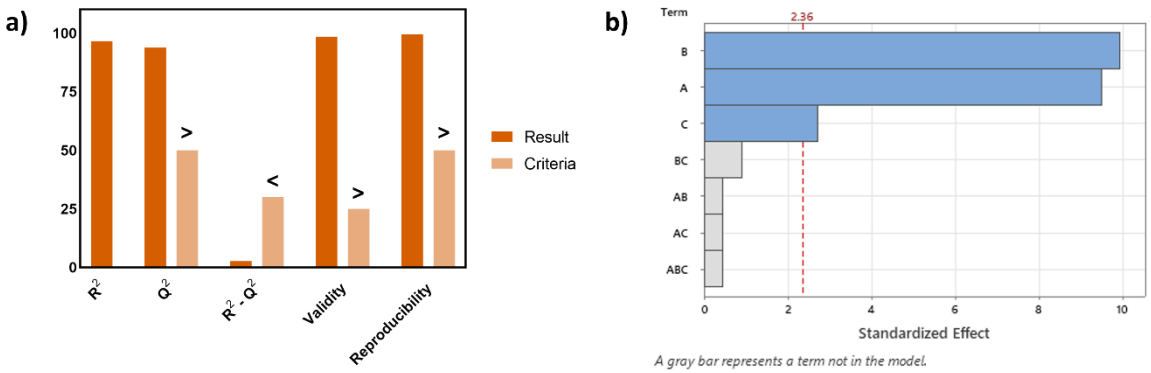

Figure 35 – Analysis of optimised model for Ca/P: a) Summary of Fit; b) Pareto Chart of standardised effects; c) Factorial Plots.

Equation 14 – Optimised Model for (Ca+Mg+Sr)/P (factor description in Table 15)

$$\frac{Ca + Mg + Sr}{P} = 1.5736 - 0.0300A - 0.0350B + 0.0550C$$

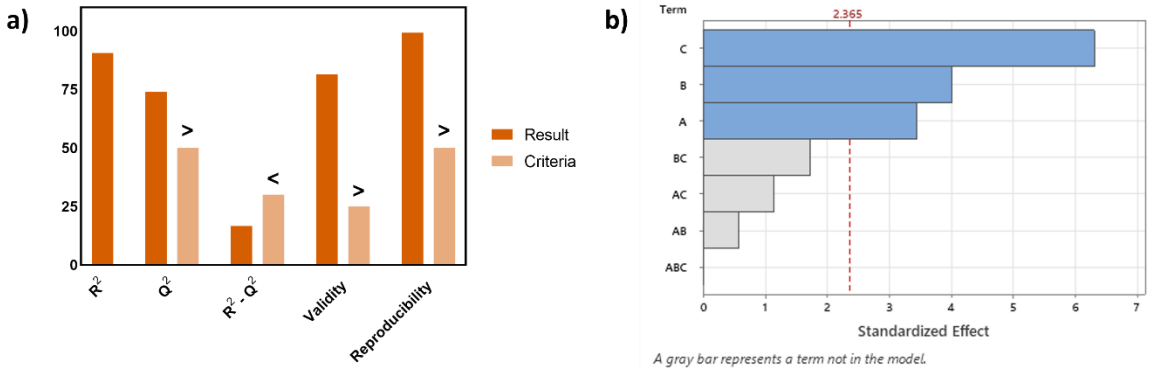

Figure 36 – Analysis of optimised model for (Ca+Mg+Sr)/P: a) Summary of Fit; b) Pareto Chart of standardised effects.

Equation 15 – Optimised Model for Mg % (λ = 4, g = 6.06826, factor description in Table 15)

$$\frac{Mg\ \%^{\lambda-1}}{\lambda \times g^{\lambda-1}} = 3.803 + 3.109A + 3.171C + 2.632AC$$

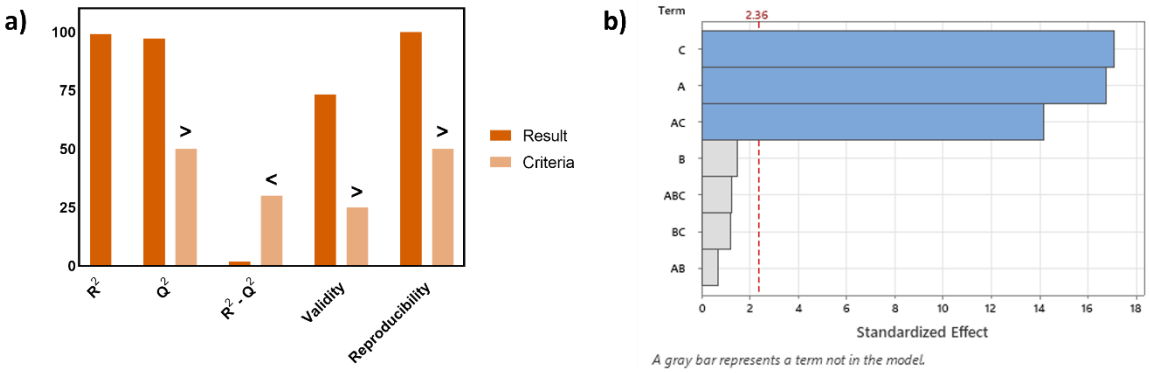

Figure 37 – Analysis of optimised model for Mg %: a) Summary of Fit; b) Pareto Chart of standardised effects.

Equation 16 – Optimised Model for Sr % (factor description in Table 15)

$$Sr\ \% = 6.8609 + 1.9575B$$

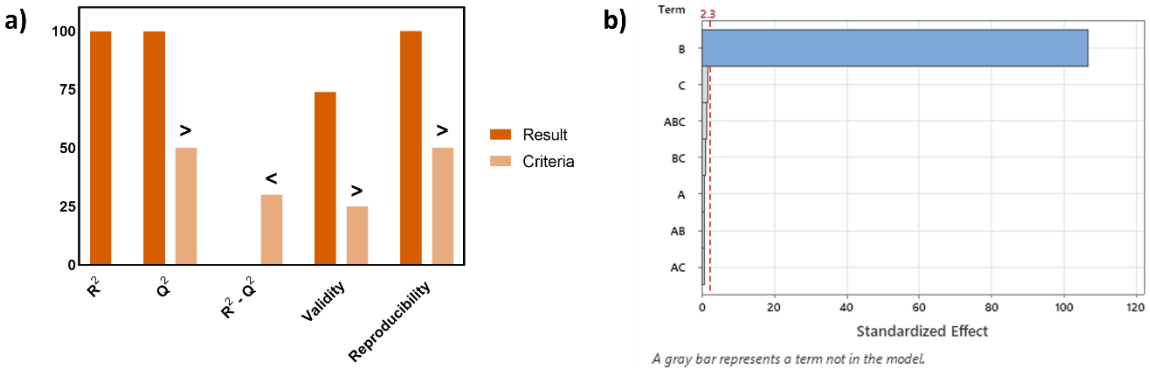

Figure 38 – Analysis of optimised model for Sr %: a) Summary of Fit; b) Pareto Chart of standardised effects.

Equation 17 – Optimised Model for HAP Phase % (λ = 10, g = 93.3001, factor description in Table 15)

$$\frac{HAP\ Phase\ \%^{\lambda-1}}{\lambda \times g^{\lambda-1}} = 10.774 - 4.86A$$

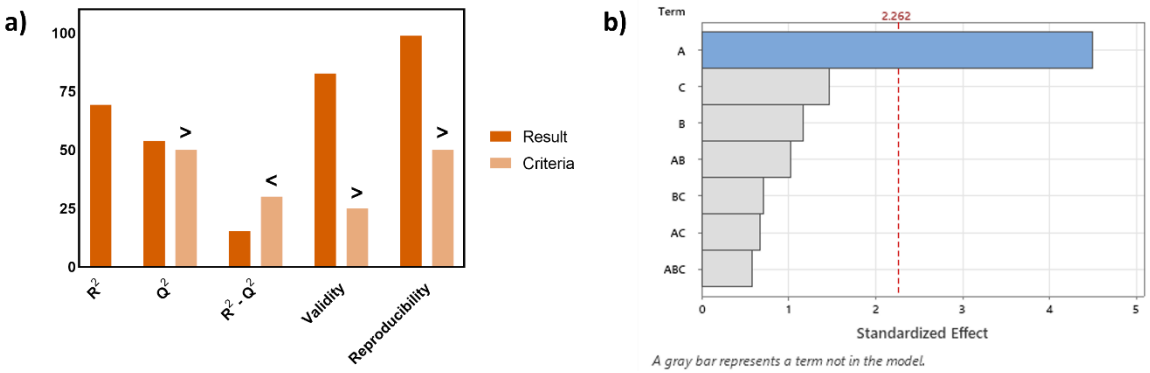

Figure 39 – Analysis of optimised model for HAP Phase %: a) Summary of Fit; b) Pareto Chart of standardised effects.

As predicted, both Mg % and HAP Phase % had to be transformed to guarantee linearity. Moreover, all models were able to pass all four Summary of Fit tests, indicating their validity to be used in the study of how the synthesis conditions affect the different physicochemical properties of sHAP.

Starting with the Ca/P ratio, the model from Equation 13 reveals that all factors in study influence it. Specifically, high concentrations of Mg and Sr lower the Ca/P ratio, which gets higher when ammonia is present in higher volumes. Moreover, the results suggest that ammonia might also aid in the incorporation of Ca. Interestingly, no interaction effect between any pair of factors seems to affect the ratio.

Similarly, the (Ca+Mg+Sr)/P ratio (Equation 14) seems to be affected only by the individual effects of each factor, decreasing with higher levels of Mg and Sr, and

increasing with the use of higher volumes of ammonia. While the effects from Mg and Sr were within expectations, the effects of ammonia were surprising. Compared to Ca/P, the volume of ammonia used has a higher impact in (Ca+Mg+Sr)/P, being the highest affecting factor in the new model and the least affecting in the former one. This suggests that ammonia might affect the incorporation of not only Ca but also of at least one of the substitutions. The model for Mg% (Equation 15) confirms this hypothesis, as it shows that higher levels of ammonia significantly help with the incorporation of Mg into the HAP structure, both individually and in combination with the Mg levels used during synthesis. Interestingly, when analysing both the Mg% model and Sr% model (Equation 16), we can see that the incorporation of one of the ions is not affected by the other. Moreover, the incorporation of Sr seems to be only dependent on the Sr levels used during synthesis. These results suggest that, for the concentrations in study, there is no competition between both ions for the incorporation into the HAP structure. It also suggests that the incorporation of Sr into HAP is easier than the incorporation of Mg.

In fact, the difficulty in incorporating Mg might explain the results from the HAP Phase % model, where Mg % is the only factor significantly affecting the relative quantity of HAP being synthesised, which decreases with higher amounts of Mg used.

6.4.4. sHAP can increase the osteogenic potential of immortalised MSCs without affecting cell viability

Figure 40 summarises the metabolic activity of the hTERT-MSCs Y201 when exposed to sHAP on days 7 and 14, and how it compares to the control groups. As observed, the metabolic activity of the Y201 cells exposed to any of the sHAP synthesised for the DoE was always of the same magnitude as that of the control groups, both on day 7 and day 14, with no negative statistical differences detected.

These results indicate that neither of the synthesised sHAP has a cytotoxic effect on Y201 cells and, as such, might also not be cytotoxic *in vivo.* Because no cytotoxic effect was detected, it was decided to not analyse this response using DoE.

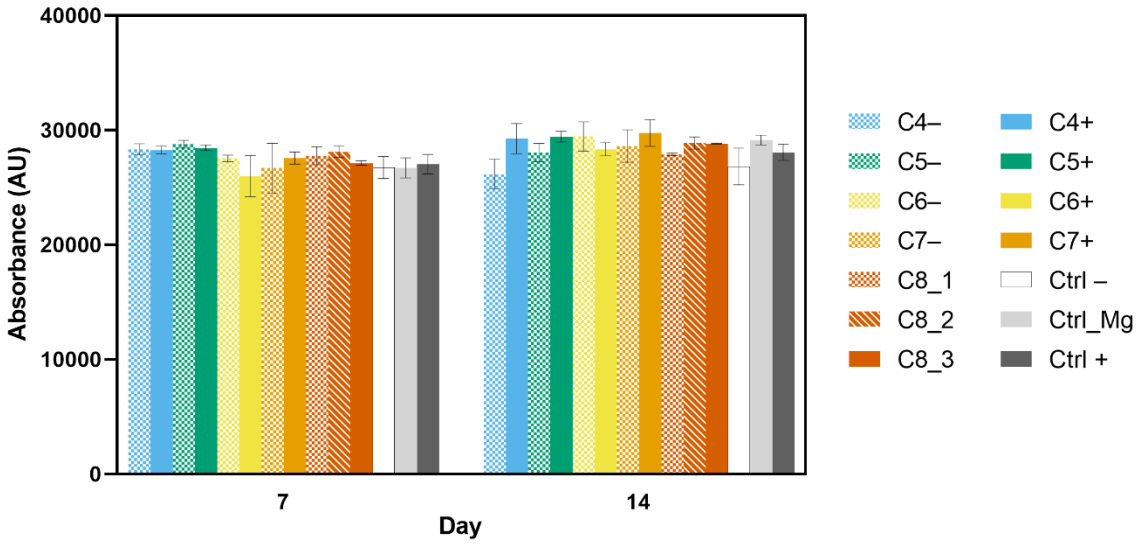

Figure 40 – Metabolic activity by resazurin reduction of hTERT-MSCs Y201 when exposed to different sHAP (mean + standard deviation, n = 3).

Figure 41 summarises the results in DNA-adjusted ALP activity of the same Y201 cells at day 14. While none of the synthesised sHAP samples were able to reach activity levels as high as those of cells cultured in osteogenic media (Ctrl +), two formulations, C4+ and C6– showed a significant increase in ALP activity when compared to cells cultured in expansion media (Ctrl –) and cells exposed to Mg-enriched sHAP from the industrial partner (Ctrl_Mg). Furthermore, sHAP synthesised following C4– showed a significant increase in ALP activity compared to Ctrl –, but not to Ctrl_Mg. These results already indicate the success in the synthesis of sHAP

with enhanced osteogenic potential. However, it is still of interest to study how these results could be further optimised using DoE.

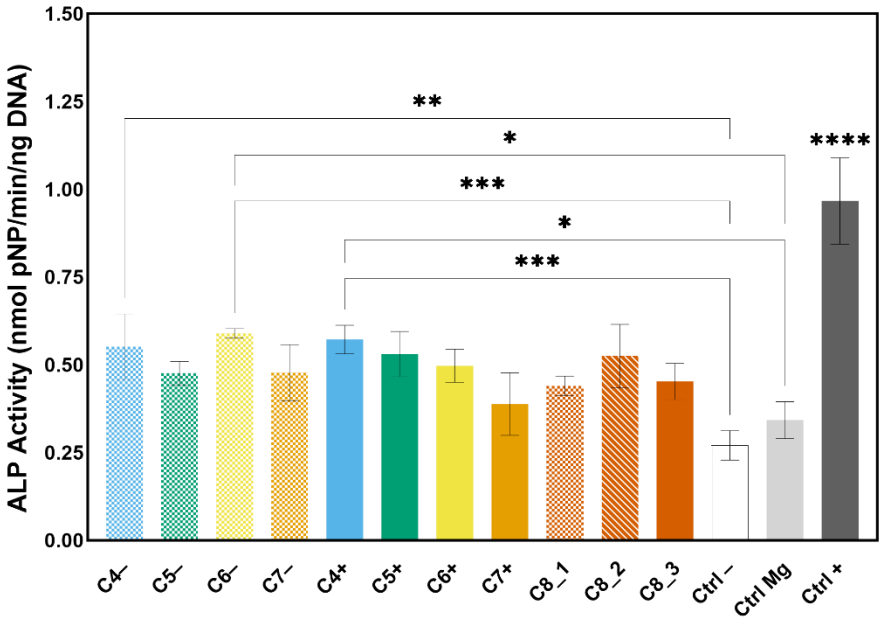

Figure 41 – DNA-adjusted ALP activity of hTERT-MSCs Y201 when exposed to different sHAP at day 14 (mean + standard deviation, n = 3; * p < 0.05; ** p < 0.01; *** p < 0.001; **** p < 0.0001).

DoE analysis was performed using the average DNA-adjusted ALP activity of all runs as the design response, excluding the control groups. Figure 42 shows the replicate plot for this response. As it is observable, the main runs can be easily divided into two halves. However, because the centre points are not equidistant from both halves, the responses might need to be transformed to ensure linearity by using the automatic function of the software *Minitab 20.0*.

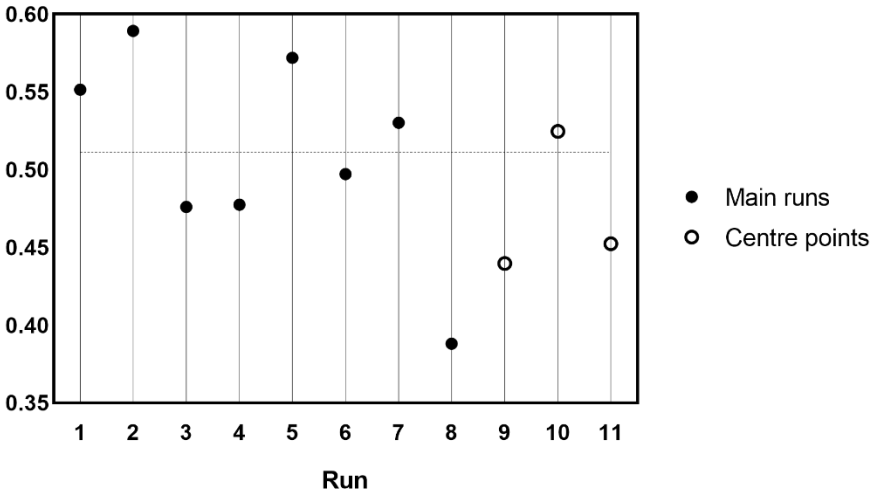

Figure 42 – Replicate plot for DNA-adjusted ALP.

Equation 18 shows the best model that was possible to be obtained for ALP activity. To ensure the model was able to pass all summary of fit tests, the effect of the centre point runs (cp) had to be included. The need for cp to be present in the model is an indicator that the real response shows curvature and that a linear model might not be the most indicated for optimising sHAP according to its osteogenic potential. This might explain why all possible factors and interactions needed to be present in the model for it to be considered valid, even if only factor B (targeted Sr%) was shown to be significant (see Figure 43).

Equation 18 – Model for DNA-adjusted ALP activity (factor description in Table 15)

$$ALP^{1.95} = 0.2727 - 0.0210A - 0.0428B - 0.0126C - 0.0117AB - 0.0321AC + 0.0067BC - 0.0399cp$$

If $A = B = C = 0$*:*
$cp = 1;$
Else:
$cp = 0;$

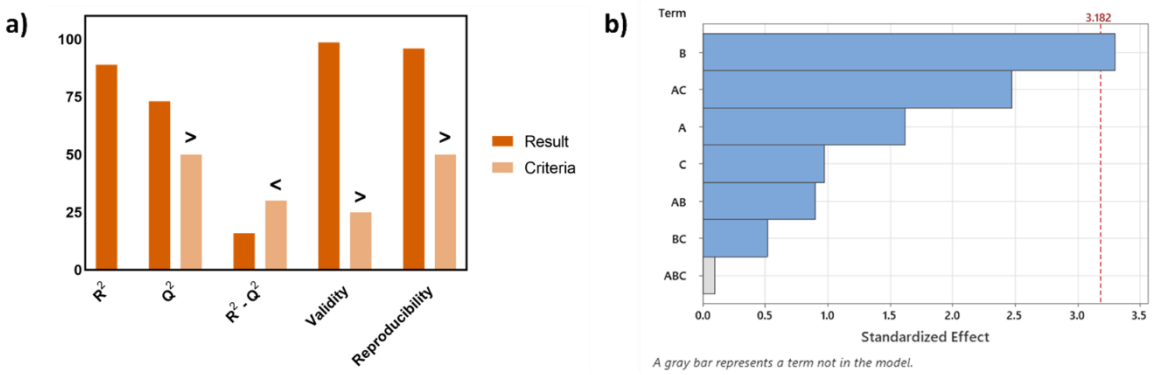

Figure 43 – Analysis of model for DNA-adjusted ALP activity: a) Summary of Fit; b) Pareto Chart of standardised effects.

The main effects plots for this model, present in Figure 44, confirm the suspicions that the real response shows curvature, demonstrated by how far the real centre point is from the theoretical centre, represented by the dashed line. This indicates that a linear model is not suitable for proper optimisation of the osteogenic potential of sHAP, and the DoE approach used should be augmented to be able to predict quadratic effects. Nevertheless, because the objective is to maximise ALP activity and with the effect plots from Figure 44 suggesting this optimal response might be at the corners of the design, it was decided to still use this model to estimate which formulation maximises osteogenesis.

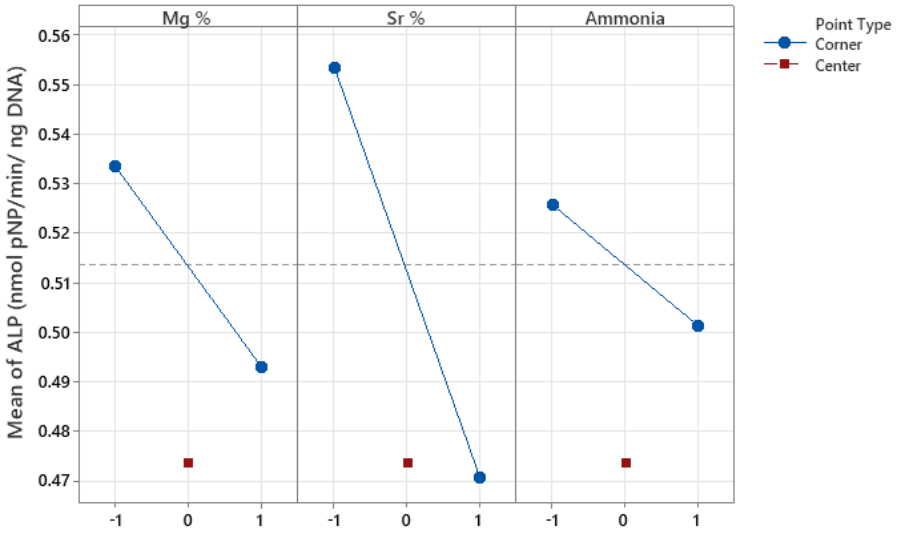

Figure 44 – Main effect plots for the DNA-adjusted ALP activity mode.

Using the response optimiser function from *Minitab 20.0*, it was found that the sHAP has its osteogenic potential optimised when following the conditions described in Table 19. These conditions match those from run 2 from Table 16 (standard order), corresponding to sHAP synthesised using formulation C6 with 15 ml of ammonia. This run did indeed result in the highest average ALP activity from all runs (0.5892 nmol pNP/min/ng DNA), which is close to the response obtained using the model (0.5903 nmol pNP/min/ng DNA).

Table 19 – Optimal synthesis conditions of sHAP optimised for maximum osteogenic potential

Value	Factor		
	A	B	C
Model	+	–	–
Real	10%	5%	15 ml

6.5. Discussion

This chapter studies the synthesis of Mg and Sr-based substituted hydroxyapatite by wet chemistry precipitation. Compared to stochiometric HAP, sHAP presents enhanced bioactivity as it more closely resembles its biological counterpart [46-48]. Furthermore, the specific ionic substitutions, Mg^{2+} and Sr^{2+}, were shown to, respectively, stimulate osteoblasts and new bone formation, and inhibit osteoclasts and bone resorption [47, 48]. The synthesis process used during this research has already been used to create commercially available HAP and Mg-enriched sHAP, and as such it is a good candidate to be optimised for the synthesis of Mg and Sr-based sHAP [49, 111].

The initial synthesis protocol, specifically the protocol present in 4.2.7 and the composition of formulation C0, were all based on the synthesis method used by the industrial partner of the project for their commercially available HAP. The (Ca+Mg+Sr)/P ratio was set as 1.66, instead of the stochiometric 1.67 ratio as slight Ca deficiencies have been shown to stimulate biomineralisation by facilitating the release of ions without compromising too much the stability of HAP [120]. The percentage of Mg and Sr substitutions were based partly on the literature, with different groups investigating total co-substitution levels up to 30%, and partly based on unpublished data from another student involved in a related project to this research work, which studied total co-substitution levels up to 40% and found the best synthesis results were obtained when total substitution levels were not higher than 20% (10% Mg and 10% Sr).

The synthesis of sHAP with different formulations was initially evaluated using FTIR as it could be used to quickly identify the calcium phosphate being synthesised, and due to the equipment being readily available to use at the laboratories of the industrial partner, where the bulk of the experimental work took place. As explained in 6.4.1, pure HAP was synthesised using the formulation C0 to serve as a standard to which all the synthesised sHAP would be compared to. The closer the FTIR

spectrum of the analysed sample was to that of C0, the more likely it was that this sample resulted in sHAP being synthesised. The initial FTIR results, which analysed samples synthesised without ammonia solution (in other words, without controlling pH), have shown that only formulation C4, which had the lowest substitution levels overall (both Mg and Sr at 5%) resulted in samples with a spectrum similar to that of C0 and, as such, was the only formulation which led to sHAP being created. These preliminary experiments were used to assess if the current synthesis method could be performed as is, or if any optimisation would be necessary. As only one of the formulations in the study resulted in sHAP being synthesised, the synthesis method did indeed need to be optimised for producing sHAP with different substitution levels.

The main suspect for the problems with obtaining sHAP was the evolution of the pH during the synthesis process. The optimal pH for HAP production is within the 10 – 12 range, as it promotes the dissociation of H_3PO_4 into H^+ and PO_4^{-3} [117, 118], which is easily obtained with the pure $Ca(OH)_2$ basic solution prepared for formulation C0 (a saturated solution of $Ca(OH)_2$ has a pH of 12.45) [121]. However, as $Mg(NO_3)_2$ and $Sr(NO_3)_2$ are both salts that acidify the aqueous solution during dissolution (acidic salts, with a pH of 5.2 and 5.8, respectively) [122], it was suspected that these could compromise pH during synthesis, especially since it already involves the addition of orthophosphoric acid. These assumptions could explain why only formulation C4 was able to successfully synthesise sHAP: the lower concentrations of both precursors could also lower their effect on pH during synthesis.

The suspicions about the effect of pH were deemed correct during the experiments detailed in 6.3.2. Formulation C6 was chosen to study pH evolution during synthesis as the previously mentioned unpublished research was able to synthesise sHAP without controlling pH using the exact same reagents and concentrations from Table 11, albeit using a different synthesis method. It is important to notice the change of Mg precursor to $MgCl_2 \cdot 6H_2O$ did not affect the previous assumptions, as it is also an acidic salt like $Mg(NO_3)_2$ [123]. As seen in

Table 17, while the pH remained at an ideal 12 during the first 45 minutes of the synthesis process, it did drop to 10 after this time point, dropping even further to 6 just five minutes later. Adding ammonia solution to keep pH at the optimal range whenever it dropped during synthesis, as well as preventive additions during the first hour after synthesis, was sufficient to successfully obtain sHAP, as seen in Figure 30. As such, it was decided that all subsequent synthesis rounds would include a specific amount of ammonia solution to counteract the possible pH drop from the beginning.

Adding ammonia to the synthesis did introduce a new problem however, as the centrifugation-based washing method previously used was not effective enough to remove all traces of ammonia from the sHAP samples, as indicated by the subtle peaks detected at 3300 and 2900 cm^{-1} in FTIR spectrum of the new samples [119]. As ammonia is a toxic reagent [124], an effective washing step is crucial for materials aimed towards medical applications. Adding three extra centrifugation steps to the initial three was enough to eliminate ammonia from the sHAP (see Figure 31), however, it also led to a doubling of the time used for the washing of the samples. This increase in time could be problematic when scaling up the synthesis to industrial levels, especially when using the formulations set by Table 13, which are based on the concentrations used by the industrial partner and result in more HAP being synthesised at once when compared to the formulations from Table 11. As Table 14 and the results from Figure 32 show, using vacuum filtration instead of centrifugation allowed for much more effective washing of sHAP, as the removal of ammonia was done in just 3 washing steps, regardless of the particular filter used. However, it is important to state that filters with high pore size could result in material being lost during the process (see Figure 33), so it is also important to choose filters that maximise final sHAP yield.

The DoE detailed in Table 16 was designed to check the effect of substitution degrees and ammonia levels used during synthesis on the physicochemical properties of the obtained sHAP, as well as their effect on the differentiation of

MSCs. The Mg% and Sr% levels used in the design allowed us to obtain sHAP following all formulations in Table 13. Specifically, it enabled sHAP to be synthesised following formulations C4 to C7 with either high or low ammonia, and following C8 with middle levels of ammonia. As for the ammonia levels, 50 ml was chosen as the + level as it facilitated the preparation of the 500 ml of basic solution (450 ml of ultrapure water + 50 ml of ammonia solution). The – and 0 ammonia levels were chosen both to have volumes similar to those used during the experiments detailed in 6.3.2 (15.0 ml is close to the 18.0 ml used during the synthesis process, 32.5 ml is close to the 33 ml used during the entire experiment), as well as to follow the design rules for full factorial designs (see 2.7.1.1). ICP-OES was used to make a quantitative analysis of the composition of each sample, from which it was possible to calculate the real ratios between chemical elements, as well as substitution degrees. XRD was used both to more precisely identify the calcium phosphates being synthesised, as well as their crystallinity. Finally, the *in vitro* assays were conducted to infer the cytotoxicity of each sHAP sample, as well as their osteogenic potential in MSCs.

Even before the proper DoE analysis, by analysing Table 18 it is possible to see the effect of the different factors on different physical-chemical properties of the synthesised sHAP. In general, while all samples resulted in a large amount of sHAP being synthesised (between 80% and 100% of the analysed sample), the samples which had higher levels of ammonia and, consequently, had a higher pH after synthesis, were also the samples that resulted in higher quantities of sHAP being produced. Moreover, it is possible to see that lower total substitution percentages also result in higher quantities of sHAP being created, and that the inclusion of Mg might have more of a negative impact on the synthesis process than Sr.

The Mg levels themselves also seem to be affected by pH, as its presence in the crystal structure is much closer to the theoretical values when using higher volumes of ammonia. These results could be related to the difficulty in integrating Mg into sHAP that previous researchers have found [125, 126], which could be

facilitated when pH is closer to optimal. Interestingly, the secondary phases detected during XRD are different depending on how much ammonia was used during the process. When using lower volumes, the secondary phase is mainly brushite, the same as detected by FTIR during the initial, ammonia-free, synthesis, while higher volumes of ammonia resulted in struvite, a phosphate mineral with the formula $NH_4MgPO_4 \cdot 6H_2O$. This indicates that excess ammonia could remove Mg^{2+} and PO_4^{3-} ions from the sHAP synthesis and introduce a potential contaminating phase to the sample being synthesised. The presence of struvite could also explain the higher levels of Mg detected during ICP-OES: it is possible that the sHAP being synthesised is still Mg-deficient compared to the theoretical values, and that the higher levels of Mg detected are coming from the struvite present in the sample. Another reason for the Mg levels possibly being affected by pH is that the actual substitution levels for samples C6 and C7 (both targeting 10% of Mg) synthesised in low ammonia are closer to the levels targeted by formulations C4 and C5 (both targeting 5% of Mg), respectively, making them closer to Ca-deficient C4 and C5 sHAP samples.

Starting the analysis of the obtained DoE models with the one for Ca/P ratio, the obtained results indicate that higher initial levels of Mg and Sr lower Ca/P. On the other hand, higher levels of ammonia result in an increase in said ratio. The first two results are not surprising, as the amount of Ca precursor is adjusted per total substitution to keep (Ca+Sr+Mg)/P equal to 1.66 (see Table 13). The positive effect of ammonia could perhaps be explained by the pH being closer to the ideal 10-12 range for HAP production: because that interval promotes the dissociation of H_3PO_4, the increase in dissociated PO_4^{3-} ions could potentially facilitate the recruitment of Ca^{2+} ions, although it cannot be discarded that ammonia is also having a direct effect in Ca^{2+} as well.

Not surprisingly, similar effects were found for the (Ca+Mg+Sr)/P model, although the reasoning might differ. Because the theoretical (Ca+Mg+Sr)/P is the same across all sHAP, the lowering effect of Mg% and Sr% indicates that the higher

the targeted substitution, the harder it is for each ion to be incorporated into the crystal structure, lowering the ratio obtained. Ammonia is still found to have a positive effect on the ratio, albeit a stronger one compared to the Ca/P model. This could be due to the possible position effect of ammonia in the incorporation of Mg. It could also be due to ammonia's role in controlling pH during sHAP synthesis, promoting the dissociation of H_3PO_4. Interestingly, no interaction effect between any pair of factors was deemed statistically significant on either ratio in the study.

The Mg% model confirms the positive effect of ammonia in the incorporation of Mg^{2+} into sHAP, as well as the effect of the target Mg substitution degree, and a positive effect of the combination of those two factors. The effect of ammonia and its interaction with the targeted Mg substitution, however, might be harder to explain. It is possible that, like H_3PO_4, $MgCl_2 \cdot 6H_2O$, which is an acidic salt, dissociates easier in basic environments due to its acidity, which in return allows it to better incorporate into the sHAP structure. Interestingly, the incorporation of Sr seems to only be affected by the initial concentration of precursor used, with no other factor affecting its incorporation. More interestingly, the incorporation of either Mg or Sr seems to be independent of one another, suggesting that there is no competition between these ions to be incorporated into the crystal structure of sHAP. This may be because the overall composition of each formulation, specifically the amount of $Ca(OH)_2$ and H_3PO_4, guarantees that all substituting ions could potentially be incorporated into the crystal lattice of the sHAP being synthesised.

The most surprising DoE results come from the HAP Phase %, where only the Mg levels seem to affect the ratio of HAP being synthesised during each run, which lowers with increasing levels of Mg. These results might come from the difficulty Mg^{2+} ions have in entering the crystal lattice when compared with Sr^{2+} ions, which in turn could affect the synthesis of sHAP, favouring the formation of other minerals. The difficulty in incorporating Mg^{2+} ions might come from the difference in size between it and Ca^{2+} ions being larger than the difference between Ca^{2+} and Sr^{2+} ions. For comparison, the ionic radius of Mg^{2+} is 88 pm, for Ca^{2+} it is 114 pm, and for Sr^{2+} it

is 132 pm [127], giving a difference of 28 pm and 18 pm, respectively. Furthermore, the role Mg^{2+} has in the synthesis of struvite, again a secondary phase detected during XRD with a formula of $NH_4MgPO_4 \cdot 6H_2O$, might also increase its negative effect on HAP Phase %. Curiously, this might explain why ammonia does not seem to have a significant effect on this model: the positive effect it has from keeping pH within the ideal range for HAP synthesis might be negated by the role it also has in the creation of struvite.

It was not possible, however, to model crystallinity due to the large variability detected in its centre point runs, which was of the same magnitude as the variability detected in the main runs. However, the results suggest that there might be something of notice occurring, as the average crystallinity of the centre point runs seems higher than any of the main runs, indicating that a linear model might not be sufficient in this case. In the future, it might be of interest to study crystallinity with a DoE strategy that allows the formulation of quadratic models, as well as including other factors to the system. Specifically, it is suspected that the duration of both the incubation and drying periods might affect the crystallinity of sHAP, by providing the system with more energy that could be used to promote crystallisation (see Equation 23 in Chapter VII). It is important to note that neither time was constant during this work, only described as “overnight”. The different incubation and drying periods during each run may explain the high variability detected.

Regarding the biological performance of sHAP, all samples were shown to not be cytotoxic, as they were shown to not affect the metabolic activity of Y201 cells when compared to different control groups: a negative control in media used just for cell expansion (Ctrl –), a positive control in media that induces osteogenic differentiation (Ctrl +), and a different positive control, of cells exposed to commercially available Mg-enriched HAP (Ctrl_Mg), produced by the project’s industrial partner. These results are a good sign that the synthesised sHAP is biocompatible and that the washing method used successfully removed any traces of ammonia, which can be toxic. It is important to notice that the cells were not in direct

contact with the sHAP samples, which would be more representative of *in vivo* applications. As such, it is possible that sHAP could still have a negative impact on cell viability when Y201 cells are directly exposed to the material, even if the obtained results are a good indicator that the synthesised samples are biocompatible. To note that other studies have also not found toxicity issues when culturing MSCs in direct contact with different HAP-based materials.

As for the osteogenic differentiation potential of the samples, while only three samples were shown to significantly increase ALP activity compared to Ctrl –, and only two of those were shown to perform significantly better than Ctrl_Mg, all sHAP samples resulted in a higher average ALP activity than the average values for both Ctrl – and Ctrl_Mg cells (see Figure 41). As a reminder, alkaline phosphatase or ALP is an enzyme which can be considered an early marker of osteoblast differentiation, increasing in activity before active bone formation [106]. While none of the samples, including the commercially available sHAP, can stimulate the ALP levels to those reached by Ctrl + cells, these results are a good indicator that it was indeed possible to synthesise Mg and Sr sHAP able to influence the differentiation of MSCs with enhanced potential compared with already available materials.

It is interesting, however, that the three compositions which presented the best results all had similar real substitution levels (see Table 18), and all were closer to formulation C4 (5% Mg and 5% Sr). This includes the best overall sample, which was synthesised during run 2 following formulation C6 (10% Mg and 5% Sr) with low ammonia. This sample is closer to being a Ca-deficient sHAP following formulation C4. As a reminder, all samples are already synthesised to be slightly Ca-deficient, as it has been shown that Ca-deficient HAP has better biological performance than stochiometric HAP due to better ion release [120]. The higher Ca deficiency levels from the run 2 samples may be partly responsible for it being the best-performing sHAP. However, it is important to notice that both C4 samples (runs 1 and 5) performed relatively similarly to run 2, so perhaps the real effect comes from an optimal substitution level. Moreover, the higher substitution levels could lead to an

inappropriately fast degradation profile which might compromise their effectiveness as an implant or coating material.

Instead, it may be the substitution levels that might be affecting the differentiation of Y201 cells. Considering that no cytotoxic behaviour was detected on any sample, it is possible that the higher ionic substitution levels from all other samples compared to runs 1, 2 and 5 hinders the differentiation of Y201 cells or stimulates different cellular phenomena. As an example, a study which also explored different Mg and Sr sHAP formulations showed that the osteogenic activity of MG63 cells was enhanced with an sHAP that aimed towards 10% of Mg substitution but only reached around 5% substitution levels, similar to the current results [128]. Interestingly, their best formulation targeted a 20% Sr substitution degree, with the real levels closer to 10%. In other words, their best formulation was closer to formulation C5 (5% Mg and 10% Sr) from this research, instead of C4. However, it is important to note that the researchers conducted their *in vitro* studies on MG63 cells, which are osteoblasts derived from a cancer cell line. In contrast, this study used Y201 cells, which is an immortalised MSC line. It is possible that higher Sr levels are more favourable to one cell line, while lower Sr levels are better suited for the other.

Finally, it is important to note that the results obtained during this research were also conducted using an immortalised cell line. It is possible that, instead of samples from run 2, samples from another run could be found as the most suitable for primary MSC cells, which are more representative of the cells these materials would encounter *in vivo* [81]. It is also possible that different sHAP samples could perform better for primary cells from different individuals. This opens the possibility that a DoE strategy such as that used here (or a strategy able to calculate quadratic effects) could be used for the development of patient-specific sHAP, using the optimisation models to infer which sHAP formulation would be more suitable for individual cases.

6.6. Summary

In this work, Mg and Sr sHAP was developed with enhanced osteogenic potential when compared to commercially available materials. DoE was used to study how different synthesis conditions affect the physicochemical properties of sHAP, as well as their biological performance. It was shown that, alongside the target substitution levels, pH was also an important factor in the synthesis of sHAP. Controlling the pH minimised the synthesis of other calcium phosphates, and facilitated the incorporation of Mg into the crystal structure of the mineral. It was also found that Mg levels significantly impact the synthesis of sHAP, with increasing levels promoting the creation of other mineral phases. Despite no competitive behaviour between ions being detected, Sr was more easily incorporated into sHAP. Finally, it was shown that the osteogenic potential of sHAP in Y201 cells was enhanced when the real substitution levels were around 5% for each ion, with formulation C6 synthesised with low ammonia volumes providing the best results.

VII. Synthesis of crystalline titanium dioxide at low sintering temperatures

7.1. Introduction

Coating orthopaedic implants with osteoinductive materials is a common strategy used to improve their integration to bone [43, 54, 56, 129], with one such material being titanium dioxide (TiO_2) [54-56, 129]. In fact, the spontaneous formation of a TiO_2 layer in titanium-based implants is directly linked to their biological performance, providing the implant with a more bioactive surface that also acts as a shield against wear and corrosion [26, 54, 55]. It is expected that coating an implant with TiO_2 would provide it with those same properties.

One technique that can easily be explored in the synthesis of TiO_2 coatings is sol-gel chemistry [56, 130-133]. This technique, involving the hydrolysis of specific reagents to obtain a sol that condensates into a gel which can be used to coat a substrate, is particularly interesting as it allows the creation of high-purity ceramic coatings using inexpensive materials and simple coating techniques such as dip coating [40, 63, 130]. Furthermore, sol-gel coatings are also particularly rich in -OH groups which increase their bioactive potential [66, 67].

The bioactivity of TiO_2 is further improved by inducing crystallisation, and TiO_2 obtained through sol-gel chemistry can easily crystallise to anatase when sintered at temperatures between 400 to 500°C [57-60]. While most metallic implants are able to sustain temperatures within that range, the same cannot be said for implants based on polymeric materials. For example, PEEK, a polymer that has increasingly been explored for orthopaedic applications due to its radiotransparency, bioinert behaviour and mechanical properties (see Chapter II), similar to those of bone, has a maximum service temperature around 250°C [12, 14, 134].

Osteoinductive crystallised TiO_2 coatings for polymeric implants have been developed in the past, including by exploring sol-gel chemistry [133, 135-138]. However, these solutions are generally based on pre-crystallising TiO_2 and/or generally involve coating techniques and extra steps that lack the high quality at low-cost benefits of sol-gel dip-coating. Other fields of engineering, especially those that benefit from the photocatalyst and self-cleaning characteristics of TiO_2, have shown it is possible to lower the crystallisation temperature of TiO_2 by fine-tuning the conditions in which the sol-gel process occurs, namely by controlling the energy provided during synthesis, pH and water content [72-75]. This has allowed them to obtain crystallised TiO_2 coatings on different substrates, including polymeric ones, by dip-coating and sintering at lower temperatures.

Due to the added benefits presented by crystallised TiO_2 regarding osteointegration compared to its amorphous counterpart, this chapter aims to research which conditions allow TiO_2 obtained through sol-gel chemistry to crystallise at temperatures that are sustainable by PEEK substrates.

7.2. Aims and Objectives

The aim of this chapter was to find the optimal synthesis conditions that allow TiO_2 with high crystallinity to be obtained when sintering at low sintering temperatures, while also minimising the presence of organic residues from the sol-gel process. From the obtained results, it will be decided what synthesis conditions will be explored for the development of TiO_2/HAP coatings (see Chapter VIII). To achieve this goal, the following objectives were addressed:

I. Pre-screen the best synthesis, sintering and drying conditions for the remaining objectives of this factor.
II. Study using DoE how the sol-gel synthesis and sintering conditions affect the organic residue content and the crystallinity of TiO_2 samples.

III. Use the obtained DoE models to determine synthesis conditions that simultaneously result in TiO_2 with high crystallinity and low organic residues.

7.3. Materials and Methods

The following Materials and Methods are specific to this chapter. For general details please check Chapter IV.

7.3.1. TiO_2 sintering conditions – design of experiments approach

TiO_2 was synthesised as stated on 4.2.12, with the following modifications:

- AcOH was added immediately after starting the hydrolysis of TTIP.
- The synthesis beaker was not covered with punctured aluminium foil.
- The synthesis was conducted at room temperature.
- The reaction was stopped 10 minutes after adding AcOH.

The synthesis was conducted using 19.0 ml of EtOH, 0.9 ml of ultrapure water and 4.1 ml of AcOH. The obtained sol was transferred to a 50 ml falcon tube and centrifuged at 6000 rpm (5070 rcf) for 10 minutes, in a benchtop centrifuge (XS R-8D, Remi group). After centrifugation, the sample was transferred to a beaker covered with parafilm and dried overnight on a hotplate directly set to 50°C. To evaluate the effect of the sintering conditions on the removal of organic residues from sol-gel TiO_2, a full factorial design was used. Table 20 details the factors and conditions studied, while Table 21 summarised the experimental design.

Table 20 – Sintering conditions DoE: factor description

Factor	Description	–	0	+
A	Temperature (°C)	200	225	250
B	Heating rate ΔT (°C/min)	4	12	20
C	Sintering time (hours)	1	3.5	6

Table 21 – Sintering conditions DoE: design summary

Standard Order	Run Order	A	B	C
1	4	–	–	–
2	9	+	–	–
3	5	–	+	–
4	6	+	+	–
5	8	–	–	+
6	11	+	–	+
7	7	–	+	+
8	10	+	+	+
9	1	0	0	0
10	2	0	0	0
11	3	0	0	0

For each sample, 100 mg were sintered in an oven (FD Series 9010-0082, Binder), following the respective conditions from Table 21. The sintered samples were analysed three times by TGA/DSC, as stated in 4.2.16. The DoE was analysed using the software *Minitab 20.0*, and the weight loss was attributed to the degradation of organic material used as the design response.

7.3.2. TiO_2 drying conditions

Three different TiO_2 samples were synthesised as stated in 7.3.1. After centrifugation, however, each sample was transferred to a glass petri dish and dried uncovered following one of the methods from Table 22.

Table 22 – Drying methods

Method	Description
1	Hot plate at 50°C, controlled directly on hotplate
2	Hot plate at 50°C, controlled by measuring temperature of beaker with 40 ml H_2O
3	Vacuum oven at 50°C and vacuum of 300 mbar

For each sample, 100 mg were weighted and sintered at 250°C for 6 hours with ΔT of 20°C/min, using the same equipment used in 7.3.1. Each sample was analysed by TGA/DSC before and after sintering, also as stated in 7.3.1.

7.3.3. Further synthesis improvements

Two different TiO_2 samples were synthesised as stated in 7.3.1. As one had no signs of TiO_2 precipitation, said sample was transferred into a 50 ml falcon tube for 7 days (labelled “no early precipitation”). The remaining sample was labelled “early precipitation.” A third sample was also synthesised, this time with AcOH added before adding ultrapure water, and with the reaction occurring for 24 hours at 50°C, in a beaker covered with punctured aluminium foil. This sample was labelled “AcOH before H_2O”. After their respective synthesis time, each sample was centrifuged as stated in 7.3.1 and dried following method 2 from Table 22. After drying, each sample was weighed, and its final weight was compared to the theoretical value (≈1038.3 mg of TiO_2 for 3.9 ml of TTIP).

7.3.4. Low-Temperature crystallisation of TiO_2 – design of experiments approach

The ability to crystallise TiO_2 at lower temperatures by tuning the synthesis and sintering conditions was studied using a definitive screening design. Table 23 details the factors and conditions studied, while Table 24 summarises the experimental design.

Table 23 – Low-temperature TiO_2 crystallisation: factor description

Factor	Description	–	0	+
A	Reaction temperature (°C)	50	60	70
B	EtOH volume (ml) (TTIP/EtOH molar ratio)	15.2 (1/20)	22.3 (1/30)	30.4 (1/40)
C	H_2O volume (ml) (TTIP/H_2O molar ratio)	1 (1/4)	2 (1/8)	3 (1/12)
D	AcOH volume (ml) (TTIP/AcOH molar ratio)	0.7 (1/1)	2.4 (1/3.25)	4.1 (1/5.5)
E	Heating rate ΔT (°C/min)	4	12	20
F	Sintering time (hours)	1	3.5	6

Table 24 – Low-temperature TiO_2 crystallisation: design summary

Standard order	Run Order	Factor					
		A	**B**	**C**	**D**	**E**	**F**
1	12	0	+	+	+	+	+
2	1	0	–	–	–	–	–
3	6	+	0	+	–	–	+
4	3	–	0	–	+	+	–
5	8	+	+	0	+	–	–
6	11	–	–	0	–	+	+
7	7	+	–	+	0	+	–
8	5	–	+	–	0	–	+
9	4	+	–	–	+	0	+
10	9	–	+	+	–	0	–
11	13	+	+	–	–	+	0
12	2	–	–	+	+	–	0
13	10	0	0	0	0	0	0

For each run, TiO_2 was synthesised as stated in 4.2.12, following the conditions and run order dictated by Table 23 and Table 24. All samples were sintered at 250°C in an oven (LHT 6/30 + 3016 controller, Carbolite Gero). The sintered samples were analysed by TGA and by XRD, following the settings described in 4.2.17 and 4.2.18, respectively. The weight loss attributed to the degradation of organic components, obtained from TGA, and the crystallinity of each sample, obtained from XRD, were used as design responses. The design was analysed using the software *Minitab 20.0*.

7.4. Results

7.4.1. The sintering conditions alter the organic residue contents from TiO_2 samples

TGA/DSC analysis for each sample resulted in graphs like the one from Figure 45, which represent one sample from run 6 (see Table 21). On the sample weight graph (TGA results, black line), it was possible to detect three different weight loss steps, determined using an automatic function from the *TA Universal Analysis* software. The first one, from 40°C to 250°C and accompanied by a subdue exothermic peak on the heat flow graph (DSC results, blue line), represents the evaporation of adsorbed water molecules. The second step, from 250°C to 400°C and accompanied by the first endothermic peak, represents the degradation of organic residues still present on the sample after sintering. The third step, between 400°C and 550°C, represents the crystallisation of the TiO_2 sample into anatase, corroborated by the second endothermic peak within that range.

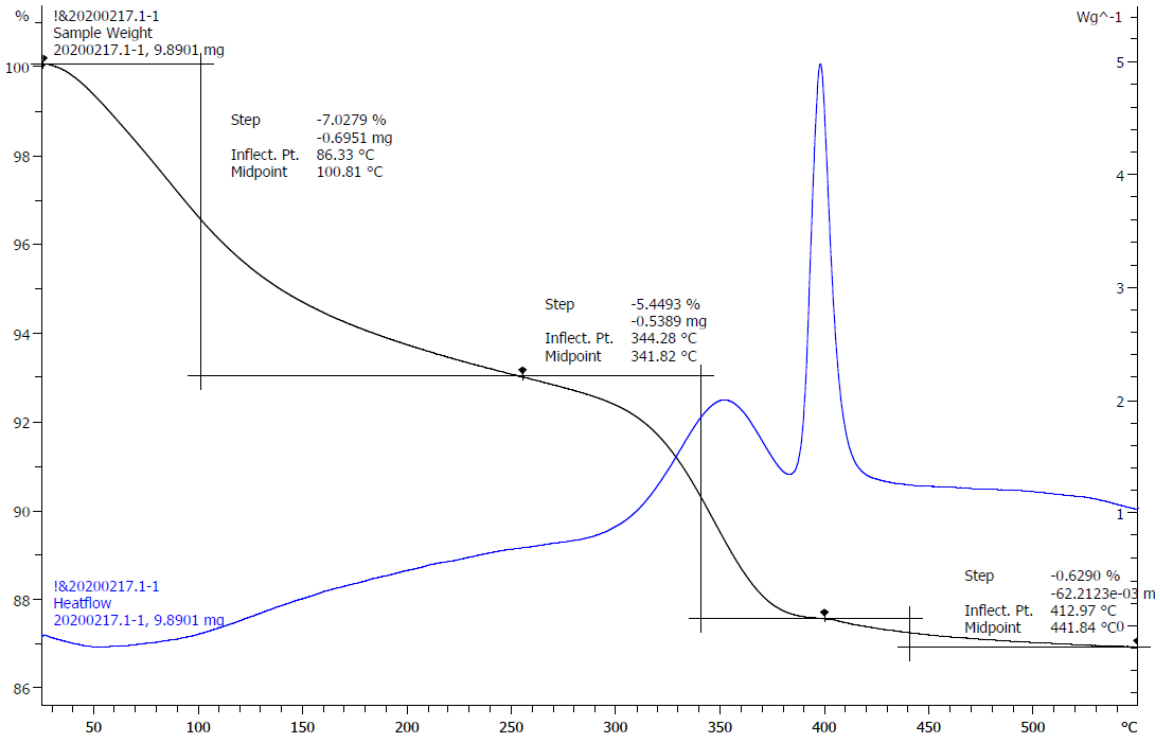

Figure 45 – Example of TGA analysis of a sample from run 6 (Table 21). The black line represents weight loss, while the blue line represents the heat flow through the sample. The three weight-loss steps detected in the black line, and the one exothermic and two endothermic peaks in the blue line correspond, in order, to water evaporation, degradation of organic residues and crystallisation of TiO_2.

The DoE response was set as the average weight loss detected for each sample that has been attributed to the degradation of organic residues, represented by the abbreviation Org. By inspecting Table 25, even before performing the DoE analysis it is possible to see the sintering conditions affecting Org, with values ranging from 5.51% to 18.29%. It is also possible to observe that response variability should be low, as the results from runs 9 to 11 are close in value.

Table 25 – TiO_2 sintering conditions - organic residues results (factor description in Table 20)

Standard Order	Factor A	Factor B	Factor C	Org (%)
1	–	–	–	17.85
2	+	–	–	8.25
3	–	+	–	18.29
4	+	+	–	10.66
5	–	–	+	13.33
6	+	–	+	5.51
7	–	+	+	10.09
8	+	+	+	5.77
9	0	0	0	9.63
10	0	0	0	9.15
11	0	0	0	9.34

Analysing the pre-screening replicate plot and histogram for Org, present in Figure 46, shows that Org can be modelled using the formulated DoE, as runs 1 to 8 can be divided into equal halves of higher and lower results, and runs 9 to 11 are close to each other in value and within the value range of 1 to 8. However, to obtain a valid linear model using DoE, Org might need to be transformed, as the histogram shows the responses skewing towards the left.

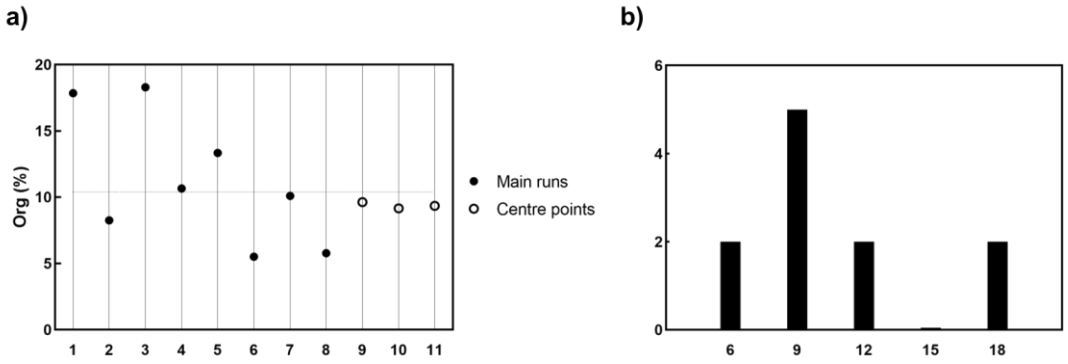

Figure 46 – TiO_2 sintering conditions - Org (%) pre-screening: a) replicate plot; b) histogram.

Transforming Org results to their standard logarithm (log(Org)) solves the problem previously detected. As shown in Figure 47, the histogram is closer to being normally distributed.

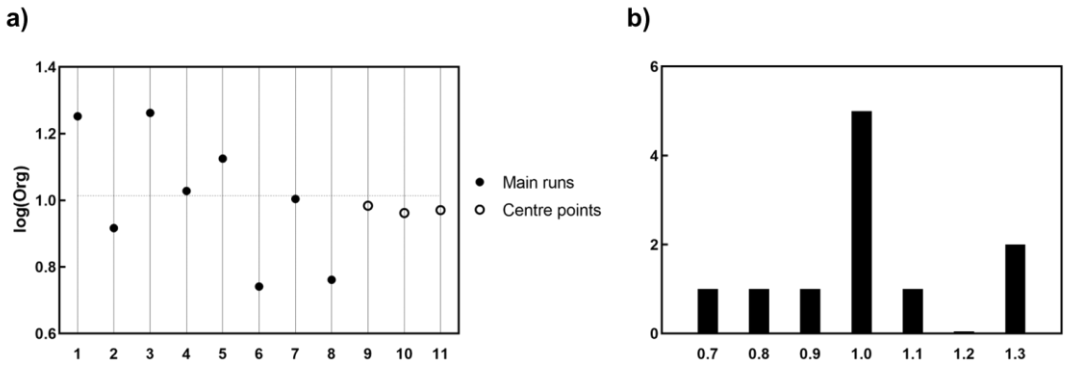

Figure 47 – TiO_2 sintering conditions - log(Org) pre-screening: a) replicate plot; b) histogram.

Equation 19 represents the optimised DoE model for log(Org), while Figure 48 illustrates the Pareto chart of the standardised effects of the same model. The model shows that factors A and C (Temperature and Sintering Time, respectively) are the factors that most significantly affect log(Org) and, consequently, Org. It is also possible to observe that the interactions of factors A and C with factor B (ΔT) affect log(Org) significantly as well. Finally, Figure 49 shows the model passes all four Summary of Fit tests, confirming the model can be considered valid.

Equation 19 – Optimised DoE model for log(Org) (factor description in Table 19)

$$\log(Org) = 1.00041 - 0.1495A + 0.0026B - 0.1034C + 0.0302AB - 0.0278BC$$

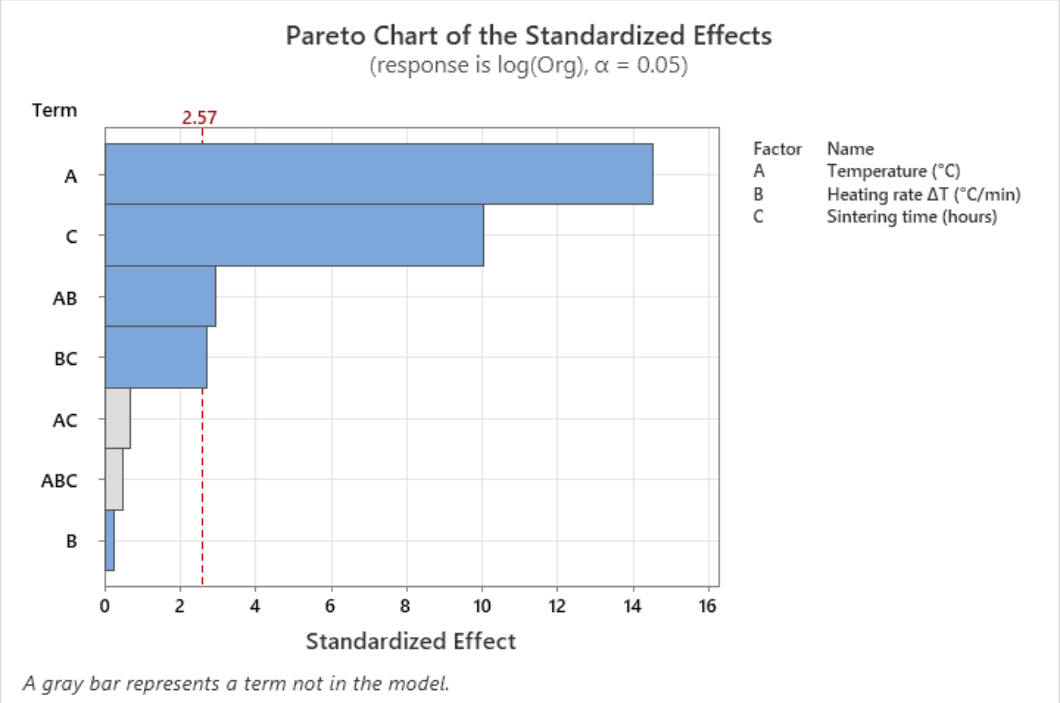

Figure 48 – Pareto chart of the standardised effect for the optimised log(Org) model.

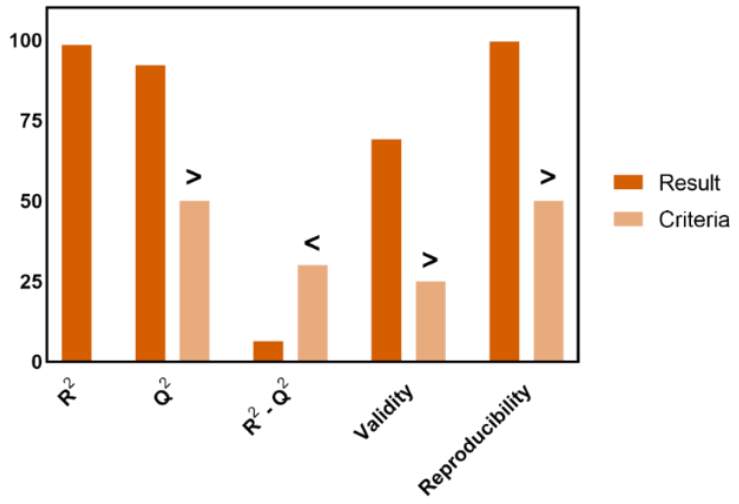

Figure 49 – Summary of Fit for the optimised log(Org) DoE model.

The Effect Plots present in Figure 50 give a clearer idea of how each factor and interaction present in the optimised model affects log(Org). As expected, and in accordance with the Pareto chart (Figure 48), factors A and C have the most profound effect on log(Org), with the response being at its lowest when both are set to their maximum values. It is also possible to see that the AB interaction is at its lowest when both factors are set either at their maximum or minimum values and that BC is at its lowest when C is set at its maximum value.

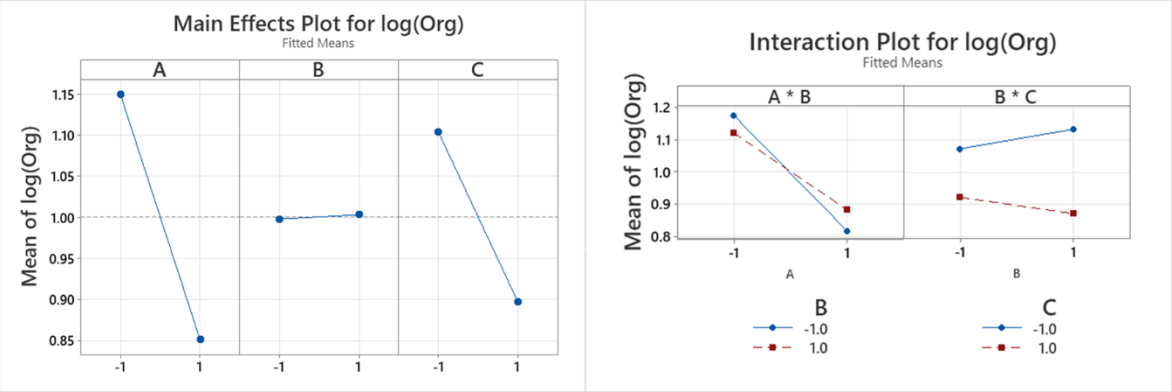

Figure 50 – Effect plots for optimised log(Org) DoE model: a) main effects; b) interaction effects (factor description in Table 20).

Using the response optimiser present in *Minitab 20.0*, it was possible to determine which set of conditions minimise log(Org) and, consequently, Org, according to the obtained model. The lowest values for log(Org) are then obtained when A and C are set at their maximum values (250°C and 6 hours, respectively), and B is set at its minimum (4°C/min). These conditions result in log(Org) = 0.7425, which in turn corresponds to a theoretical Org of 5.53%. This value is close to the one measured during run 6, which follows the optimal conditions and resulted in an Org value of 5.51% (see Table 25). However, due to changes in equipment for

consequent experiments (see section 7.3.4), which can change the obtained results, the only sintering condition that was set after this experiment concluded was Temperature, set to 250°C. Both ΔT and Sintering Time were once again explored during the experiments detailed in 7.3.4, while for the experiments detailed in 7.3.2 and 7.3.3, Sintering Time was set to 6 hours and ΔT to 20°C/min. These settings result in a theoretical log(Org) of 0.7525, and, consequently, Org = 5.66% (close to 5.77% measured during run 8).

7.4.2. Drying conditions alter the organic residues contents on TiO_2 samples before sintering

Figure 51 shows the organic residues detected by TGA of samples dried by different methods (see Table 22). While after sintering all methods performed similarly, before sintering method 3 (drying at 50°C in a vacuum oven at 300 mbar) was shown to result in significantly more organic residues than method 1 (50°C controlled directly on a hotplate) and method 2 (50°C, with temperature controlled by measuring the temperature of a beaker with ultrapure water). Because methods 1 and 2 were shown to be more efficient before sintering, method 3 was discarded as the method to use for drying TiO_2 samples.

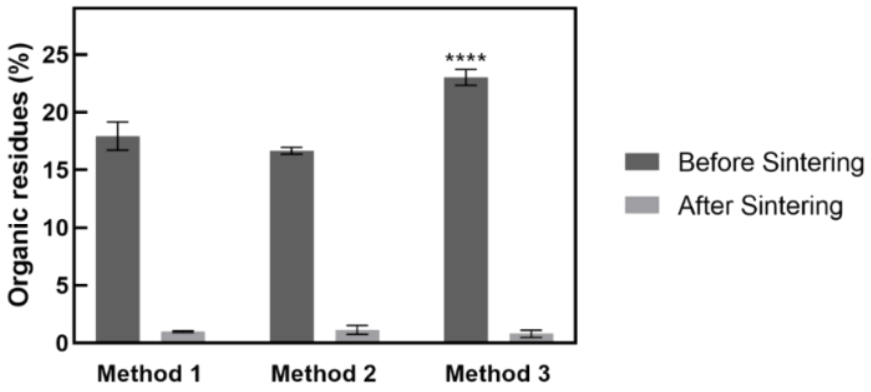

Figure 51 – Organic residues for each TiO_2 drying method (mean + standard deviation, n = 3; **** p < 0.0001).

While methods 1 and 2 performed similarly on average, variability in results pre-sintering was higher in method 1 compared to method 2. Moreover, method 2 could be easily adapted to also control the temperature during synthesis with better precision than method 1. For these reasons, method 2 was chosen as the drying method for all future TiO_2 syntheses.

7.4.3. TiO_2 yield can be improved with the appropriate synthesis conditions

The synthesis method used until now and described in 7.3.1 presented two common problems:

- Only 100 - 300 mg of TiO_2 were generally obtained during synthesis, from a theoretical yield of around 1038 mg (Figure 52-a and Figure 53).
- The synthesis could be unsuccessful, with no TiO_2 precipitating (Figure 52-b).

Due to these common problems, it was decided to study different ways to improve the sol-gel process, as to increase the yield of TiO_2 obtained, as well as to make the process more reproducible. First, the sample labelled “no early precipitation” was left incubating inside a 50 ml falcon tube at room temperature until TiO_2 precipitation was observed. This occurred after 7 days and resulted in a significant increase in TiO_2 yield, as can be observed in Figure 52 and Figure 53. However, 7 days were deemed as too long of an incubation period.

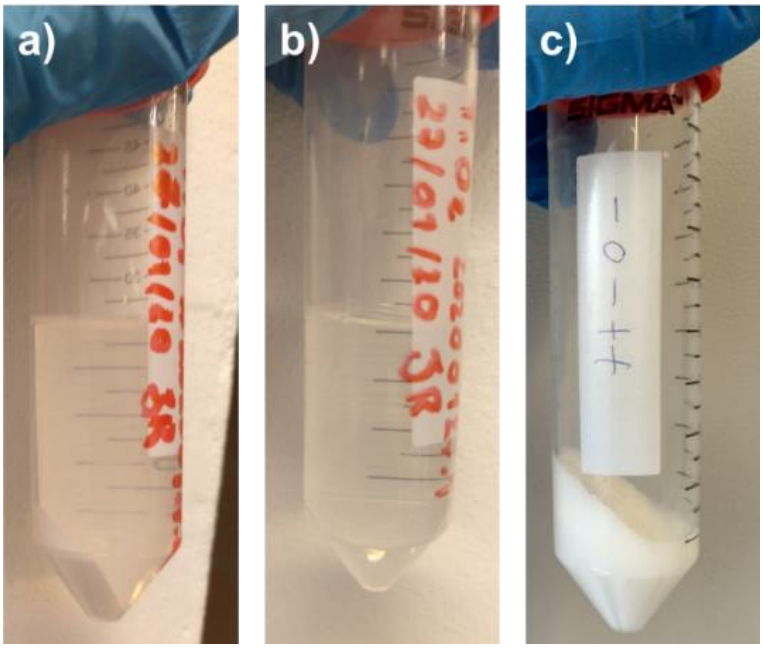

Figure 52 – Comparison between TiO_2 yield after centrifugation: a) early precipitation; b) no early precipitation after 10 minutes incubation period; c) AcOH before H_2O (photo) and no early precipitation after 7 days incubation period.

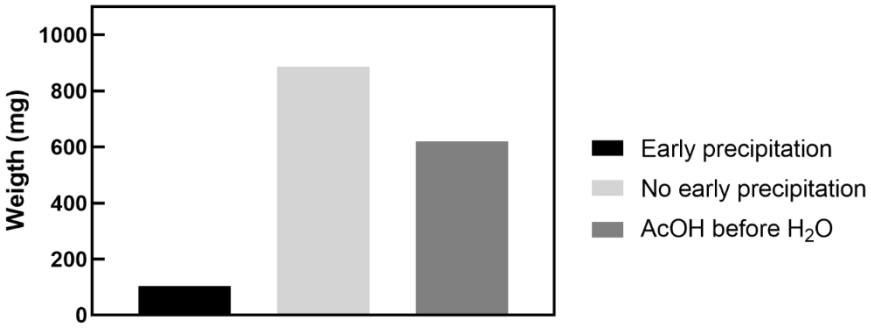

Figure 53 – TiO_2 yield after each synthesis method (n=1).

Adding AcOH before starting hydrolysis and setting the synthesis temperature to 50°C helped solve the long incubation period. First, the addition of AcOH before starting hydrolysis with ultrapure water allowed to reverse any sign of early precipitation due to air humidity. It also prevented the start of the hydrolysis reaction immediately after adding H_2O. These effects, which can be observed in Figure 54, were key for controlling the rate at which the hydrolysis of TTIP to TiO_2 occurred.

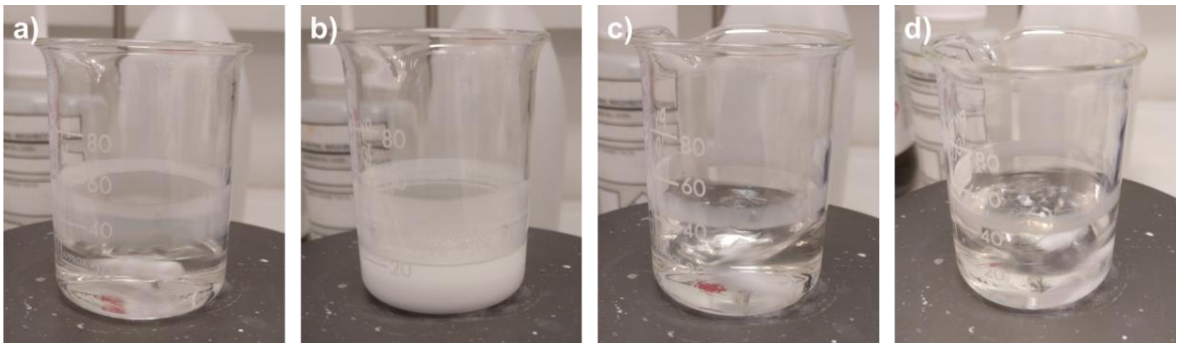

Figure 54 – TiO_2 synthesis with AcOH added before H_2O: a) after adding TTIP; b) 10 minutes after adding TTIP, showing early precipitation of TiO_2 occurred due to air humidity; c) after adding AcOH, which reverses the prior early precipitation of TiO_2; d) after adding H_2O, showing no signs of TiO_2 precipitation.

Second, by heating the solution during the hydrolysis process, it was possible to start precipitating TiO_2 at a faster rate, with the first signs of precipitation occurring 10 minutes after starting the heating process. If covered with punctured aluminium foil, this process could be maintained for 24 hours without full solvent evaporation. Analysing Figure 53, it is possible to see that TiO_2 yield with this synthesis process was still higher than the initial synthesis method, although not as high as leaving the synthesis incubating for 7 days at room temperature. However, it is important to note that the obtained gel from the new synthesis method had to be transferred to a Falcon tube for centrifugation, while the gel obtained from the 7-day incubation formed directly in a Falcon tube and did not need to be transferred for centrifugation. Had both samples been centrifuged following the same conditions, it is possible that both would result in a similar yield. As such, due to the faster synthesis process while keeping high TiO_2 yield levels, it was decided to use the "AcOH before H_2O" synthesis method as the one to use for all future experiments.

7.4.4. The synthesis conditions affect the crystallisation of TiO_2 at 250°C

As was the case in section 7.4.1, the TGA graph for some of the samples showed three weight loss phases corresponding, to water evaporation, degradation of organic residues and crystallisation of TiO_2 to anatase (Figure 55-a). However, as shown in Figure 55-b, other samples did not show a crystallisation phase in their TGA graph. Moreover, samples that showed a crystallisation phase were darker in colour post-analysis, while samples that lacked the crystallisation phase were lighter in colour (Figure 55). These results suggest that some of the obtained samples were already crystallised before being analysed by TGA.

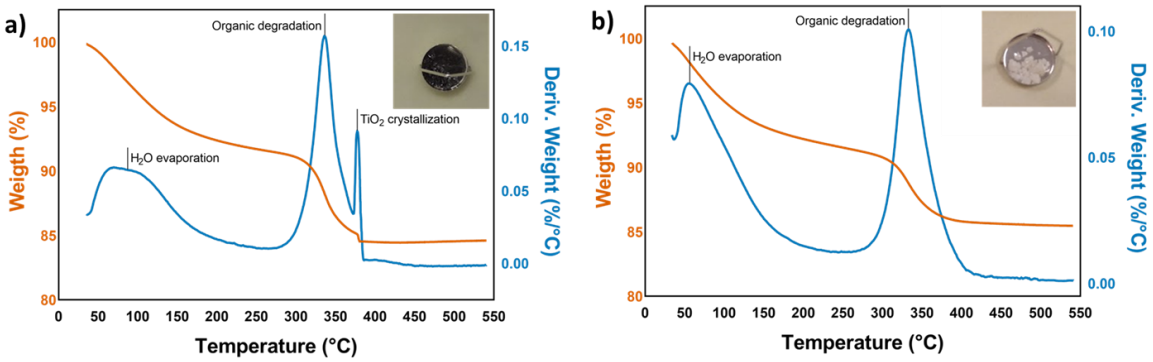

Figure 55 – Example of TGA results, including sample in pan after sintering: a) amorphous TiO_2 (sample 8, standard order); b) crystallised TiO_2 (sample 3, standard order).

XRD analysis allowed confirmation of the previous assumption, with samples categorised into four distinct groups (see standard order in Table 24): amorphous (samples 2, 4, 8, 10 and 11), low crystallinity (sample 6), medium crystallinity (samples 1, 5, 9, 12 and 13) and high crystallinity (samples 3 and 7). Figure 56 compares the XRD graphs of one sample from each group to the standard XRD graph for anatase [139]. Not only were anatase peaks detected in all crystalline samples, but also different samples can have better-defined peaks and, as a result, higher crystallinity. Overall, XRD analysis confirmed that, by tuning the synthesis process, it is possible to obtain crystallised TiO_2 at sintering temperatures of 250°C with different rates of crystallinity.

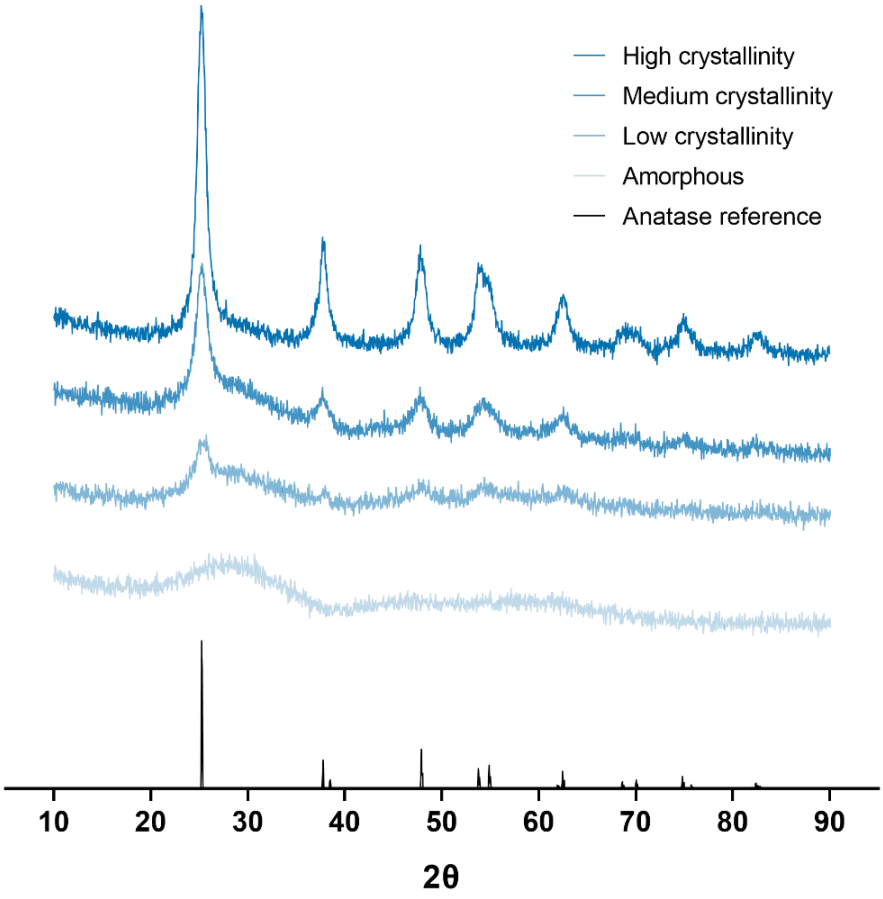

Figure 56 – Examples of XRD results compared to anatase reference (RRUFF ID: R06027): amorphous – sample 8; low crystallinity – sample 6; medium crystallinity – sample 13; high crystallinity – sample 3 (standard order).

7.4.5. DoE allowed to optimise the synthesis of crystallised TiO_2

As in 7.4.1, Org was set as the average weight loss attributed to the degradation of organic residues for each sample, measured by TGA. Likewise, Crystallinity was set as the average crystallinity for each sample, calculated from the XRD analysis. Table 26 summarises the Org and Crystallinity values obtained during each run, and before analysis, it is already possible to observe that both responses

can be affected by the factors in study. Specifically, Org can vary between 7.04% to 13.34%, while Crystallinity can vary between 0.00% (amorphous) and 77.83%.

Table 26 – Low-temperature TiO_2 crystallisation – results (factor description in Table 23)

Standard order	Factor						Org (%)	Crystallinity (%)
	A	B	C	D	E	F		
1	0	+	+	+	+	+	8.10	66.35
2	0	–	–	–	–	–	11.17	0.00
3	+	0	+	–	–	+	7.04	77.83
4	–	0	–	+	+	–	13.34	0.00
5	+	+	0	+	–	–	12.30	60.93
6	–	–	0	–	+	+	12.24	36.91
7	+	–	+	0	+	–	7.71	76.14
8	–	+	–	0	–	+	7.10	0.00
9	+	–	–	+	0	+	7.18	51.59
10	–	+	+	–	0	–	10.92	0.00
11	+	+	–	–	+	0	7.11	0.00
12	–	–	+	+	–	0	9.74	65.97
13	0	0	0	0	0	0	9.35	60.77

Due to the lack of replicate runs in DSD, it does not make sense to show a replicate plot for either Org or Crystallinity. Moreover, as the amorphous samples have null crystallinity, this response cannot be modelled with transformed results. Nevertheless, the histogram for Org% (Figure 57) shows that the obtained results do not follow a normal distribution and, consequently, might need to be transformed. The best transformation was determined using the automatic function from the software *Minitab 20.0*.

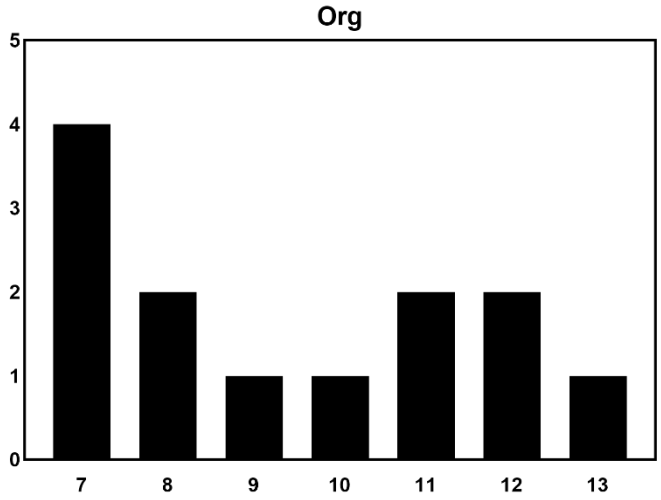

Figure 57 – Histogram of Org.

Equation 20 shows the optimised DoE model for Org, while Figure 58 illustrates the Pareto chart of standardised effects and results for the same model. Despite the results from the histogram analysis, the software found that Org results did not need to be transformed. As it is possible to observe, the only factors that did not seem to affect Org were factors B (ethanol volume) and E (ΔT). Moreover, while factors A and F (reaction temperature and sintering time, respectively) affected the model in a linear fashion, factors C and D (H_2O volume and AcOH volume, respectively) showed signs of curvature, with their quadratic effects being significant to the model. The interaction between factors A and C was also shown to be significant. As presented in Figure 59, the model was able to pass all possible Summary of Fit tests (due to the nature of DSD, it is not possible to calculate validity for this model) and, consequently, can be considered a valid screening model.

Equation 20 – Optimised DoE model for Org (factor description in Table 23)

$$Org\ (\%) = 9.385 - 1.999A - 0.240C + 0.219D - 1.378F - 2.741C^2 + 2.872D^2 + 0.748AC$$

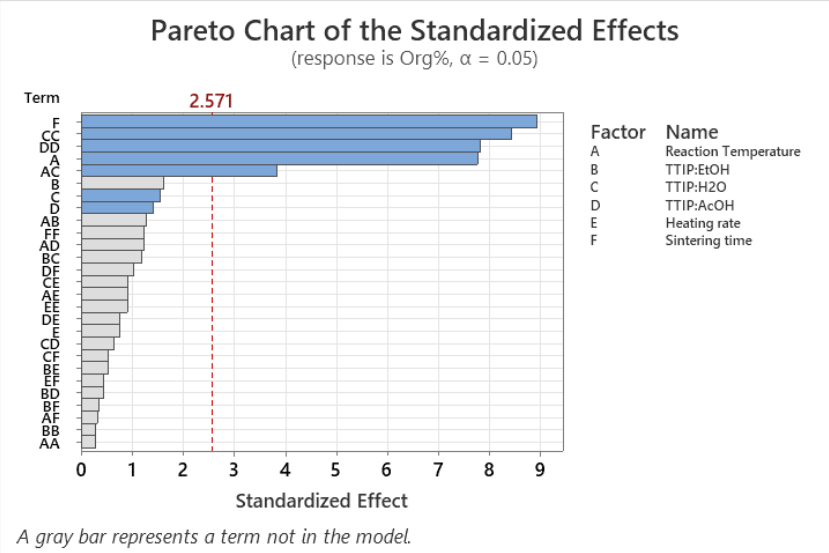

Figure 58 – Pareto chart of the standardised effect for the optimised Org model.

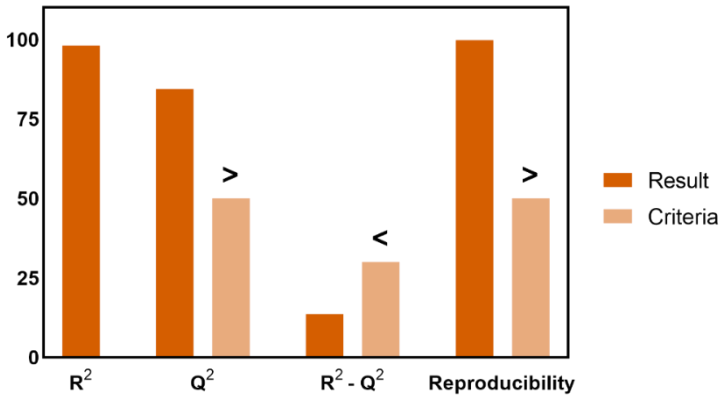

Figure 59 – Summary of Fit for the optimised Org model.

The effect plots from Figure 60 help to visualise how each significant factor affects Org. In the case of factors C and D, it allows to better understand their quadratic effect. In fact, for factor C it is possible to observe a peak where Org is at its highest level, while for D it is possible to observe a valley where Org is at its lowest. Furthermore, it is also possible to observe how the interaction between A and C affects Org, with the lowest value being reached when A is set to 1, and C set to -1.

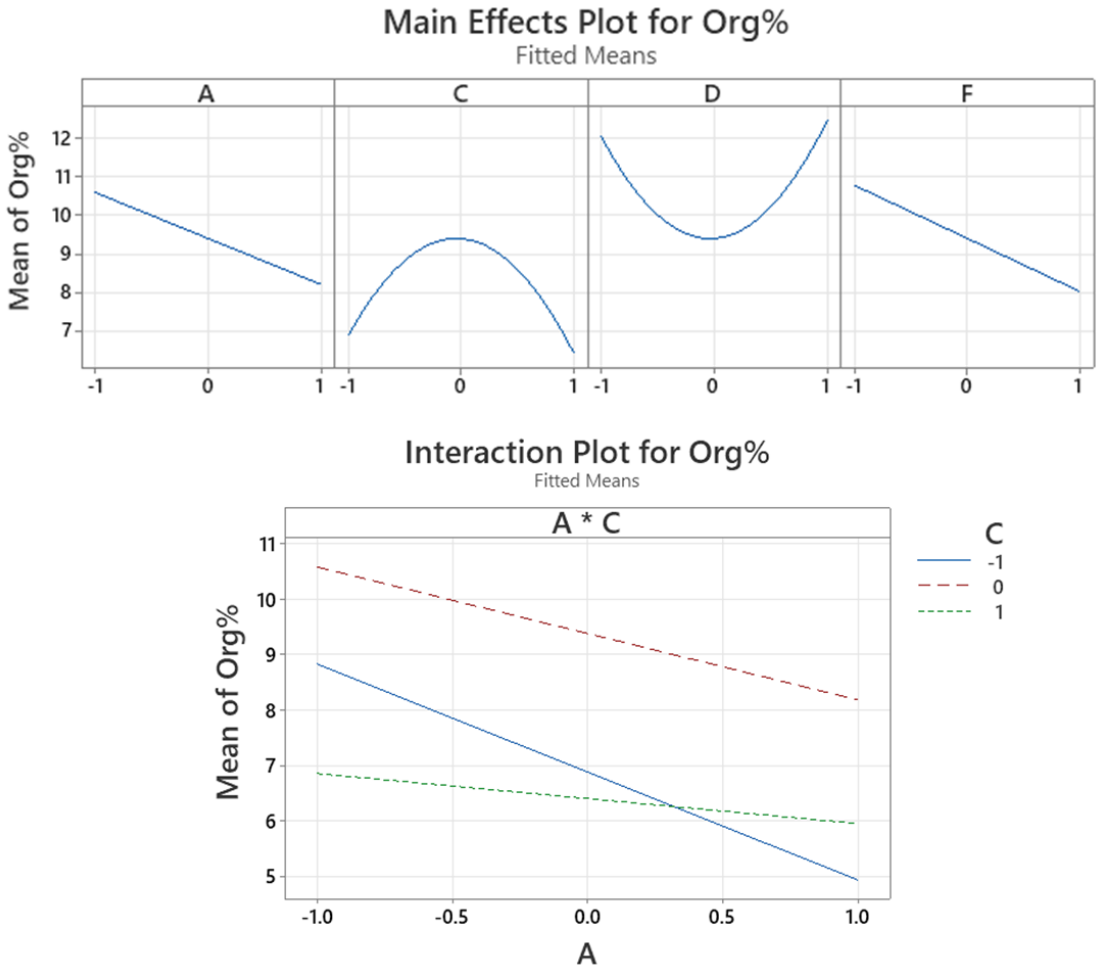

Figure 60 – Effect plots of main effects and interactions for optimised Org DoE model (factor description in Table 23).

Equation 21 and Figure 61 show, respectively, the optimised DoE model for TiO_2 crystallinity and its Pareto chart of standardised effects. Once again, factor E is shown to not significantly affect the modelled response. Moreover, all remaining factors are shown to affect Crystallinity linearly, except for factor C, which is again shown to have a quadratic effect on the model. As shown by Figure 62, the model also passes all possible Summary of Fit tests and, as such, can be considered a valid screening model.

Equation 21 – Optimised DoE model for Crystallinity (factor description in Table 23)

$$Crystallinity = 52.87 + 16.36A - 10.33B + 23.47C + 13.01D + 9.56F - 19.08C^2$$

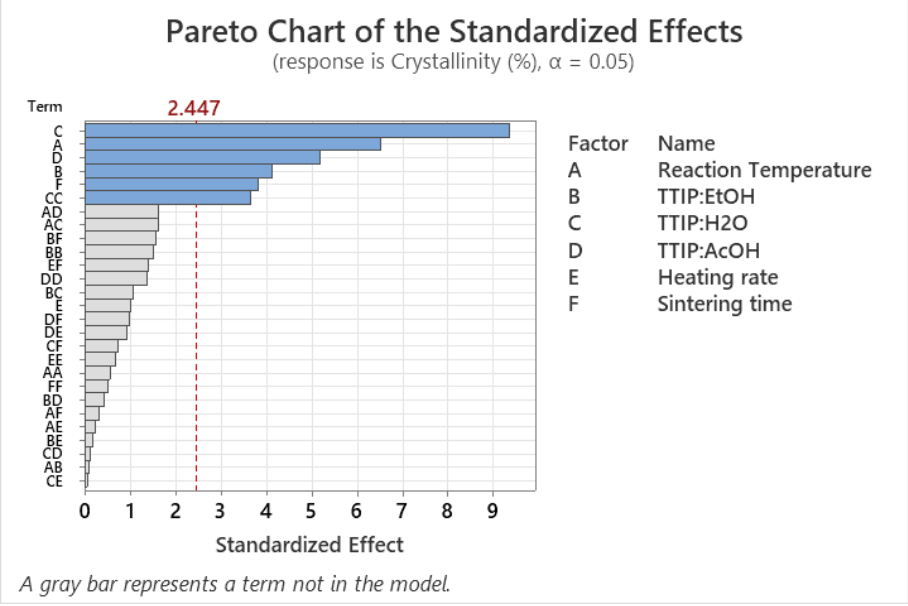

Figure 61 – Pareto chart of the standardised effect for the optimised Crystallinity model.

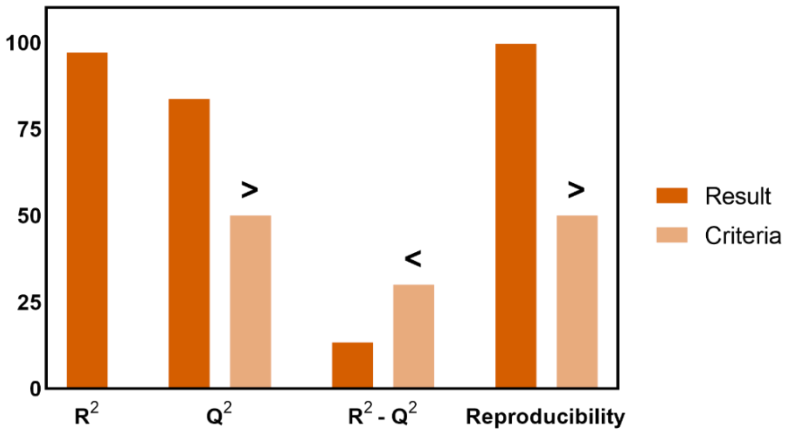

Figure 62 – Summary of Fit for the optimised Crystallinity model.

The effect plots for Crystallinity can be observed in Figure 63. Apart from factor B, all factors with a linear effect are shown to maximise crystallinity when set at their highest value. Moreover, for factor C it is possible to observe that crystallinity reaches its peak when TTIP/H_2O is set to a value between 0 and 1.

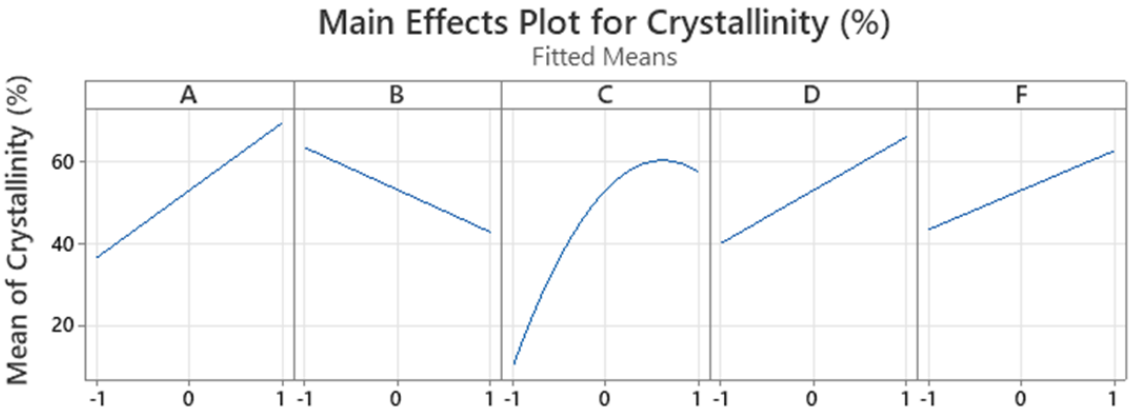

Figure 63 – Effect plots for optimised Crystallinity model (factor description in Table 23).

Using the obtained models and the response optimisation tool from *Minitab 20.0*, it was possible to determine the synthesis conditions that allow to individually minimise Org and maximise Crystallinity. The results can be observed in Table 27 and were used to infer which conditions allow to maximise crystallinity while also keeping Org as low as possible. As the optimal values for factors A (ethanol volume) and F (sintering time) are the same in both cases, the overall optimal synthesis conditions will also have factors A and F set to those same values. Moreover, as factor B is shown to only affect crystallinity, the optimal value for B (EtOH volume) will be the same as the one that allows maximising said response. On the same note, as factor E (ΔT) does not affect any of the possible responses, this factor can be set to the value that is most convenient, in this case, its maximum value (20°C/min).

Table 27 – Optimal synthesis conditions for each modelled response (factor description in Table 23)

Response	Factor					
	A	**B**	**C**	**D**	**E**	**F**
Org	+	N/A	–	-0.03	N/A	+
Crystallinity	+	–	0.62	+	N/A	+

For factors C (H_2O volume) and D (AcOH volume), however, finding the overall optimal synthesis conditions might be slightly more complicated, as the optimal values for each response are not equal. Of the two, factor C is the easiest to optimise. Analysing once again Figure 60, Org was found to reach similar values whenever C is set to either 1 or -1, both independently and when in combination with factor A set to 1. Likewise, by analysing both Table 27 and Figure 63, it is possible to see that, while C should optimally set to 0.62, there is not a large difference in crystallinity when C is set to that value or 1. As such, it can be deduced that the

optimal overall value for factor C that allows for both low Org and high crystallinity is 1.

The same cannot be said about factor D. Analysing once again Figure 60 and Figure 63, it is possible to see that when optimising one of the responses, the other with significantly stray away from its optimal settings. However, in both cases, the overall optimal value for D should be around 0 and 1. Using the prediction function from Minitab 20.0, it was calculated the predicted values of Org and Crystallinity when D is set to different values between 0 and 1, and when all other factors are set at their optimal values. The results can be observed in Table 28. As can be seen, the increase in Org from when D changes from 0 to 0.5 is lower than when D changes from 0.5 to 1. Moreover, the increase in Crystallinity is also higher when D changes from 0 to 0.5, even if the highest crystallinity is indeed reached when it is set to 1. With these results in mind, it can be concluded that the optimal synthesis condition set factor D to 0.5 and, consequently, the overall best TiO2 synthesis conditions can be considered those from Table 29.

Table 28 – Org and Crystallinity when factor D is set at different values (A=1, B=-1, C=1, F=1)

Factor D	Org (%)	Crystallinity (%)
0	3.56	93.51
0.5	4.39 (+23.31%)	100.02 (+6.96%)
1	6.65 (+51.48%)	106.52 (+5.99%)

Table 29 – Optimal TiO_2 synthesis conditions (factor description in Table 23)

Value	Factor					
	A	**B**	**C**	**D**	**E**	**F**
Model	+	–	+	0.5	+	+
Real	70°C	15 ml	3 ml	3.25 ml	20°C/min	6 hours

Figure 64 compares the TGA and XRD results obtained by analysing a TiO2 sample synthesised following the conditions from Table 29, and those obtained following run 3 from Table 26, which resulted in the DoE sample with the lowest Org and highest Crystallinity. As it is possible to see, the sample following the optimal conditions was shown to have lower Org (5.52%) and higher Crystallinity (79.97%) than run 3 (7.04 and 77.83%, respectively), confirming that the conditions from Table 29 are indeed able to simultaneously minimise Org and maximise Crystallinity and can, consequently, be considered as optimal for the synthesis of crystallised TiO2 sintered at 250 °C.

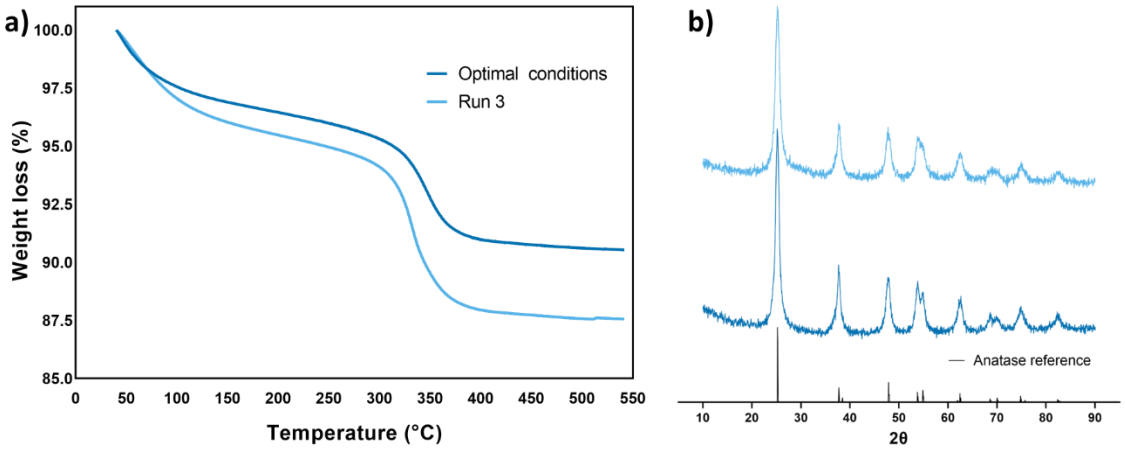

Figure 64 – Comparison between run 3 and TiO_2 synthesised following optimal synthesis conditions: a) TGA; b) XRD (anatase reference: RRUFF ID – R060277.9).

7.5. Discussion

This chapter studied the ability to crystallise TiO_2 synthesised through sol-gel chemistry at low sintering temperatures. While there have been studies showing the benefits on the osteointegration of orthopaedic implants with crystallised TiO_2 [57,

58], including coatings produced through sol-gel, these have always been conducted on metallic or ceramic substrates [132, 140, 141], which are able to sustain the temperatures required to crystallise TiO_2, traditionally between 400 to 500°C to obtain anatase crystals [59, 60]. On polymeric substrates such as PEEK, studies seem to either focus on amorphous TiO_2 sol-gel coatings [133, 142, 143] or on other coating techniques which use pre-crystallised TiO_2 [133, 135-138]. Nevertheless, the ability to lower the crystallisation temperature of TiO_2 has been studied for other non-biomedical applications, and this work aimed to translate those solutions to the medical field [72-75].

The initial protocol for synthesising TiO_2 through sol-gel was derived from different protocols found in the literature [70, 71, 73, 74, 144]. Titanium isopropoxide or TTIP was chosen as the TiO_2 precursor mainly for two reasons. First, alongside titanium butoxide, TTIP is one of the better-studied precursors for the sol-gel synthesis of TiO_2. Second, compared to titanium butoxide, the hydrolysis of TTIP to TiO_2 releases isopropanol as a byproduct, as seen in the chemical reaction detailed in Equation 22. For that same reason, isopropanol was initially planned as a solvent for this research, as it would minimise the number of organic compounds that need to be removed after synthesis to two (isopropanol and AcOH), compared to three when using EtOH (isopropanol, EtOH and AcOH). However, it was not possible to use isopropanol as a solvent due to permit issues from the project's industrial partner. Nevertheless, different studies suggest that crystallinity might be higher in samples prepared in EtOH, when compared to isopropanol, explaining why EtOH was chosen as the solvent for the present study [145-147].

Equation 22 – Hydrolysis of Titanium Isopropoxide to Titanium Dioxide

$$Ti\{OCH(CH_3)_2\}_4 + 2H_2O \rightarrow TiO_2 + 4(CH_3)_2CHOH$$

The proportions of reagents are also based on previous research, as well as on the reaction detailed in Equation 22. As TTIP has a molar mass of 284.219 g/mol and a density of 0.96 g/ml, and considering that 1 mol of TTIP originates 1 mol of TiO_2 (molar mass of 79.866 g/mol), the 3.9 ml of TTIP used during synthesis results in approximately 1 gram of TiO_2 (specifically, 1.038 g). Moreover, that same volume of TTIP indicates that approximately 0.9 ml of H_2O (molar mass of 18.015 g/mol, density of 0.997 g/ml) is the volume necessary to have a TTIP/H_2O molar ratio of 1 to 4, which is double of mols of H_2O necessary to fully hydrolyse all TTIP. This guarantees that all TTIP is hydrolysed during synthesis. As for solvent, 19.0 ml of EtOH (molar mass of 46.069 g/mol, density of 0.789 g/ml) results in a TTIP/EtOH molar ratio of 1 to 25, which is around the average TTIP/solvent ratio used during different studies [70, 71, 73, 74, 144]. Finally, AcOH was chosen as a peptising agent for two reasons. First, alongside HCl and HNO_3, it is one of the better-studied reagents used for this purpose [70, 71, 73, 74, 144]. Second, and most importantly, AcOH is much safer to use in its pure state compared to the aforementioned alternatives. This is important, as these acids are generally stored in aqueous solutions for safety, and TTIP is very reactive to water. This is the same reason why anhydrous EtOH is used as a solvent.

Because the presence of organic residues might impact the biocompatibility of TiO_2, the first objective of this research was to quantify these residues in the samples produced. This is the main reason why TGA was predominant during the study, as it helps quantify Org present in each sample. Ideally, Org should be lower than 1%, as those values can be attributed to the release of adsorbed CO_2, and the TiO_2 samples can be considered as free of organic impurities [148]. As expected, Org was minimised with higher reaction and sintering temperatures, and with longer sintering times. Interestingly, while a low heating rate during sintering is preferable, its individual effect is negligible. The DoE detailed in 7.3.4 also reveals some interesting results, mainly the quadratic effects of the volumes of H_2O and AcOH used, and the interactive effect between H_2O and reaction temperature on Org, as well as the lack of an effect from the EtOH volume used during TiO_2 synthesis. As

they might be explained by the nature of the residues detected, as well as on the sample's crystallinity, these results will be explained later in the discussion (page 163).

It is important to notice that in none of the samples synthesised during each DoE resulted in ideal Org values (Org ≤ 1%). For this reason, identifying the nature of the organic residues present in the samples is of great importance, both to better assess its possible effect on the biocompatibility of the synthesised TiO_2, as well as to decide the best post-treatment necessary to remove those impurities from the samples. This is one of the main reasons why DSC was performed alongside TGA analysis: it is able to detect different temperature-induced phenomena, including the evaporation of desorption of different chemical compounds, which can be used for their identification. In this case, the lack of peaks around 78.0°C, 82.6°C, 117.9°C and 232°C suggest that the detected residues do not come from remaining EtOH, isopropanol, AcOH and TTIP, as those are their respective evaporation temperatures. The lack of an EtOH-related peak can explain why it did not influence Org during the second DoE: as all EtOH had evaporated after drying and sintering, none remained to affect Org for each sample.

There was, however, a peak detected at around 350°C for all samples (see Figure 55), which literature attributes to acetate groups adsorbed at the surface of the TiO_2 samples [149, 150]. The presence of these groups can be attributed to the AcOH used during synthesis. Despite most AcOH being evaporated during the drying and sintering processes, some is adsorbed into the samples, and can only be thermally desorbed at temperatures higher than the sintering temperatures in study [149, 150]. What is interesting is that, as can be observed in Figure 60, until it reached its DoE 0 value, Org decreases with the increase of AcOH. Furthermore, one interesting caveat from identifying acetate groups as the source of Org is that one can use UV light or gamma radiation to activate TiO_2's photocatalyst behaviour to degrade the adsorbed groups and, as such, clean itself during sterilisation with those agents [151, 152]. Both UV light and gamma radiation are extensively used for

sterilisation processes [153], and TiO_2 has been shown to degrade adsorbed acetic acid when exposed to both sources of radiation [154].

The drying method also shows an effect on Org. Comparing even the optimal results from the first DoE, which had the samples drying while covered with parafilm, and the drying methods detailed in Table 22 (page 134), where all samples were dried uncovered, there was a substantial decrease in Org detected after sintering when the samples were left to dry uncovered. It is possible that uncovering the samples facilitated the evaporation of AcOH, diminishing its chances of adsorbing into the TiO_2. What is curious is that the methods detailed in 7.3.2 only show differences between their respective results before sintering and that the worst-performing method at this stage was drying under a vacuum. It was expected that this method would have performed the best, as the vacuum was used to remove evaporating compounds. While it is possible that the vacuum was not strong enough for this purpose, it might also be possible that drying in the hotplate allows for better heat transfer through the TiO_2 samples and, as such, enhance the evaporation of organic compounds. While on average both hotplate-based methods performed similarly, the more precise temperature control from method 2 seemingly resulted in less variable results before sintering. For this reason, as well as it being a method that could be explored both for the synthesis and drying processes, method 2 was chosen as the drying process for the remaining experimental work.

Regardless of drying method, all seemed to reach the desired Org value of around 1% after sintering during the experiments detailed in 7.3.2. However, that stopped being the case when analysing the second DoE. It is suspected these results came from the changes to the synthesis protocol derived from the experiments detailed in 7.3.3. The addition of AcOH before starting the hydrolysis of TTIP, the peptising effect AcOH has during the synthesis process and the increase of the synthesis duration from 10 minutes to 24 hours all might have contributed towards facilitating the adsorption of the organic compound and, consequently, increase Org to levels higher than 1%. However, these changes were necessary to

make the synthesis process much more reproducible, as well as to improve TiO_2 yield after drying. Moreover, as previously stated, while AcOH could be substituted for other acids such as HCl or HNO_3, because the peptising agent should be used undiluted due to TTIP's reactivity with water, the use of the alternatives would substantially increase the safety risks of the synthesis process. The peptising effect of AcOH is important for the crystallisation of TiO_2, as it has been proven by different publications [74, 155], as well as this current work. AcOH acts as a chelating agent able to control the hydrolysis reaction, being able to even revert the hydrolysis process derived from TTIP reacting with humidity from the experimental environment (see Figure 54). However, the chelating process also slows the reaction considerably when performed at room temperature, as it can take up to 7 days for the reaction to complete. Nevertheless, if energy is supplied to the synthesis process by running it at temperatures as high as 50°C, the hydrolysis process can be completed at much faster rates. Combining both the peptising agent and temperature allows for a more controlled synthesis process at faster rates. Covering the reaction also allows the synthesis to run for longer periods without fully evaporating, while in turn providing more energy to TiO_2 which helps with its crystallisation.

While TGA and DSC were mainly used to study Org, they were also useful as indicators of the crystalline nature of the sintered TiO_2 samples. The crystallisation of TiO_2 to anatase can be detected as a sudden decrease in sample weight during TGA at around 400°C, as well as an endothermic peak around the same temperature during DSC. Detecting these phenomena is an indication that the TiO_2 sample is crystallising to anatase during TGA and DSC, and as such was in an amorphous stage before analysis. However, as shown in Figure 55, some samples did not show this decrease in weight at 400°C attributed to the crystallisation of TiO_2. TGA and DSC in these cases indicate that the TiO_2 sample was already crystallised before analysis: as the sample was already in a crystalline state, it will not crystallise again. These suspicions were shown to be correct after XRD analysis: the samples which did not crystallise during TGA showed the characteristic peaks for anatase, while the samples which crystallised during TGA were shown to be amorphous during XRD.

Even before creating the DoE model, these results already indicate that this chapter's objective was successful and it was possible to decrease the crystallisation temperature of TiO_2 from around 400°C to 250°C and, consequently, a crystallised TiO_2-based coating can be potentially achieved at temperatures that PEEK can withstand without degrading or melting.

Before DoE analysis, two factors were suspected to have a significant effect on TiO_2 crystallisation at 250°C: synthesis temperature and AcOH volume. Due to the endothermic nature of the crystallisation process, providing the system with more energy by increasing the synthesis temperature should promote the formation of anatase. This effect has already been shown in different works, both by utilising heat sources and microwaves [73, 74]. Furthermore, the peptising effect of AcOH, which has also been shown to promote crystallisation, might enhance the crystallisation process by controlling the hydrolysis process in a more organised fashion, facilitating the formation of crystalline structures [74, 156, 157]. It was also of interest to see if the volume of H_2O used to initiate hydrolysis influences crystallinity, as it has been shown to affect the obtained crystal structures in previous studies [158, 159]. Other factors that were deemed interesting to study were the volume of EtOH used and sintering time, as they could both influence the energy in the form of heat being supplied to the system (see Equation 23, considering the TiO_2 gel a solid material, and the distance between surfaces increasing when increasing the volume of EtOH), and the heating rate during sintering, as slower heating rates could help to control the crystallisation process.

Equation 23 – Heat transfer through conduction

$$Q = \frac{kA(T_{Hot} - T_{Cold})}{d} \cdot t$$

Q = *heat (J)*
k = *thermal conductivity (J/msK)*
A = *surface area (m^2)*
T = *temperature (K)*
d = *distance between surfaces (m)*
t = *time (s)*

The optimised DoE model, presented in Equation 21 (page 152), shows that, besides heating rate, all factors in this study did indeed affect crystallinity, in accordance with what has been shown in previous works. Specifically, crystallinity is at its highest when synthesis temperature, AcOH volume and sintering time are at their highest levels, and when EtOH volume is at its lowest. Once again, these results prove the importance of the peptising effect of AcOH in crystal formation, and the importance of the energy in the form of heat provided during synthesis and sintering for the formation of anatase crystals which, as a reminder, is an endothermic process.

More interesting is the quadratic behaviour attributed to the TTIP:H_2O ratio. As previously mentioned, the volume used to induce hydrolysis has been shown to affect both the crystallinity and crystal structures obtained after sintering TiO_2 [158, 159]. What these previous works seem to have missed, perhaps due to their focus on higher sintering temperatures than 250°C, is crystallinity increases significantly when changing the TTIP/H_2O ratio from 1/4 to 1/8. This increase in crystallinity seems to then stabilise when increasing the ratio further to 1/12, as it is observed in the effect plot from Figure 63. Because the difference in crystallinity when the ratio is at 1/8, 1/12 and when it is at its optimal value is not very high, it is even possible that crystallisation reaches a plateau within this region. What is interesting is that the point where this possible plateau is reached corresponds to the point where Org starts decreasing due to the water volume (compare Figure 60 to Figure 63). It is possible that this decrease in Org might relate to the sample reaching its maximum crystallinity, as the state of TiO_2 samples after TGA suggest that it is easier to remove organic residues from crystalline samples (compare the colour of amorphous and crystallised TiO_2 in Figure 55, with crystallised TiO_2 being white after TGA).

Similar reasoning might explain how Org changes due to AcOH levels: because crystallinity increases linearly with AcOH, Org values initially decreases with AcOH levels. But because AcOH is the source of organic residues present in the samples, the growth in crystallinity might become insufficient to combat the

adsorption of acetate groups and Org starts increasing once again. This explains why it was important to optimise the sol-gel process not just for TiO_2 crystallinity, but for Org as well: even if an effective cleaning method is found, it is important to have as fewer organic residues as possible to facilitate the cleaning process.

The optimisation process was for the most part straightforward. Regarding synthesis temperature and sintering time, the same conditions that minimise Org also increase crystallinity. Furthermore, because the volume of EtOH does not impact Org, said factor can be set to the level that optimises crystallinity, and because it does not affect either response, heating rate can be set at the most suitable condition, in this case at its highest level. The H_2O level was also relatively simple to optimise, as Org is similarly low when using 1 ml or 3 ml and crystallinity either reaches a plateau at 2 ml or there is no significant difference between using 3 ml or using the actual optimal volume. It was, however, necessary to optimise the AcOH levels since both optimal responses seem to be at odds with one another. In the end, it was decided that the best solution was to set AcOH at 0.5 (3.25 ml), as the increase in Org, calculated using the model from Equation 20, was lower from 0 to 0.5 than from 0.5 to 1, while the increase in crystallinity between the same levels, calculated using the model from Equation 21, was of similar magnitudes.

It is important to state that the models used to optimise both conditions were screening models. As such, while they are useful to understand which are the conditions that result in optimal results, they cannot be used to predict said results. A good example are the crystallinity levels calculated to optimise AcOH (see Table 28): two of the values measured were above 100%, which should be impossible. Nevertheless, TiO_2 samples synthesised following the theoretical conditions still showed an increase in crystallinity and a decrease in Org when compared to the sample prepared for run 3, which was the DoE sample with the best overall results (see Table 26 and Figure 64). These results demonstrate that both responses were indeed optimised using the obtained DoE models, even if they were not able to predict the actual optimal values.

7.6. Summary

In this work, a sol-gel protocol that can be used to synthesise TiO_2 capable of crystallising into anatase at a sintering temperature of 250°C was successfully developed. Moreover, DoE was successfully used to obtain mathematical models that allowed optimisation of the synthesis conditions to maximise TiO_2 crystallinity and minimise organic residues still present after sintering. The optimal synthesis conditions were found to be when synthesis temperature is set at 70°C, 15.00 ml of EtOH are used as solvent, 3.25 ml of AcOH as a peptising agent, 3.00 ml of H_2O is used to start hydrolysis and when the sintering process occurs at 250°C for 6 hours. These conditions result in TiO_2 with crystallinity around 79.97% and 5.52% of organic residues in weight. Heating rate was found to not influence the optimal synthesis process, despite being important in reducing organic residues when the sintering temperature is lowered to 200°C. The optimal conditions obtained will be used as the basis for the sol-gel coatings to be developed during Chapter VIII.

VIII. Development of composite TiO_2/hydroxyapatite coatings for spinal fusion cages

8.1. Introduction

One of the main issues that can cause the failure of spine fusion surgery is the failure of proper integration of the spinal fusion cage with the adjacent vertebra [9, 13]. This issue is particularly prevalent in cages based on polyether ether ketone (PEEK), as it is a bioinert material and, as such, does not promote bone growth at its surface. However, PEEK has some advantages compared to Ti-6Al-4K as a material for fusion cages, namely its mechanical properties which are closer to those of cortical bone [10, 11, 27]. Nevertheless, it is possible to enhance the osteointegration of cages made of both Ti-6Al-4V and PEEK by coating them with an osteoinductive material [10, 11, 14].

One interesting material to explore is hydroxyapatite (HAP), as it is the basis of bone mineral and is able to induce, when in contact, the osteogenic differentiation of mesenchymal stem cells (MSCs) and, as such, bone growth and regeneration [109, 110]. HAP-based coatings have been successfully used for other orthopaedic applications [39, 51], however, the coating technique used for those, plasma spraying, is not adequate for polymer-based implants due to the high temperatures it requires and presents several drawbacks in terms of phase purity and mechanical performance [39-41]. Furthermore, HAP coatings tend to adhere poorly to substrates, compared to other materials [69, 70].

Another material of interest is titanium dioxide (TiO_2). This oxide was found to be responsible for the biological performance of Ti-based implants, occurring naturally at the surface of those materials, protecting them from corrosion and wear, and introducing an osteoinductive effect of its own [26, 54, 55]. That osteoinductive effect of TiO_2 can be further enhanced when present in one of its crystalline forms [57-60]. Furthermore, TiO_2 can be easily synthesised by sol-gel chemistry, a

technique able to synthesise high-quality ceramic coatings in a simple and cost-effective way [40, 63, 130].

Composite TiO_2/HAP coatings have been synthesised in the past, to combine the benefits of both materials into one coating [66, 69-71]. However, no studies have been found that combine HAP with crystalline TiO_2 on polymeric substrates such as PEEK, while simultaneously retaining the advantages of sol-gel dip coating. With that in mind, this chapter aims to develop a composite crystalline TiO_2/HAP coating based on sol-gel chemistry which can be used on both Ti-6Al-4V and PEEK substrates.

8.2. Aims and Objectives

The aim of this chapter was to use DoE to find the optimal conditions that will result in composite TiO_2/sHAP coatings with optimised osteogenic potential. The coatings will be developed with commercially available Mg-enriched HAP [49], and TiO_2 synthesised using the optimal conditions from Chapter VII. To achieve the aim, the following objectives were addressed:

I. Pre-screening coating conditions, including maximum sHAP quantity, drying conditions, and substrate air plasma pre-treatment that still allow for a stable coating to be formed.
II. Assess using DoE what conditions allow maximal coating adherence to a substrate and maximal biological performance.
III. Use the obtained DoE models to determine conditions that result in highly adherent coatings with optimal biological performance. Test said conditions both with commercial sHAP and the optimal formulation from Chapter V.

8.3. Materials and Methods

The following Materials and Methods are specific to this chapter. For general details please refer to Chapter IV.

8.3.1. Preliminary coating conditions

Two sets of glass substrates were coated as stated in 4.2.15, albeit manually. The substrates were submitted to air plasma pre-treatment for 1 minute with 50% power (50 W) for all conditions. The first set was coated using a pure TiO_2 suspension, which was synthesised following the conditions set in run 9 (standard order) presented in Table 24 from Chapter VII. However, contrary to the instructions from 4.2.15, this set was washed before the sintering process. This set followed conditions A to D, as described in Table 30. The water contact angle (WCA) of the coated substrates, as well as uncoated glass, was measured by manually dropping three 5 µl drops of ultrapure water using a 20 µl micropipette, photographing the profile of the drops, and measuring the angle of both sides of each drop using the software *ImageJ*. WCA was measured for samples before and after sintering and considered as the average value of all measurements for each condition.

Table 30 – Preliminary coating conditions

Condition	Layers (unit)	Coating Time (min)
A	1	1
B	3	1
C	1	5
D	3	5
E	1	3
F	3	3

The second set was coated in similar conditions as set 1, albeit using a TiO_2/HAP suspension (1/1 ratio in weight, considering a theoretical TiO_2 weight of 1.038 g). Mg-enriched HAP was used. For this set, samples were coated following all conditions set in Table 30. WCA was also measured as stated above, although for conditions E and F WCA was measured only after sintering.

8.3.2. Pre-screening air plasma pre-treatment in Ti-6Al-4V and PEEK substrates

The air plasma pre-treatment of the Ti-6Al-4V and PEEK substrates was studied in two phases. In the first phase, Ti-6Al-4V substrates were cut to have a diameter of 1.5 cm (see 4.2.13) and were treated as stated in 4.2.14 following the conditions present in Table 31. For each condition, WCA was measured as stated in 8.3.1 at different time points (0 min, 1 min, 5 min, 10 min, 30 min, 60 min). WCA at each time point was measured in a different sample, with all samples being covered in aluminium foil until their specific collection time.

Table 31 – Preliminary air-plasma conditions

Condition	Power (%)	Time (sec)
A	50	60
B	100	60
C	50	120
D	100	120

The second phase involved the study of the pre-treatment in PEEK substrates. The tests were conducted similarly to the second phase, but only following condition D from Table 31, and a new condition, labelled E, with power set

at 100% (100 W) and time to 300 seconds. Timepoints were also reduced to four (0 min, 10 min, 30 min, 60 min).

8.3.3. Preliminary *in vitro* testing conditions

For the preliminary *in vitro* study, different Ti-6Al-4V substrates with 1.5 cm diameter were prepared, in the following manner:

- Three substrates coated with pure TiO_2
- Three substrates coated with pure TiO_2 and treated under UV light
- One substrate coated with TiO_2/HAP composite
- One substrate coated with TiO_2/HAP composite and treated under UV light
- Two uncoated substrates

Before coating, all substrates were cut and pre-treated as stated in 4.2.13 and 4.2.14 respectively, with the air plasma pre-treatment running for 5 minutes at 100% power (100 W). The suspensions prepared in 8.3.1 were used to coat the prepared substrates. The UV treated samples were immersed in 5 ml of ultrapure water in a 35 mm open petri dish, and exposed to UV light for 90 minutes, changing the water every 30 minutes. All samples were sterilised by immersing in 25 ml of 70% ethanol in a 50 ml Falcon tube for 2 days.

hTERT-MSCs Y201 cells, passage 78 [83] were seeded as stated in 4.2.19 for 7 days in all substrates besides one uncoated substrate, used as a blank. The cells were cultured in serum and xeno-free media (StemMACS™ MSC Expansion Media Kit XF, human, Miltenyi Biotec). On day 7, metabolic activity was measured using a resazurin reduction assay, as stated in 4.2.5.

8.3.4. Development of osteogenic TiO_2/sHAP sol-gel coatings – DoE approach

The development of TiO_2/sHAP coatings was studied using a definitive screening design (DSD). Table 32 describes the factors and conditions studied, while Table 33 summarises the experimental design.

Table 32 – Development of TiO_2/sHAP coatings: Factor description

Factor	Description	–	0	+
A	Substrate	Ti6Al4V	n/a	PEEK
B	TiO_2/sHAP (w:w) sHAP weight (mg)	1:0 (0.0 mg)	1:0.75 (778.7mg)	1:1.5 (1557.5mg)
C	Layers (unit)	1	3	5
D	Dip time (min)	1	3	5
E	Robot timing (ms)	10	20	30
F	Heating rate ΔT (°C/min)	4	12	20

Table 33 – Development of TiO2/sHAP coatings: Design summary

Standard order	Run Order	Factor					
		A	**B**	**C**	**D**	**E**	**F**
1	11	–	+	+	+	+	+
2	2	+	–	–	–	–	–
3	13	+	0	+	–	–	+
4	8	–	0	–	+	+	–
5	12	+	+	0	+	–	–
6	3	–	–	0	–	+	+
7	4	+	–	+	0	+	–
8	1	–	+	–	0	–	+
9	9	+	–	–	+	0	+
10	5	–	+	+	–	0	–
11	7	+	+	–	–	+	0
12	14	–	–	+	+	–	0
13	6	–	0	0	0	0	0
14	10	+	0	0	0	0	0

Three sol-gel suspensions, following the TiO_2/sHAP ratios detailed in Table 32, were prepared as stated in 4.2.15 following the optimal TiO_2 synthesis conditions defined in Chapter VII, albeit using 20 ml of ethanol. The Ti-6Al-4V and PEEK substrates used had a diameter of 7.5 mm and were cut and pre-treated as stated in 4.2.13 and 4.2.14 respectively, with an air plasma pre-treatment set to 5 minutes at 100% power (100 W). The substrates were coated following the protocol described in 4.2.15, and the conditions and run order set by Table 33. For each condition, 4 samples were prepared. All samples were sterilised in 25 ml 70% ethanol in a 50 ml Falcon tube for 2 days. Alongside the coated samples, four uncoated samples of both Ti-6Al-4V and PEEK were also sterilised under the same conditions.

For each condition and uncoated substrates, hTERT-MSCs Y201 cells, passage 78 were seeded as stated in 4.2.19 in 3 of the prepared substrates, with the remaining sample used as a blank. The Ti-6Al-4V substrates were placed in 48 well-plates, while the PEEK substrates were placed in 24-well plates. Alongside all substrates, Y201 cells were also cultured directly in a 48-well plate, both in expansion and osteogenic media, to serve as positive and negative controls. All cells were cultured in serum and xeno-free media (StemMACS™ MSC Expansion Media Kit XF, human, Miltenyi Biotec) for up to 14 days. As DoE response the DNA-adjusted ALP was used, measured at day 14 as stated in 4.2.6.3. Metabolic activity by resazurin reduction assay was also measured on day 7 and day 14 as described in 4.2.5.

8.3.5. Measuring roughness and thickness of optimised coatings

Substrates of both Ti-6Al-4V and PEEK with a diameter of 1.5 cm were cut and pre-treated as described in 4.2.13 and 4.2.14 respectively, with air plasma set to run for 5 minutes at 100% power (100W). The samples were then coated as stated

in 4.2.15, following the optimal conditions defined by the DoE detailed in 8.3.4 and with either Mg-enriched HAP or the HAP C6- developed during the experiments detailed in Chapter VI. Before coating, half of the substrates' surface was covered with adhesive tape, to only coat half of the sample. The tape was removed before the sintering process. The prepared samples, as well as uncoated Ti-6Al-4V and PEEK substrates, were analysed with profilometry (Contour Elite X, Bruker), measuring different area roughness parameters and the thickness (20x magnification) of each coating.

8.4. Results

8.4.1. Coating glass substrates alter their original WCA

Figure 65 shows the measured WCA for substrates coated with pure TiO_2. Before sintering all coated samples are shown to become significantly more hydrophobic after coating compared to uncoated glass. After sintering, however, the samples are shown to become significantly more hydrophilic, both compared to their pre-sintering state and to uncoated substrates. These results confirm both that the substrates were successfully coated and that the coated TiO_2 is crystallising after sintering, as amorphous TiO_2 tends to be more hydrophobic and crystallised TiO_2 more hydrophilic [160-162].

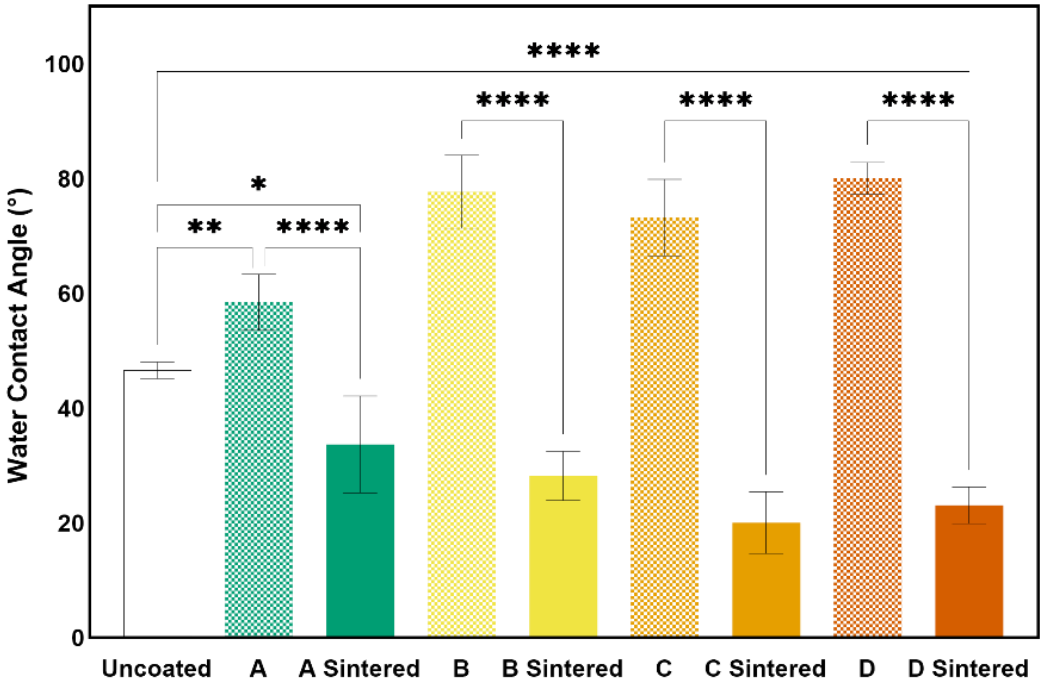

Figure 65 – WCA of glass substrates coated with TiO_2 (mean + standard deviation, n = 6; * p < 0.05; ** p < 0.01; **** p < 0.0001).

Figure 66 details how WCA changes when HAP is incorporated into the TiO_2 suspension. As it is possible to see, when HAP is included WCA in coated samples significantly drops compared to uncoated glass even before sintering. This can be explained by the presence of HAP in the coating, which generally has a hydrophilic nature [163, 164], and can be seen as a sign that HAP has been successfully incorporated both in the initial suspension and in the coating itself.

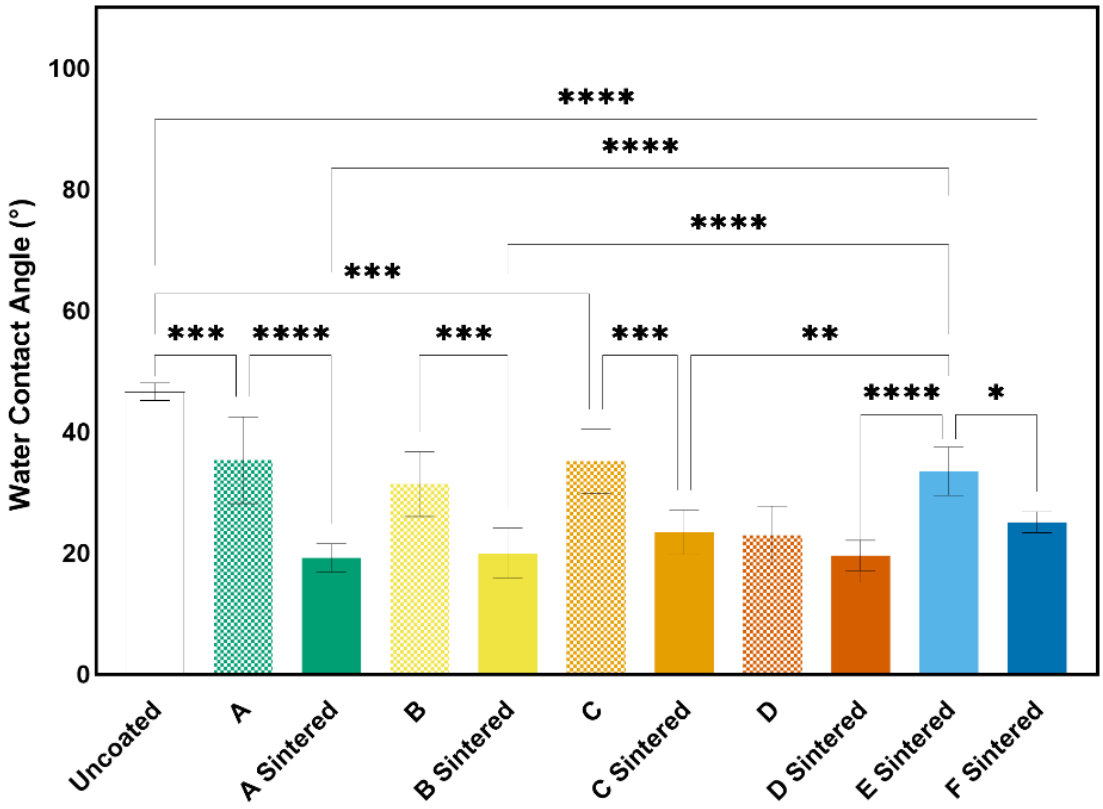

Figure 66 – WCA of glass substrates coated with TiO2/HAP composite (mean + standard deviation, n = 6; * p < 0.05; ** p < 0.01 *** p < 0.001; **** p < 0.0001).

For conditions A, B and C there was also a further significant decrease in WCA after sintering the substrate, again a sign of TiO_2 crystallisation. This drop, while also present, was not significant for sample D. As this was the sample with the longest coating process (3 layers with 5-minute-long coating time), this may be indicative of a better coating process. Finally, WCA was significantly higher for the sintered sample E compared to all other sintered substrates. This might indicate a possible effect on the coating time (this and sample F had a 3-minutes coating time) or a possible interaction between coating time and the number of layers as sample F did not show any significant difference between all other sintered samples.

8.4.2. The evolution of wettability of air-plasma treated substrates changes with different settings

Figure 67 illustrates how WCA evolves in Ti-6Al-4V substrates pre-treated with air-plasma set to different settings, as described in Table 31. The wettability of the substrate's surface evolves in different manners, depending on air-plasma setting. The setting that reached the lowest average WCA was setting B (50% power, 120 sec), which could potentially indicate a more favourable adhesion of the coating materials to the substrate's surface. However, WCA also quickly increases over time with these settings, getting the highest WCA after 60 minutes. In turn, all other settings start with a similar initial WCA, with setting C (100% power, 60 sec) ending with the lowest WCA at minute 60, and setting D (100% power, 120 sec) staying with a relatively constant WCA for at least 30 minutes, being the sample with lowest average WCA from minute 5 to minute 30.

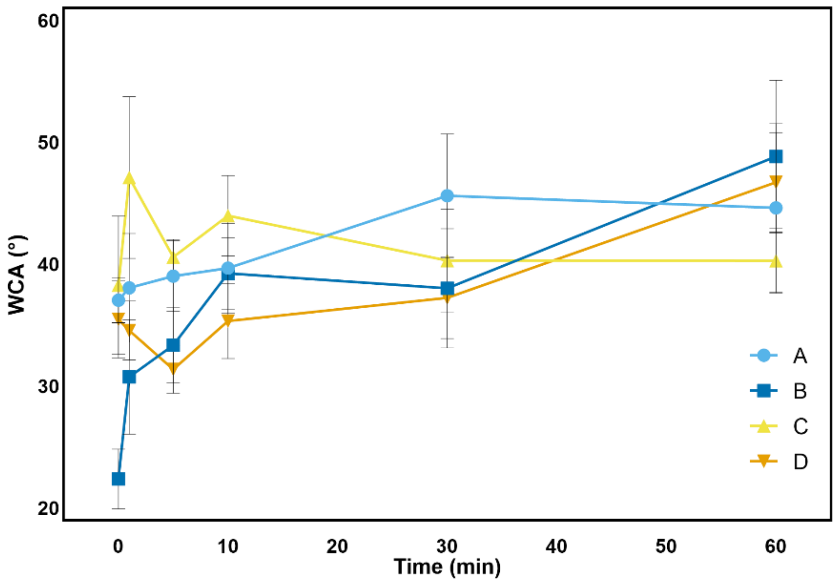

Figure 67 – Evolution of water contact angle on Ti-6Al-4V substrates (mean + standard deviation, n =6).

Because of the perceived stability for longer periods of time, it was decided to also study setting D for PEEK samples, as well as setting E (100% power, 300 sec), to see if an even longer treatment could enhance the evolution of wettability in these substrates. As can be observed in Figure 68, while the average WCA seems more stable when following setting D, the variability in WCA measured is lower overall when following setting E, which could indicate a more uniform pre-treatment and, as such, possibly a more uniform distribution of deposited material after the coating process. As such, it was decided to use setting E as the pre-treatment setting for all substrates.

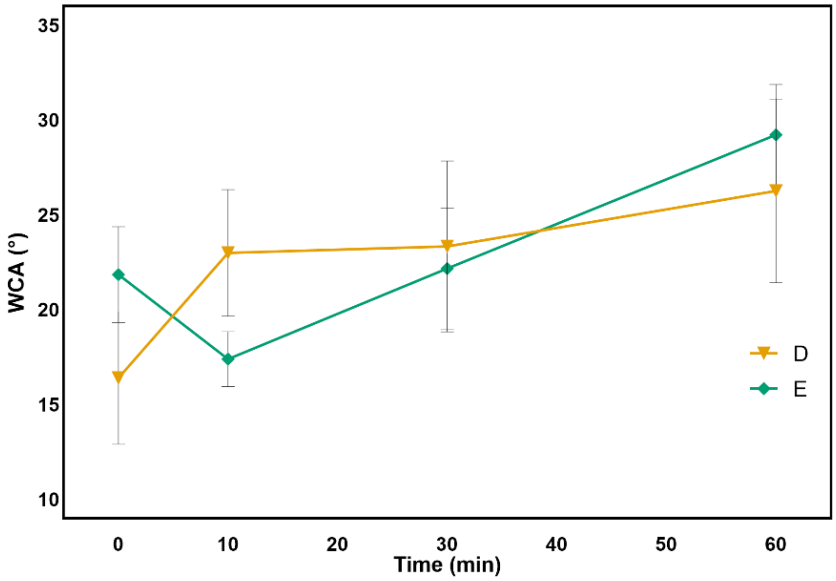

Figure 68 – Evolution of water contact angle on PEEK substrates (mean + standard deviation, n = 6).

8.4.3. The coating conditions and exposure to UV-light potentially affect cell viability

Figure 69 illustrates the metabolic activity of Y201 cells after being cultured in different Ti-6Al-4V substrates. The first result to notice is how UV-treatment seems to

have a negative effect on cell viability, particularly on substrates coated with pure TiO_2. While the UV-light treatment was used to see if the photocatalyst properties of TiO_2 could be used to further remove any organic impurity present in the coating (see Chapter VI), it might also be triggering any other phenomena that has a negative impact on cell adhesion and/or proliferation. This negative effect does not seem to be as profound on substrates coated with the TiO_2/HAP composite, as the difference in metabolic activity between those two groups is less severe. This could also serve as an indicator that HAP is indeed present on the coating, as it would result in less TiO_2 being present on the surface of the substrate and, consequently, have fewer photocatalytic materials that could induce a negative effect when exposed to UV light. Before UV treatment, however, both TiO_2 and composite coated samples seem able to reach similar metabolic activity levels, although without replicates of the TiO_2/HAP it is hard to say if any of the tested coatings performs better than the other.

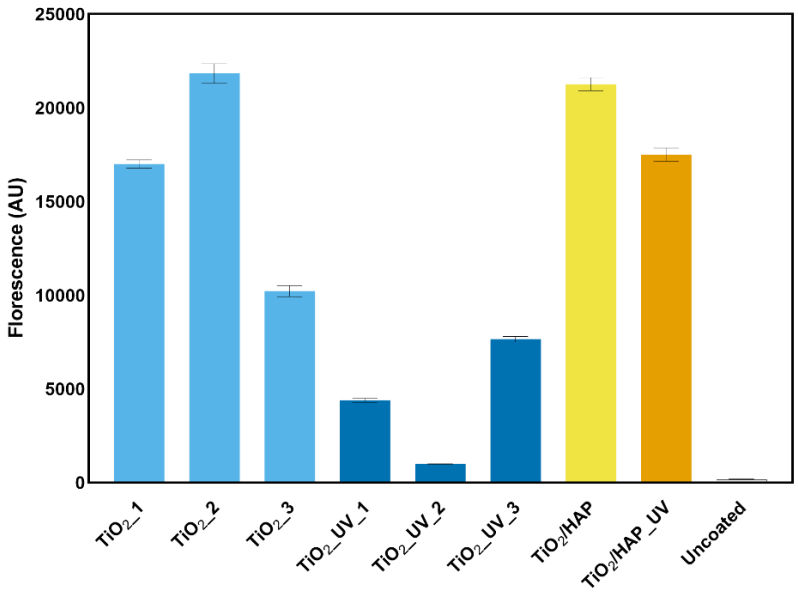

Figure 69 – Metabolic activity of Y201 cells after 7 days in different Ti-6Al-4V substrates (mean + standard deviation, n = 3).

However, it is possible that these results originated from inadequate seeding: the metabolic activity in the uncoated substrates was negligible, indicating that almost no cells were growing in these substrates. These results contradict the literature, as uncoated Ti-6Al-4V is regarded as being biocompatible and MSCs should be able to attach and proliferate on its bare surface [165]. The results present in the next section also show that Y201 cells can indeed attach and proliferate in uncoated Ti-6Al-4V. Furthermore, an inadequate seeding could explain the variability in metabolic activity detected in the pure TiO_2-coated substrates, regardless of UV-treatment. Nevertheless, these results still indicate that the coatings should not be cytotoxic, and that UV treatment is not recommended as it can negatively impact the coating's biological performance.

8.4.4. The substrate potentially affects cell adhesion and proliferation in coated samples

Figure 70 shows the metabolic activity of Y201 cells on the coated substrates for the DoE detailed in Table 33. While variability was high in Ti-6Al-4V substrates, these substrates were shown to have higher average metabolic activity than PEEK substrates. In turn, the results from PEEK were much more reproducible, despite the lower average metabolic activity. These phenomena could be associated with the surface chemistry of each material (PEEK has a much more inert surface compared to Ti-6Al-4V, which can affect both cell and coating adhesion [10, 11, 27]), wettability (coated surfaces are more hydrophilic in Ti-6Al-4V samples which, while good for cell attachment, could also facilitate media evaporation during the seeding density and, as such, compromise cell viability [166]), and substrate dimension (higher thickness of PEEK substrates meant it was easier to assess if the seeding media was leaking from surface of the substrate or not).

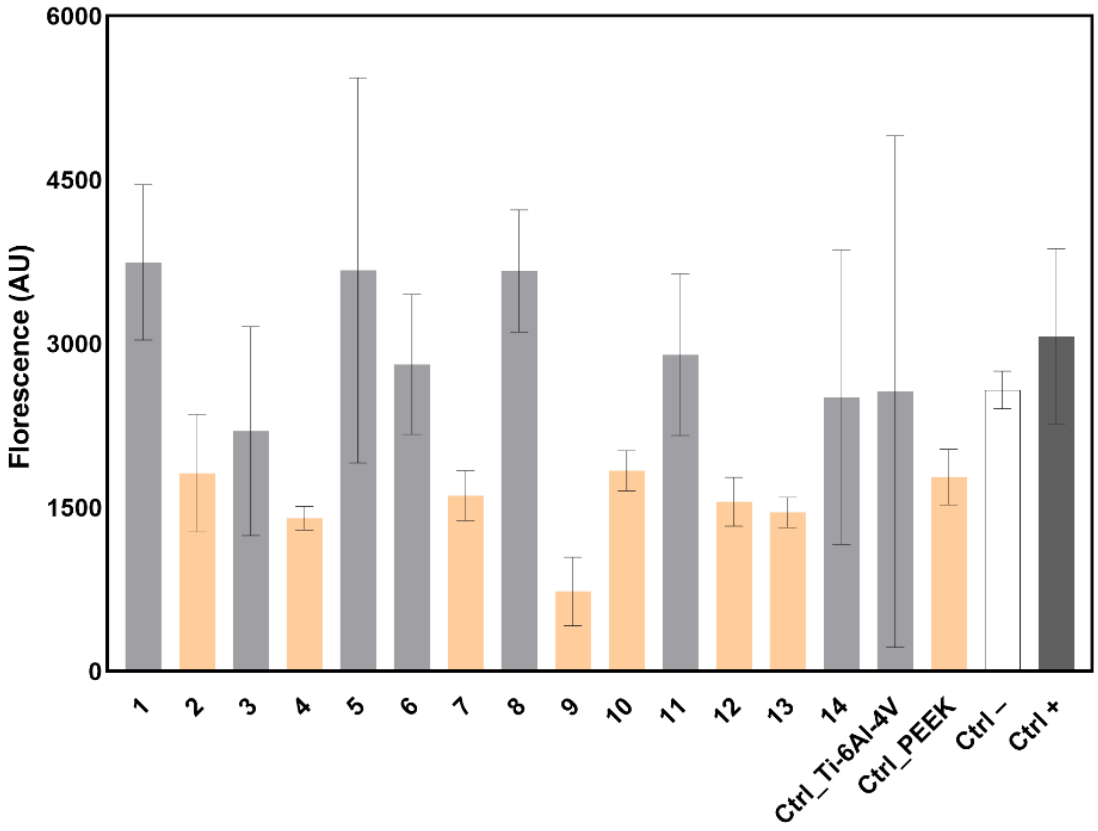

Figure 70 – Metabolic activity of DoE coated substrates at day 7 (mean + standard deviation, n = 3; run order, Table 33).

Comparing the results from day 14 (Figure 71) with the day 7 results, it is possible to see that, while metabolic activity remained largely the same or increased in Ti-6Al-4V substrates, we can see an overall decrease in all PEEK substrates. While this could indicate a cytotoxic effect of those substrates, considering the bioinert nature of PEEK it is most likely that the decrease in metabolic activity is due to poor adhesion of the cells and/or coating to the substrate, indicating that a more effective pre-treatment of PEEK's surface might be required.

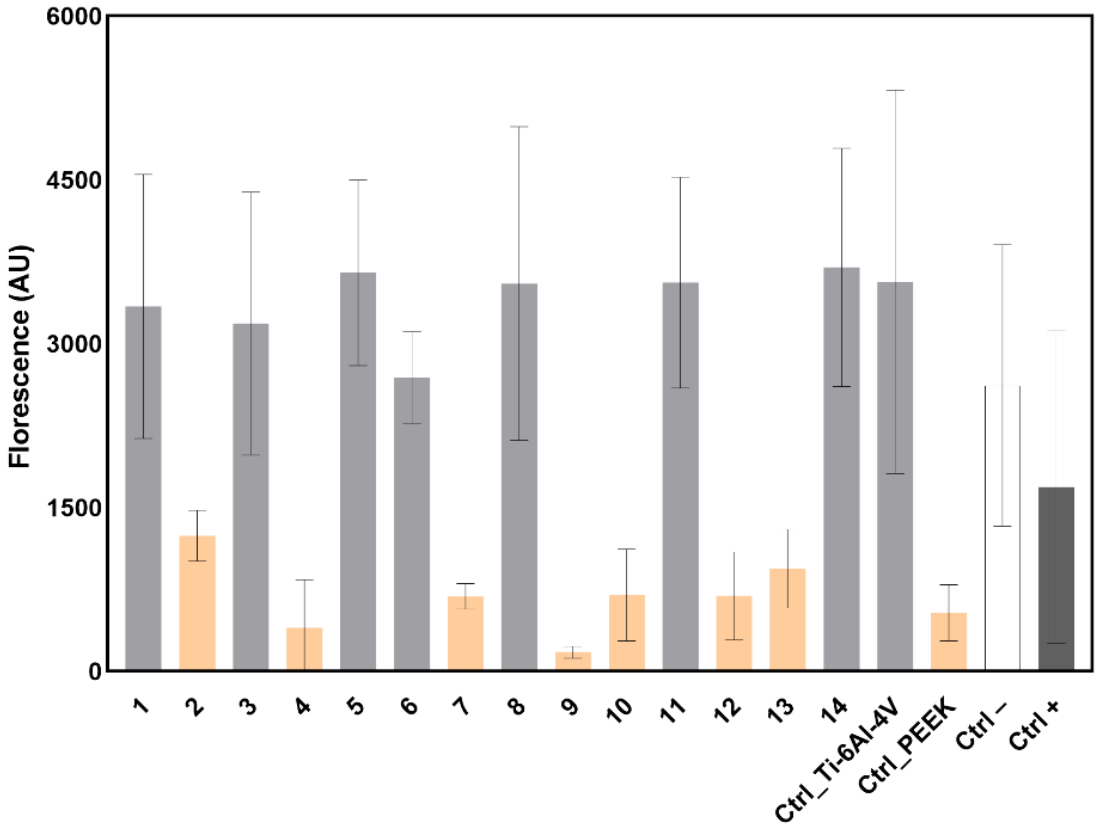

Figure 71 – Metabolic activity of DoE coated substrates at day 14 (mean + standard deviation, n = 3; run order, Table 33).

It is important to notice the increase in variability in metabolic activity in the control groups Ctrl – and Ctrl +. This resulted from cells growing overconfluent in these conditions and starting to detach in some of the wells. This could potentially indicate that a lower cell density might be needed during seeding, to reduce the risk of cell detachment in future experiments.

8.4.5. TiO_2/HAP coatings can significantly improve the osteogenic potential of substrates

Figure 72 details the results obtained from the DNA-adjusted ALP activity at day 14 measured for all tested conditions. There were two DoE runs, 11 and 13 (run order from Table 33) that not only performed significantly better than their uncoated counterparts and Ctrl – but were also able to perform similarly to Ctrl +, which represents cells cultured in media optimised for osteogenic differentiation. Even before performing the DoE analysis, these results show that it was indeed possible to develop composite TiO_2/HAP coatings using sol-gel chemistry which improve the osteogenic potential of Ti-6Al-4V and PEEK substrates and, as such, could potentially improve the osteointegration of spinal cages based on those materials.

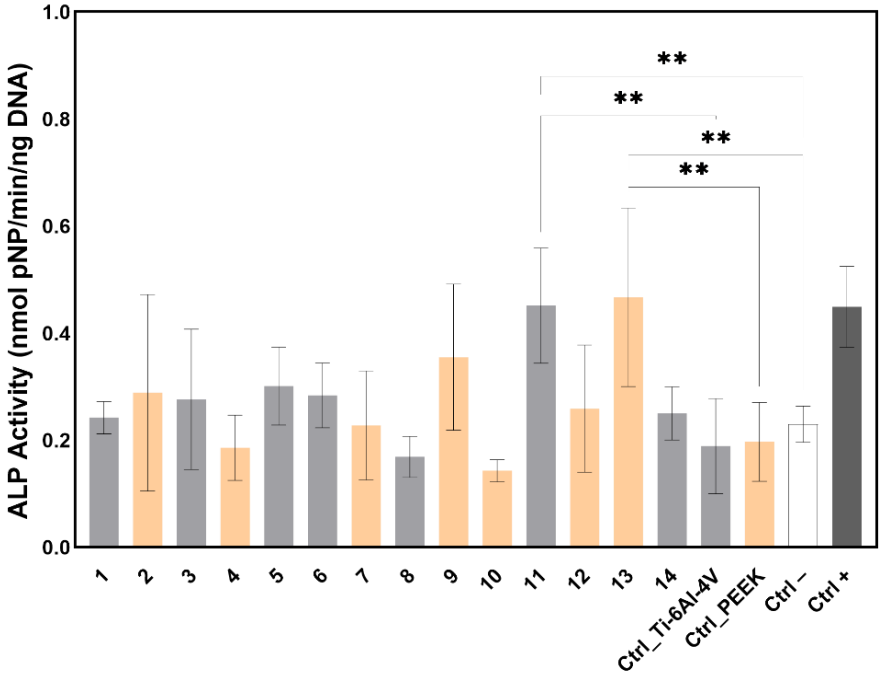

Figure 72 – DNA-adjusted ALP activity of DoE coated substrates (run order, Table 33) at day 14 (mean + standard deviation, n = 3; ** p < 0.01).

For the DoE analysis, average DNA-adjusted ALP activity measured for each condition was used, which can be consulted in Table 34.

Table 34 – DoE results

Standard order	Factor						ALP Activity
	A	B	C	D	E	F	
1	–	+	+	+	+	+	0.4517
2	+	–	–	–	–	–	0.2888
3	+	0	+	–	–	+	0.4673
4	–	0	–	+	+	–	0.1690
5	+	+	0	+	–	–	0.2590
6	–	–	0	–	+	+	0.2764
7	+	–	+	0	+	–	0.1860
8	–	+	–	0	–	+	0.2423
9	+	–	–	+	0	+	0.3551
10	–	+	+	–	0	–	0.3011
11	+	+	–	–	+	0	0.2277
12	–	–	+	+	–	0	0.2503
13	–	0	0	0	0	0	0.2838
14	+	0	0	0	0	0	0.1432

Due to the lack of replicate runs in DSD (see section 2.7.4), it does not make sense to present a replicate plot for this data. Analysing the histogram of the results (Figure 73), the data seems to possibly be following a trimodal distribution, which suggests that the data might need to be transformed to obtain a valid model. The best transformation was determined using the automatic function from the software *Minitab 20.0*.

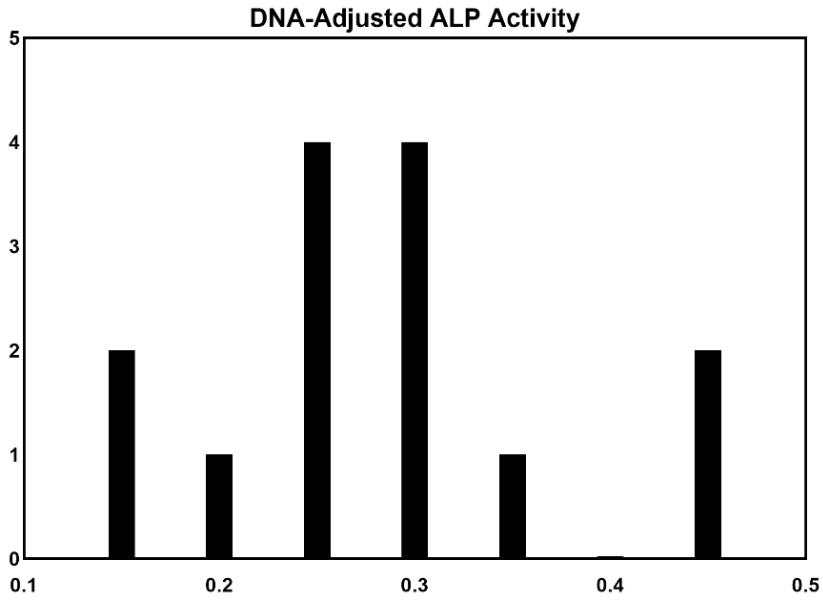

Figure 73 – Histogram of DNA-adjusted ALP activity.

Equation 24 details the optimised model for DNA-adjusted ALP activity of coated substrates, with Figure 74 detailing its respective Pareto chart of standardised effects, and Figure 75 its summary of fit. As it is possible to see, all main factor interactions had to be included to obtain a valid model. Moreover, as suspected by the histogram in Figure 73, the responses indeed had to be transformed to obtain a valid model. Overall, the model indicates that ALP activity and, consequently, the osteogenic potential of a coated substrate is increased when said substrate is composed of PEEK (factor A), when increasing the amount of HAP present in the coating (factor B), when coating with more layers (factor C) at 1 or 5 minutes per layer (factor D, which has a significant quadratic effect), with a faster moving robot (factor E) and faster heating rates (factor F). The interaction between factors D and E was also found to be significant).

Equation 24 – Optimised model for DNA-adjusted ALP activity

$$\frac{ALP^{\lambda-1}}{\lambda \times g^{\lambda-1}} = -4.7068 + 0.0315A + 0.0305B + 0.0748C + 0.0008D - 0.0113E + 0.0988F + 0.1167D^2 + 0.0935DE \quad \Big| \quad \lambda = 3,\ g = 0.264568$$

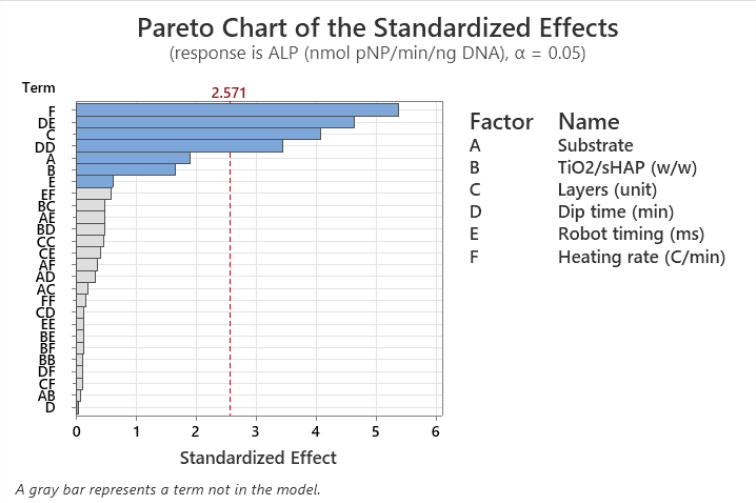

Figure 74 – Pareto chart of standardised effects for optimised ALP model.

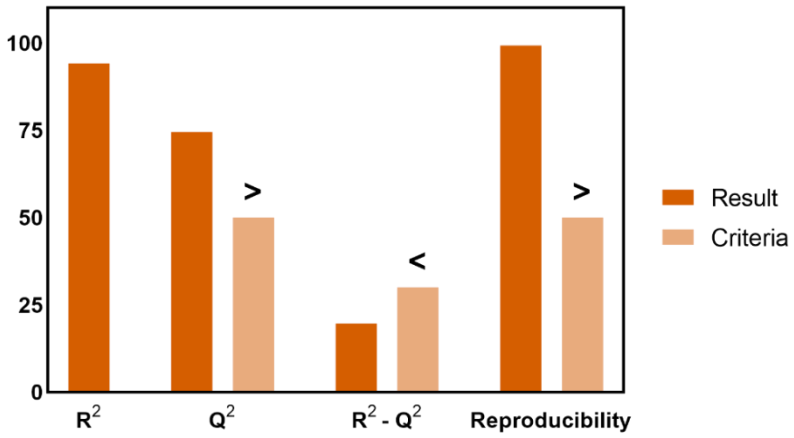

Figure 75 – Summary of fit of optimised ALP model.

The effect plots in Figure 76 help to better understand the effects of each factor on the osteogenic potential of coated substrates. Interestingly, while the optimisation process resulted in the quadratic effects of factors B, C and F being discarded from the final model, it is still possible to see a curvature in their individual effects. Nevertheless, it is quite clear that the best results for all these factors are at one of the extremities of their experimental region, with no detectable valley or peak (see the main effect from factor D), hence the optimised model ignores their quadratic effects. Furthermore, the interaction plot for factors DE shows the curious interaction between both factors: shorter dipping times seem to be enhanced by faster robot movements (represented by shorter timings), while a slower coating process favours longer dipping times. ALP activity is most optimal, however, when both D and E are set to their – levels.

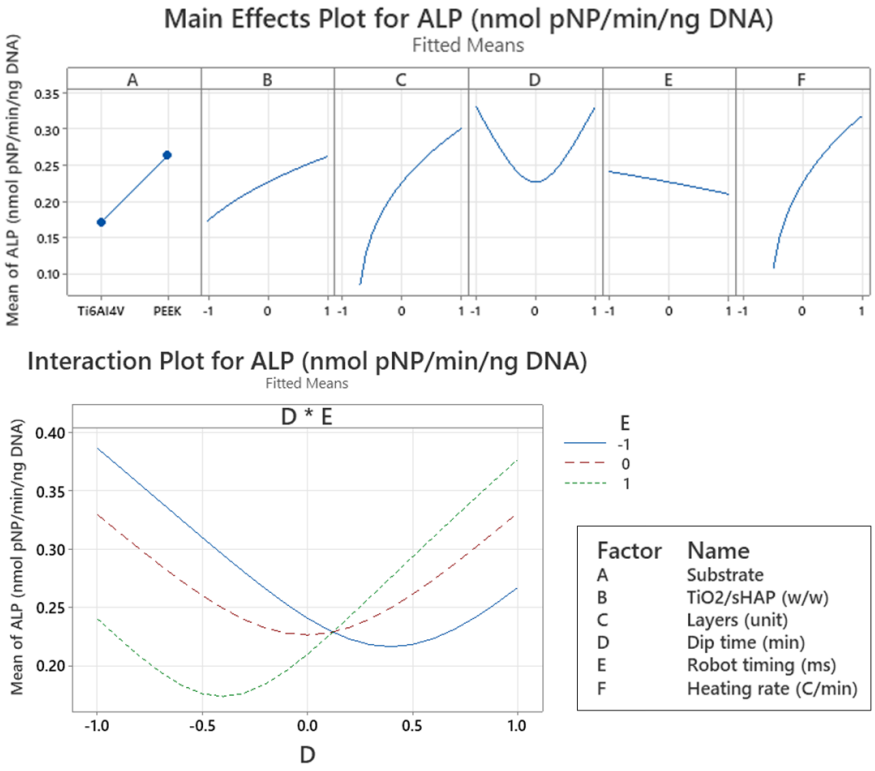

Figure 76 – Main effects and interaction plots of optimised ALP model.

The optimal coating conditions were calculated using the optimisation tool from *Minitab 20.0*. The tool was set to calculate the optimal conditions for both kinds of substrates used during the design, and the results can be seen in Table 35. As expected, as the only interaction effect deemed significant was between factors D and E, the optimal coating conditions for both Ti-6Al-5V and PEEK are the same. Overall, it can be concluded that ALP activity and, consequently, osteogenic activity of coated substrates is at its highest when coating said substrates with a TiO_2/HAP weight ratio of 1/1.5, with 5 layers, dipping the substrate in the composite suspension for 1 minute using faster robot movements, and with a faster heating rate of 20°C/min during sintering. Overall, these results show that the addition of HAP into the TiO_2 sol-gel system does indeed result in enhanced osteogenic potential and, as such, could potentially increase the osteointegration of coated implants. Furthermore, it is shown that faster cycles and sintering processes are optimal for this objective, despite the osteogenic potential also increasing with an increase in the number of coating cycles performed.

Table 35 – Optimal coating conditions for both substrates (design from Table 32)

Value	Factor					
	A	**B**	**C**	**D**	**E**	**F**
Model	**–**	+	+	–	–	+
Real	Ti-6Al-4V	1/1.5 TiO_2/HAP	5 layers	1 min	10 ms	20°C/min
Model	+	+	+	–	–	+
Real	PEEK	1/1.5 TiO_2/HAP	5 layers	1 min	10 ms	20°C/min

8.4.6. TiO_2/HAP coatings change the surface topography of Ti-6Al-4V and PEEK substrates.

Figure 77 shows the 3D plot of the surface of uncoated Ti-6Al-4V and PEEK, obtained by optical profilometry at 2.25x magnification. Overall, it is possible to see that the Ti-6Al-4V substrates present an overall rougher surface compared to PEEK, which is relatively smoother. It is important to notice that PEEK surfaces also present deep, crater-like areas which were also visible to the naked eye (see Figure 19 in Chapter IV). These areas might be responsible for the biological results obtained for PEEK samples, as they might have shielded the coating deposited and/or the cells seeded in those crater areas from coating and/or cellular detachment.

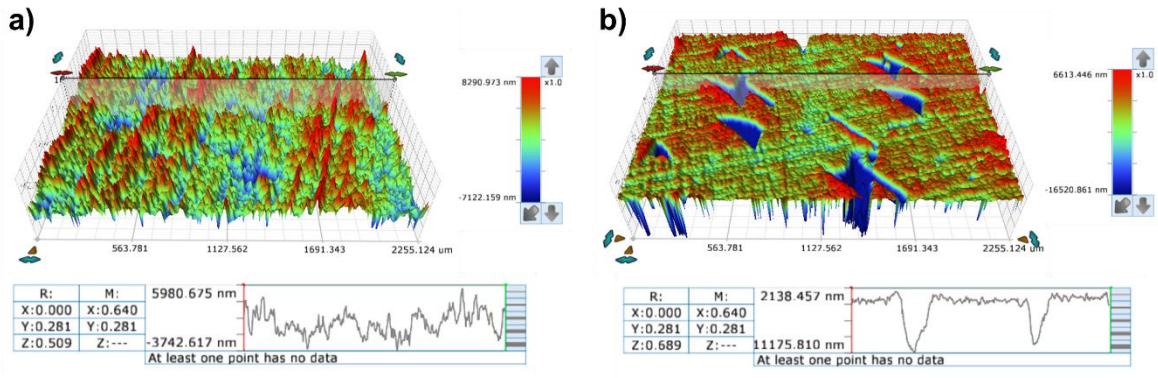

Figure 77 – Profilometry results (2.25x magnification) of uncoated substrates: a) Ti-6Al-4V; b) PEEK.

Figure 78 shows the 3D plots of the substrate-coating interfaces of the coated Ti-6Al-4V and PEEK substrates, alongside the profiles used to then calculate the thickness of each coating. At first glance, it is possible to see that the overall topography is different between the substrates used, regardless of coating. Ti-6Al-4V coatings seem to have a topography closer to randomly spread particle

agglomerates, while the surface of PEEK coatings looks like a stack of parallel saw-like structures. Furthermore, the overall height difference between the uncoated and coated areas is more noticeable in the Ti-6Al-4V substrates than in the PEEK ones. These results suggest that more material has been deposited in the metallic substrates compared to the polymeric ones. Between Ti-6Al-4V substrates, it is also possible to see that the results obtained suggest that more material is deposited when using C6- instead of Mg-enriched hydroxyapatite, as the increase in height seems more prominent in the former case than in the latter.

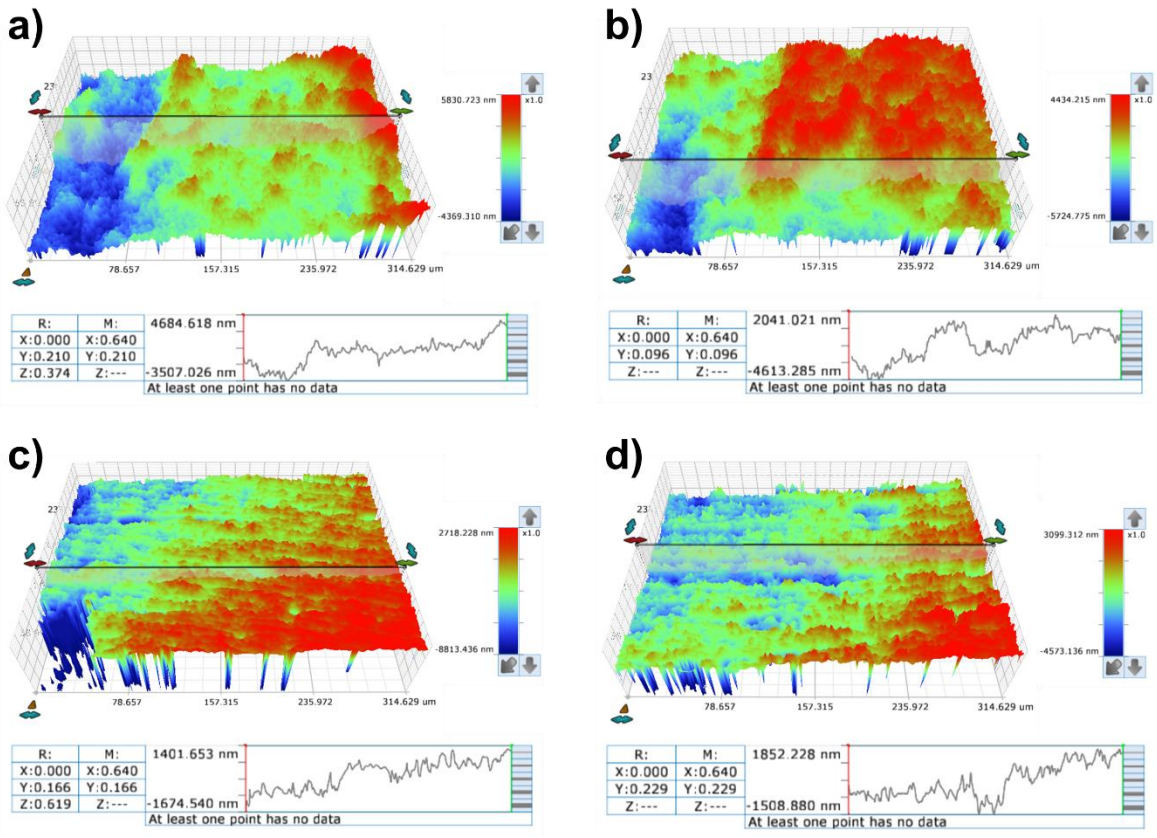

Figure 78 – Profilometry results at substrate/coating interface: a) Ti-6Al-4V and Mg-enriched HAP-containing coating; b) Ti-6Al-4V and C6- sHAP-containing coating; c) PEEK and Mg-enriched HAP-containing coating; d) PEEK and C6- sHAP-containing coating.

The thickness measured for each substrate (difference between the average heights of the coated and uncoated areas), shown in Table 36, confirms this assumption, as the value for Ti-6Al-4V coatings containing C6- sHAP is higher than the one obtained for coatings containing Mg-enriched HAP. The same cannot be said about coatings in PEEK substrates, as the thickness of the coatings with each HAP are approximately the same. However, the type of HAP used still affects the surface morphology of coatings deposited in PEEK substrates. As also shown in Table 36, both the average and root mean square of surface roughness (Sa and Sq, respectively) are higher when C6- is incorporated, both indicating an increase in overall surface roughness compared to Mg-enriched HAP. This is also true for coatings deposited on Ti-6Al-4V substrates.

Table 36 – Profilometry results (Sa – average surface roughness; Sq – root mean square of surface roughness)

Sample		Measurement		
		Sa (nm)	Sq (nm)	Thickness (µm)
Ti-6Al-4V	Uncoated	753	958	N/A
	Mg-enriched	781	984	3.01
	C6-	827	1022	3.75
PEEK	Uncoated	380	481	N/A
	Mg-enriched	398	520	1.25
	C6-	469	728	1.25

Overall, it is possible to see an increase in surface roughness between coated and uncoated substrates regardless of substrate and HAP used. Between substrates, the Ti-4Al-6V substrates have higher surface roughness than PEEK samples. As, in general, higher surface roughness correlates with higher surface area, which in turn is generally preferred for cell attachment and proliferation, this could indicate that the biological performance of the developed coatings might not only be affected by their composition, (see results from section 8.4.5 and Chapter VI), but by their topography as well.

8.5. Discussion

This chapter studied the development of sol-gel-based composite TiO_2/HAP osteoinductive coatings for spinal fusion cages. One of the main issues with spinal fusion surgery is improper bone integration of the fusion cage, which can lead to a more difficult recovery period for the patient, decrease success rates and increase the need for revision surgery [9, 13]. This problem is particularly relevant for PEEK cages, traditionally a bioinert material [10, 11, 27]. Coated fusion cages are already available, however, they can involve coating techniques which either result in lower-quality coatings or require expensive equipment [36, 167, 168]. The present work aimed to solve this issue by studying a coating technique which could result in high-quality composite coatings using cost-effective techniques which did not require specialised equipment. The coating method chosen was sol-gel chemistry [40, 63, 130].

The initial coating tests were performed in glass substrates as they were a more readily available material compared to the substrates of interest for this project (Ti-6Al-4V and PEEK, the most common materials used in the production of fusion cages [10, 11, 14]). To improve the adhesion potential of the substrates, the samples were pre-treated using air plasma, which is able to introduce polar functional groups to the surface of not only glass [169] but of Ti-6Al-4V [170] and PEEK [160] substrates as well, which can, in turn, be used to support a better adhesion of the materials being coated.

During the first preliminary tests, it was developed coatings composed of pure TiO_2, to see if the sol-gel protocol developed during Chapter VII could be used for coating purposes. These tests were not conducted using the optimal synthesis conditions found in Chapter VII as they were conducted while the TiO_2 optimisation process was still ongoing. The formulation chosen followed the conditions that, at the time, were thought to optimise crystallisation (high acetic acid volume, reaction temperature and sintering time, and low ethanol volume). To check if the coating

process was successful, WCA was measured in uncoated and coated substrates, as a change in WCA would indicate a change in surface properties. As seen in Figure 65, WCA significantly changed between uncoated and TiO_2-coated glass, demonstrating that the substrates were successfully coated. Sintering the coated sample further changed the WCA of its surface: glass became more hydrophobic before sintering and more hydrophilic after the process. This not only confirms that TiO_2 is being deposited, but that it is still crystallising as intended. As other works have shown, WCA of TiO_2 tends to be more hydrophobic when in an amorphous state (WCA usually between 70° and 80°), dropping considerably when crystallised into anatase (WCA usually between 20° and 35°) [160-162].

Adding HAP into the sol-gel suspension resulted in coatings with a more hydrophilic behaviour even before sintering, as seen in Figure 66. This can be explained by HAP's typical hydrophilic behaviour [163, 164], and can be seen as an indicator that HAP has been successfully incorporated in the coating suspension and deposited onto the substrate. WCA further dropped after sintering, again showing the successful crystallisation of TiO_2, demonstrating that is indeed possible to obtain composite coatings of crystallised TiO_2 and HAP. This drop was not significant in the sample coated following condition D (3 layers, 5-minute coating time), as WCA before sintering was already low. This was an early sign that the coating conditions could potentially be optimised. The results from condition E (1 layer, 3-minute coating time) also show that the coating process can be optimised, as it was the only condition with a significantly worse WCA after sintering. As condition F (3 layers, 3-minute coating time) still showed a similar WCA to other sintered samples, it is possible that a quadratic effect is present in the coating time which favours shorter or longer coating times, or that coating time interacts with the number of layers for a worse result when following the settings from condition E.

As previously stated, an effective pre-treatment was of the uttermost importance to ensure coating adhesion to PEEK surfaces, which is traditionally an inert material [10, 11, 27]. Air plasma was chosen as a pre-treatment both due to

availability and for having been shown to improve PEEK's surface properties [133, 135, 160, 171]. Despite TiO_2 naturally occurring in Ti-based substrates and, consequently adhering well to Ti-based materials, Ti-6Al-4V can also benefit from air-plasma pre-treatment [170]. As more Ti-6Al-4V substrates were available, the initial tests were performed using samples of this material and studying more time points. It was difficult to decide which of these treatments could be considered the best performing. On one hand, as shown in Figure 67, treatment B (100% power, 60 s) had the initial lowest WCA measured, but was also the treatment that resulted in the highest increase in WCA over time. On the other hand, treatment C (50% power, 120 s) had the lowest final WCA, but the initial WCA was quite unstable. In the end, it was decided to keep studying treatment D (100% power, 120 s), as it showed a good compromise between low WCA and stability for longer periods of time.

Studying the air-plasma treatment on PEEK substrates was also challenging. As shown by Figure 68, treatment D did show a more stable WCA average at different time points. However, treatment E (100% power, 300 s) presented less variability in the WCA measured at each time point, even if the average WCA measured was less stable over time. In the end, it was decided to use treatment E for all samples, as it was decided that a more stable average WCA was more important, considering that WCA was still lower than untreated Ti-6Al-4V and PEEK (average WCA 76° and 72°, respectively).

Before performing the DoE, it was important to see if the coatings could potentially be cytotoxic, especially considering the optimal TiO_2 synthesis conditions still leave around 5.52% of organic residues present on its surface (see results from Chapter VII). It was also decided to test coated samples that went through a UV-light treatment before sterilisation in 70% ethanol. The photocatalyst properties of TiO_2 can degrade the acetate groups that are the source of organic residue from TiO_2 and could potentially be used as a method to further clean the substrates [151, 152]. The results obtained, however, showed that the UV-light treatment might instead have a negative impact on metabolic activity, as can be seen in Figure 69. This could be a

consequence of how that photocatalyst effect takes place, which is based on the formation of free ·OH radicals and other reactive oxygen species, which are found to indeed be cytotoxic [172, 173]. This could potentially be a problem, as the same effect can be induced by gamma radiation [174, 175], which is commonly used to sterilise medical implants [153]. While a decrease in metabolic activity was also detected on samples coated with TiO_2/HAP, said decrease was not as severe in this case, possibly due to less TiO_2 being present in those coatings in relative quantities.

The coatings themselves, however, do not seem to be cytotoxic when not exposed to UV light, as these did show relatively high metabolic activity. It is important to notice, however, the significant differences in metabolic activity detected between pure TiO_2-coated substrates, as well as the almost negligible activity detected in uncoated substrates. While these could indicate that the coating process is not uniform and that cells do not grow in uncoated Ti-6Al-4V, this is most likely due to an improper cell seeding method. As the DoE results provide more evidence towards the problem being an improper seeding method, these results will further be discussed later in this section.

One problem found when preparing the 1/1 (w/w) suspension of TiO_2/HAP is that using 15.2 ml of ethanol made it difficult to incorporate HAP, even after ultrasound treatment. To be able to study suspensions with higher HAP quantities, it was decided to increase ethanol volume to 20.0 ml for the coatings. While this lowers the crystallinity of TiO_2 (see Equation 21 from Chapter VII), the difference in results should not be too important: run 3 from the TiO_2 crystallisation DoE was conducted with suboptimal ethanol volume (22.8 ml) and reached a similar crystallinity compared to the optimal conditions (77.83%, compared to 79.97%). HAP could have also been introduced after the synthesis of TiO_2 following the optimal conditions, when the suspension volume is adjusted to 40 ml. However, it was hypothesised that HAP would be better integrated within the sol-gel process if introduced before the hydrolysis process had started.

The first factor that was deemed interesting to study using DoE was the substrate itself, as that would allow us to more easily compare both substrates while also reducing the number of samples necessary for each material in half. Another factor of interest was the TiO_2/HAP ratio used. It was decided to study the ratio in weight, as it has been used in other similar projects [66, 71]. Moreover, the – condition was set as a pure TiO_2 coating to better compare the effect of adding HAP without needing an extra control group (because of the kind of DoE used, dropping this factor would not affect the number of required runs – see 2.7.1.2 in Chapter II). Other factors deemed interesting were the number of layers deposited and dipping time, as both could potentially increase the quantity of material being deposited, and the speed of the dipping process (translated to robot timing) and heating rate during sintering, as they could influence the coating's integrity. Similarly to Chapter VI for the synthesised sHAP, the osteogenic potential of the coated substrates was evaluated by measuring the DNA-adjusted ALP activity of hTERT-MSC Y201. In this case, the cells were in direct contact with the coated substrate, and four different kinds of control groups were used: uncoated Ti-6Al-4V, uncoated PEEK, and cells grown directly in 48-well plates in either expansion (Ctrl –) or osteogenic (Ctrl +) media. Cell metabolic activity was also measured with resazurin reduction assay, to try to better understand cytotoxicity and cell growth in the coated substrates.

Regarding the metabolic activity results, as predicted, the coatings do not seem to be cytotoxic, as the average metabolic activity from the coated substrates is, in general, similar to that of the uncoated substrates. Moreover, the average response in Ti-6Al-4V substrates is similar to or even higher than the one measured for Ctrl – and Ctrl +, on both day 7 (Figure 70) and day 14 (Figure 71). Variability between samples of the same condition/run is still high, similar to the preliminary tests. However, unlike those preliminary tests, during this experiment, it was possible to have Y201 cells growing on uncoated Ti-6Al-4V substrates. These results made it even more suspicious that the variability in metabolic activity is due to improper seeding method.

The average metabolic activity in PEEK substrates however, while more reproducible, is also lower than that of Ctrl – and Ctrl +, especially on day 14. These results were expected for uncoated PEEK substrates. PEEK is a bioinert material [10, 11] and it was expected that Y201 cells would have a problem adhering to its surface. However, it was expected that this would not occur in the coated samples, as the cells should attach to the coating. It is possible that, in those cases, the coating itself did not properly attach. The air-plasma treatment used should have been enough to prevent coating detachment from the PEEK substrate, as other works have successfully used similar strategies to improve the adhesion strength of the material [133, 135, 171]. These strategies, however, polish PEEK with 800-grit sandpaper before treatment, which was not undertaken here. There were still some cells attached to PEEK substrates, likely due to the presence of “crater” areas on its surface. These craters were observable to the naked eye (see Figure 19 from Chapter IV), and were further visualised using profilometry (see Figure 77). It is possible that the cells and deposited materials present in these pockets were shielded from the activities that would potentiate cell and coating detachment, namely the resazurin reduction assay itself and the media change on day 7. It’s possible that those same craters shielded cells during the seeding process, possibly being the reason why metabolic activity is less variable in PEEK samples.

Even before starting the proper DoE analysis, it was already clear that the main goal of this project was met, as two of the coating conditions, 11 and 13, were not only able to significantly increase ALP activity when compared to Ctrl – and their respective uncoated substrate, but were able to reach ALP activity levels close to those of Ctrl +, as it can be seen in Figure 72. The figure also highlights the importance of normalising ALP results to DNA-quantity present in the lysates: despite the high variability in metabolic activity, the cells that were indeed present at the surface of each sample for each condition were differentiating at similar rates.

DoE analysis showed that all factors in study must be present in the final model to have it pass all summary of fit tests that can be performed for DSD. This

includes the substrate in study (factor A), with PEEK surprisingly being the material with better osteogenic potential. This goes against what other researchers have found, with their results favouring Ti-6Al-4V [176]. However, the “craters” present in PEEK could again be responsible for this increase in ALP activity in PEEK substrates. If we consider those craters as pores, PEEK with surface porosity has been shown to have increased osteogenic potential when compared to non-porous Ti-6Al-4V [177]. While ALP activity in that study was actually lower in porous PEEK, the study suggested that it was due to the cells being in a later stage of differentiation, as all other signs pointed towards porous PEEK being the best-performing substrate. A similar effect may be happening in this case, albeit still in the early stages of osteogenic differentiation, when ALP is present at a higher level.

Increasing the quantity of HAP present in the coating (factor B) also had a positive effect on the osteogenic potential of the coatings, showing the benefits of having a composite TiO_2/HAP coating instead of a pure TiO_2 one. Interestingly, the results slightly contradict what other researchers have found, which favoured a TiO_2/HAP ratio of 1:1 in weight [66]. However, it is important to notice that the study used a higher TiO_2/HAP maximum ratio (1/2, compared to 1/1.5 used in this work) and a different cell line (MG-63, which is an osteosarcoma cell line). It is possible that both those factors explain why a different TiO_2/HAP ratio was found to be optimal in the present research. It’s also important to note that these coatings were developed using the Mg-enriched HAP used as a control in the experiments detailed in Chapter VI. Considering that there were sHAP formulations that performed significantly better in indirect contact than the HAP used during this DoE, it is quite possible that the effect of HAP in the coating can be even further improved if the coating is developed using those better-performing formulations.

As for the number of layers deposited (factor C), ALP activity was also found to increase with the number of layers used. While a different study showed no significant difference between 3 and 5 layers of pure TiO_2 coatings [131], said study evaluated the bioactivity of the coating by soaking them in simulated body fluid, and

not with biological tests. Nevertheless, the researchers attributed the better properties to a rougher surface obtained from the increased number of layers, which could also be the case for the present research. An increase in roughness can also explain the effect of heating rate during sintering (factor F), as faster sintering rates have been linked to rougher surfaces in sol-gel coatings [178], which is, in turn, linked to an increase in osteogenic potential [179]. Faster heating rates are also shown to prevent coating shrinkage during the sintering process, important for its integrity [180].

Interestingly, the DoE also confirms what was suspected during the preliminary coating tests: 3-minute-long coating processes (factor D) seem to negatively affect the coating's performance, compared to either 1-minute or 5-minute-long processes. As far as it is known, no other study has investigated the effect of dipping times as short as the ones used in this study. Coating adsorption may be stronger during the first minute of the dipping process, with the deposition of any extra material becoming more stable the longer the coating process takes. Another possible explanation is perhaps a drop in coating roughness from 1 to 3 minutes of dipping time, which could again increase when coating for at least 5 minutes. It would be of interest for future work to study in more depth the effect of dipping time on the osteogenic potential of these coatings.

Also interesting is the effect of robot timing (factor E), which effectively represents dipping speed (shorter timings represent faster speeds). By itself its effect is not significant, however, its interaction with coating time can affect the biological performance of the coating. Specifically, shorter coating times are enhanced by a faster dipping process, while a slower process is preferred for longer coating periods. As far as it is known, no other study has remarked on this effect. Nevertheless, the best results are found when both factors are set to their – levels, or in other words, coating for 1 minute with a faster dipping process.

Because no interactions between factor A and any other factor were deemed significant, the optimal coating conditions were the same regardless of using Ti-6Al-4V or PEEK as substrate. Due to the aforementioned seeding problems, it was not possible to test the *in vitro* performance of the optimal coating conditions. It is suspected that these coating conditions result in a surface that might be too hydrophilic to use the single-drop seeding method without the seeding media evaporating and the cells dying during the process. As a reminder, the more hydrophilic a material is, the faster the evaporation at its surface [166]. Nevertheless, because highly hydrophilic surfaces increase MSC proliferation and differentiation [181, 182], this can be an early sign that, with a proper seeding protocol, coating Ti-6Al-4V or PEEK following the optimal conditions will indeed result in enhanced osteogenic potential.

Studying the morphology of the optimal coatings can also provide an early insight into the biological performance of the optimal coatings. At the same time, it would be interesting to see if changing the Mg-enriched HAP used during the DoE for sHAP following formulation C6-, the best-performing sHAP from Chapter VI, could provide any other advantage besides its composition (as a reminder, the indirect contact *in vitro* tests detailed in Chapter VI show that C6- performed significantly better than Mg-enriched HAP). The first thing to notice is that coatings in Ti-6Al-4V substrates appear to be thicker than coatings in PEEK substrates. This could be due to both the innate affinity of TiO_2 to Ti-based substrates (a layer of TiO_2 naturally occurs in Ti-based implants [10, 11, 26], and PEEK's general inert behaviour [10, 11, 27]. Another reason for this difference in coating thickness could perhaps be a possible shrinkage effect in PEEK substrates, making the coatings thicker at the centre of the coated area. This possible shrinkage could also explain the adhesion problems detected on PEEK substrates during the DoE experiments [183]. Regardless of substrate, the obtained coatings are one to two degrees of magnitude smaller than typical HAP-based coatings (1.25 – 3.75 µm, compared to the typical 50 – 200 µm range) [184]. It is important to notice, however, that the typical range was found to be optimal for plasma-sprayed HAP coatings, with

mechanical performance favouring thinner coatings [185]. Other techniques, including sol-gel, were able to obtain thinner coatings with similar performance to the conventional plasma-sprayed coatings, even at the nanoscale [184]. The coatings obtained during this work were within the thickness range usually obtained with sol-gel chemistry [186].

The overall surface roughness seems to increase when a coating is applied, regardless of the substrate used. Replacing Mg-enriched HAP with C6- sHAP further enhances the topography of the coating, with the coatings containing the latter showing a rougher surface compared to coatings containing the former. In Ti-6Al-4V substrates, coatings are also thicker when developed using C6-. However, it is important to notice that the differences in roughness and thickness could be due to possible differences in particle size due to grinding, and it would be interesting to compare coatings prepared with particles ground in a similar manner. Nevertheless, the current results suggest that, besides composition, C6- might further enhance the osteogenic potential of the TiO_2/HAP coatings by also providing a more suitable surface topography for MSC expansion and differentiation than Mg-enhanced HAP.

Finally, and bearing in mind that the model developed in the current chapter is not an optimisation model but a screening one, the optimal coating conditions could potentially lead to a 150.2% increase in ALP activity and, consequently, of the osteogenic potential of Ti-6Al-4V substrates (0.4550 compared to an average of 0.1888 nmol pNP/min/ng DNA) and a 141.3% increase in PEEK substrates (0.4754 compared to an average of 0.1970 pNP/min/ng DNA). Considering the 72.0% increase in ALP activity from C6- sHAP compared to Mg-enriched HAP (see results from Chapter VI), the osteogenic potential for both Ti-6Al-4V and PEEK can potentially be increased up to 315% when coated following the optimal conditions. However, again reminding that the model created in this chapter is not an optimisation model, it will be necessary to test the optimal conditions *in vitro* to properly assess their biological performance.

8.6. Summary

In this chapter, a composite TiO_2/HAP dip coating protocol was successfully developed, based on sol-gel chemistry, capable of increasing the osteogenic potential of both Ti-6Al-4V and PEEK substrates. This coating could be explored for improving the osteointegration of spinal fusion cages composed of these materials. Regardless of substrate, ALP activity of hTERT-MSCs Y201 is increased when coating with 5 layers of TiO_2/HAP composite with a 1/1.5 in weight ratio. A faster coating process, with 1-minute-long dipping stages, increased dipping speeds, and faster heating rates during the sintering process, also has a positive effect on the osteogenic potential of coated substrates. The substrate used also has an observable effect, with PEEK substrates seemingly increasing ALP activity of Y201 cells. However, the metabolic activity results indicate that cell and/or coating adhesion on these substrates is poor, and a more efficient pre-treatment is necessary for PEEK. When following the optimal coating conditions, more material is deposited in Ti-6Al-4V substrates, with coating thickness being ≈ 2.7 times larger compared to PEEK substrates. Overall, the thin coating layers deposited have larger surface roughness and area compared to their uncoated counterparts, results that are further enhanced when replacing Mg-enriched HAP with the optimal sHAP developed during Chapter VI. It is expected, then, that both the composition and surface morphology of the developed coatings will positively impact the osteointegration of the coated substrates, although more studies are still necessary to fully understand their biological performance.

IX. Summary and Future Work

This thesis explored the development of osteoinductive coatings based TiO_2/HAP sol-gel composite. The objective was to develop a coating capable of improving the osteointegration of spine fusion cages and, consequently improve the post-operative period and outcome of spine fusion surgery. The plan was to first develop a protocol for serum-free culture of immortalised MSCs which would eliminate the most common sources of variability in *in vitro* assays. Then, it was studied the synthesis conditions for both HAP and TiO_2 which improve their individual biologic performance. The final step combined all previous results to find the optimal coating conditions which lead to the osteogenic differentiation of MSCs.

In the end, the aim of this project was achieved. One commercially available SFM was found to be ideal for the expansion of Y201 cells, an immortalised MSC line. It was also found that Y201 culture can be kept for up to 21 days with just one full media change every week, and Y201 cells start showing signs of osteogenic differentiation in 14 days. At least two HAP formulations were found to inducing MSC differentiation, significantly outperforming a commercially available solution. It was also found that, by carefully tuning the sol-gel reaction process, it was possible to lower the crystallisation temperature of TiO_2 from ≈400°C to 250°C. As crystallised TiO_2 has been found to further enhance osteointegration compared to its amorphous counterpart [57, 58], this strategy allowed PEEK substrates to be coated with crystallised TiO_2 using simple and cost-effective methods. Finally, not only was it possible to obtain TiO_2/HAP coatings that were capable to increase the osteogenic potential of both Ti-6Al-4V and PEEK, the two materials most used in fusion cages, using DoE the optimal coating conditions for both conditions were found.

It is important to mention that opportunities for further research were found for all steps took during this thesis. Starting with the serum-free protocol for *in vitro* testing, it is important to see if the same culture conditions used in Y201 cells can be transferred to cells from a primary source. While CD1 was also found to enhance the

expansion of primary MSCs, these tests were conducted for only 7 days, and with full media changes every 2 or 3 days. Because primary cells are more representative of *in vivo* conditions [81], it will be important to assess the biological performance of any of the developed materials using this kind of cells. Furthermore, because cells sourced from different individuals can behave differently to the same culture conditions [76, 78], it will be important to see if these testing conditions can be applied to MSCs from different donors.

In the case of the substituted hydroxyapatite, three different pathways were identified. The first one is to expand the full factorial DoE used in this study to a central composite design. Considering that the DoE model for ALP activity showed signs of curvature (see Equation 18 and Figure 44 in Chapter VI), using a design capable of calculating quadratic effects would be more indicated for optimising the synthesis process. At the same time, considering the antibacterial effects that Sr is shown to possess [187, 188], it would be interesting to study how the sHAP formulations developed during this thesis impact bacterial growth. Finally, it could be of interest to study the potential to develop patient-specific sHAP formulations using DoE and the patient's own MSCs, as this personalised strategy could further improve surgery outcome.

Three possible routes were identified to expand the study of sol-gel TiO_2. To start, it would be interesting to study the cytotoxicity of the TiO_2 samples developed for the DoE, similarly to how it was studied for sHAP. If none of the TiO_2 samples are shown to not affect metabolic activity, this could potentially indicate it is possible to further optimise the crystallinity of TiO_2 without worrying about organic residues still being present after sintering, potentially increasing the biologic performance of the developed coatings. On the same note, it would be of interest to directly compare how the optimal TiO_2 compares to amorphous TiO_2 and TiO_2 sintered at 400°C, both in morphology and on the osteogenic differentiation of MSCs. Finally, it would be interesting to study if the crystallisation temperature of TiO_2 could be further reduced, allowing for the sol-gel dip coating of crystallised TiO_2 on a larger range of materials.

As for the TiO_2/HAP coatings, it will be necessary to study how the optimal coating conditions found using DoE perform *in vitro*, as well as how biological performance is affected when replacing the Mg-enriched HAP used during the DoE analysis with sHAP C6-, the best performing sHAP developed during this thesis. Furthermore, it is important to study the mechanical performance of the developed coatings, including their adhesion strength to the implant, to see if they are indeed viable options. It is also necessary to improve coating adhesion to PEEK, as the air-plasma treatment seemingly did not prevent the detachment of the deposited material. The solution could pass through polishing PEEK before treatment, as done by other researchers who successfully used air-plasma to improve coating adhesion to PEEK [133, 135, 171]. Finally, it would be of interest to compare the developed coatings to commercially available solutions, to better understand if the solution developed during this research is indeed a more viable and cost-effective alternative to what is already on the market.

Bibliography

1. Cieza, A., et al., Global estimates of the need for rehabilitation based on the Global Burden of Disease study 2019: a systematic analysis for the Global Burden of Disease Study 2019. Lancet, 2020. 396(10267): p. 2006-2017.

2. Years Lived with Disability, in Handbook of Disease Burdens and Quality of Life Measures, V.R. Preedy and R.R. Watson, Editors. 2010, Springer New York: New York, NY. p. 4354-4355.

3. Sebbag, E., et al., The world-wide burden of musculoskeletal diseases: a systematic analysis of the World Health Organization Burden of Diseases Database. Annals of the Rheumatic Diseases, 2019. 78(6): p. 844-848.

4. Disability Adjusted Life Years (DALYs)Disability adjusted life years (DALYs), in Encyclopedia of Public Health, W. Kirch, Editor. 2008, Springer Netherlands: Dordrecht. p. 267-268.

5. Organization, W.H., Global health estimates 2020: disease burden by cause, age, sex, by country and by region, 2000–2019. 2020, Geneva.

6. Abbafati, C., et al., Global burden of 369 diseases and injuries in 204 countries and territories, 1990-2019: a systematic analysis for the Global Burden of Disease Study 2019. Lancet, 2020. 396(10258): p. 1204-1222.

7. Maher, C., M. Underwood, and R. Buchbinder, Non-specific low back pain. Lancet, 2017. 389(10070): p. 736-747.

8. Lee, H., et al., How does pain lead to disability? A systematic review and meta-analysis of mediation studies in people with back and neck pain. Pain, 2015. 156(6): p. 988-997.

9. Airaksinen, O., et al., Chapter 4. European guidelines for the management of chronic nonspecific low back pain. European spine journal : official publication of the European Spine Society, the European Spinal Deformity Society, and the European Section of the Cervical Spine Research Society, 2006. 15 Suppl 2(Suppl 2): p. S192-S300.

10. Jain, S., et al., Advances in Spinal Interbody Cages. Orthopaedic Surgery, 2016. 8(3): p. 278-284.

11. Phan, K. and R.J. Mobbs, Evolution of Design of Interbody Cages for Anterior Lumbar Interbody Fusion. Orthopaedic Surgery, 2016. 8(3): p. 270-277.

12. Kersten, R., et al., Polyetheretherketone (PEEK) cages in cervical applications: a systematic review. Spine Journal, 2015. 15(6): p. 1446-1460.

13. Talia, A.J., et al., Comparison of the different surgical approaches for lumbar interbody fusion. Journal of Clinical Neuroscience, 2015. 22(2): p. 243-251.

14. Rao, P.J., et al., Spine Interbody Implants: Material Selection and Modification, Functionalization and Bioactivation of Surfaces to Improve Osseointegration. Orthopaedic Surgery, 2014. 6(2): p. 81-89.

15. Bakkum, B.W., Chapter 1 - Surface Anatomy of the Back and Vertebral Levels of Clinically Important Structures, in Clinical Anatomy of the Spine, Spinal Cord, and Ans (Third Edition), G.D. Cramer and S.A. Darby, Editors. 2014, Mosby: Saint Louis. p. 1-14.

16. Urits, I., et al., Low Back Pain, a Comprehensive Review: Pathophysiology, Diagnosis, and Treatment. Current Pain and Headache Reports, 2019. 23(3).

17. Knezevic, N.N., et al., Low back pain. Lancet, 2021. 398(10294): p. 78-92.

18. Hartvigsen, J., et al., What low back pain is and why we need to pay attention. Lancet, 2018. 391(10137): p. 2356-2367.

19. Bagby, G.W., ARTHRODESIS BY THE DISTRACTION-COMPRESSION METHOD USING A STAINLESS-STEEL IMPLANT. Orthopedics, 1988. 11(6): p. 931-934.

20. Kuslich, S.D., et al., The Bagby and Kuslich method of lumbar interbody fusion - History, techniques, and 2-year follow-up results of a United States prospective, multicenter trial. Spine, 1998. 23(11): p. 1267-1278.

21. Lowery, G.L., Titanium surgical mesh for vertebral defect replacement and intervertebral spacers. Manual of internal fixation of the spine, 1996.

22. Ray, C.D., Threaded fusion cages for lumbar interbody fusions - An economic comparison with 360 degrees fusions. Spine, 1997. 22(6): p. 681-685.

23. Cain, C.M.J., et al., A new stand-alone anterior lumbar interbody fusion device: Biomechanical comparison with established fixation techniques. Spine, 2005. 30(23): p. 2631-2636.

24. Aesculap and B. Brawn. Interbody Fusion. [cited 2019 26th June 2019]; Available from: https://www.bbraun.com/en/products-and-therapies/degenerative-spinal-disorders/interbody-fusion.html.

25. Branemar.Pi, et al., REGENERATION OF BONE MARROW - A CLINICAL AND EXPERIMENTAL STUDY FOLLOWING REMOVAL OF BONE MARROW BY CURETTAGE. Acta Anatomica, 1964. 59(1-2): p. 1-&.

26. Navarro, M., et al., Biomaterials in orthopaedics. Journal of the Royal Society Interface, 2008. 5(27): p. 1137-1158.

27. Ma, R. and T.T. Tang, Current Strategies to Improve the Bioactivity of PEEK. International Journal of Molecular Sciences, 2014. 15(4): p. 5426-5445.

28. Grasmeder, J. A Closer Peek at PEEK – HPP explained (part 2). 2017 28 June 2019]; Available from: https://www.victrex.com/en/blog/2017/a-closer-peek-at-peek.

29. Van der Vegt, A.K. and L.E. Govaert, Polymeren. Tc, 2005. 186: p. 75.

30. El-Qoubaa, Z. and R. Othman, Tensile Behavior of Polyetheretherketone over a Wide Range of Strain Rates. International Journal of Polymer Science, 2015.

31. Seaman, S., et al., Titanium vs. polyetheretherketone (PEEK) interbody fusion: Meta-analysis and review of the literature. Journal of Clinical Neuroscience, 2017. 44: p. 23-29.

32. Lingutla, K., et al., Radiological outcomes of Peek vs Titanium transforaminal lumbar interbody cages. The Spine Journal, 2015. 15(3): p. S53.

33. Chen, Y., et al., Comparison of titanium and polyetheretherketone (PEEK) cages in the surgical treatment of multilevel cervical spondylotic myelopathy: a

prospective, randomized, control study with over 7-year follow-up. European Spine Journal, 2013. 22(7): p. 1539-1546.

34. Niu, C.C., et al., Outcomes of Interbody Fusion Cages Used in 1 and 2-levels Anterior Cervical Discectomy and Fusion Titanium Cages Versus Polyetheretherketone (PEEK) Cages. Journal of Spinal Disorders & Techniques, 2010. 23(5): p. 310-316.

35. Meier, U. and D. Kemmesies, Erfahrungen mit 6 verschiedenen intervertebrodiskalen Spacern zur Spondylodese der Halswirbelsäule. Der Orthopäde, 2004. 33(11): p. 1290-1299.

36. Aesculap and B. Brawm, Interbody Fusion: Implants with PEEK core and Plasmapore XP ® titanium coating. p. 15.

37. Lee, J.H., et al., Cold-spray coating of hydroxyapatite on a three-dimensional polyetheretherketone implant and its biocompatibility evaluated by in vitro and in vivo minipig model. Journal of Biomedical Materials Research Part B-Applied Biomaterials, 2017. 105(3): p. 647-657.

38. Almasi, D., et al., In Vitro Evaluation of Bioactivity of Chemically Deposited Hydroxyapatite on Polyether Ether Ketone. International Journal of Biomaterials, 2015: p. 5.

39. Asri, R.I.M., et al., A review of hydroxyapatite-based coating techniques: Sol-gel and electrochemical depositions on biocompatible metals. Journal of the Mechanical Behavior of Biomedical Materials, 2016. 57: p. 95-108.

40. Paital, S.R. and N.B. Dahotre, Calcium phosphate coatings for bio-implant applications: Materials, performance factors, and methodologies. Materials Science & Engineering R-Reports, 2009. 66(1-3): p. 1-70.

41. Narayanan, R., et al., Calcium phosphate-based coatings on titanium and its alloys. Journal of Biomedical Materials Research Part B-Applied Biomaterials, 2008. 85B(1): p. 279-299.

42. Arts, M.P., J.F.C. Wolfs, and T.P. Corbin, Porous silicon nitride spacers versus PEEK cages for anterior cervical discectomy and fusion: clinical and

radiological results of a single-blinded randomized controlled trial. European Spine Journal, 2017. 26(9): p. 2372-2379.

43. Zhang, B.G.X., et al., Bioactive Coatings for Orthopaedic Implants-Recent Trends in Development of Implant Coatings. International Journal of Molecular Sciences, 2014. 15(7): p. 11878-11921.

44. de Grado, G.F., et al., Bone substitutes: a review of their characteristics, clinical use, and perspectives for large bone defects management. Journal of Tissue Engineering, 2018. 9: p. 18.

45. Suchanek, W. and M. Yoshimura, Processing and properties of hydroxyapatite-based biomaterials for use as hard tissue replacement implants. Journal of Materials Research, 1998. 13(1): p. 94-117.

46. Lin, K. and J. Chang, 1 - Structure and properties of hydroxyapatite for biomedical applications, in Hydroxyapatite (Hap) for Biomedical Applications, M. Mucalo, Editor. 2015, Woodhead Publishing. p. 3-19.

47. Supova, M., Substituted hydroxyapatites for biomedical applications: A review. Ceramics International, 2015. 41(8): p. 9203-9231.

48. Ratnayake, J.T.B., M. Mucalo, and G.J. Dias, Substituted hydroxyapatites for bone regeneration: A review of current trends. Journal of Biomedical Materials Research Part B-Applied Biomaterials, 2017. 105(5): p. 1285-1299.

49. Finceramica and T. Holding. Sintlife: moldable bone substitute. [cited 2019 2nd June 2019].

50. Boanini, E., M. Gazzano, and A. Bigi, Ionic substitutions in calcium phosphates synthesized at low temperature. Acta Biomaterialia, 2010. 6(6): p. 1882-1894.

51. Vahabzadeh, S., et al., Phase stability and biological property evaluation of plasma sprayed hydroxyapatite coatings for orthopedic and dental applications. Acta Biomaterialia, 2015. 17: p. 47-55.

52. Parrino, F., et al., 2 - Properties of titanium dioxide, in Titanium Dioxide (Tio_2) and Its Applications, F. Parrino and L. Palmisano, Editors. 2021, Elsevier. p. 13-66.

53. Hümmelgen, I.A., “Oxide semiconductors for solar energy conversion—titanium dioxide”. Author: Janusz Nowotny. Journal of Solid State Electrochemistry, 2012. 16(6): p. 2287-2287.

54. Liu, Z.Q., X.L. Liu, and S. Ramakrishna, Surface engineering of biomaterials in orthopedic and dental implants: Strategies to improve osteointegration, bacteriostatic and bactericidal activities. Biotechnology Journal, 2021. 16(7).

55. Prodana, M., et al., Innovative Coatings of Metallic Alloys Used as Bioactive Surfaces in Implantology: A Review. Coatings, 2021. 11(6).

56. Priyadarshini, B., et al., Bioactive coating as a surface modification technique for biocompatible metallic implants: a review. Journal of Asian Ceramic Societies, 2019. 7(4): p. 397-406.

57. Bencina, M., et al., Crystallized TiO(2)Nanosurfaces in Biomedical Applications. Nanomaterials, 2020. 10(6).

58. He, J., et al., The anatase phase of nanotopography titania plays an important role on osteoblast cell morphology and proliferation. Journal of Materials Science-Materials in Medicine, 2008. 19(11): p. 3465-3472.

59. Djaoued, Y., et al., Study of Anatase to Rutile Phase Transition in Nanocrystalline Titania Films. Journal of Sol-Gel Science and Technology, 2002. 24(3): p. 255-264.

60. Baszczuk, A., M. Jasiorski, and M. Winnicki, Low-Temperature Transformation of Amorphous Sol-Gel TiO2 Powder to Anatase During Cold Spray Deposition. Journal of Thermal Spray Technology, 2018. 27(8): p. 1551-1562.

61. Danks, A.E., S.R. Hall, and Z. Schnepp, The evolution of 'sol-gel' chemistry as a technique for materials synthesis. Materials Horizons, 2016. 3(2): p. 91-112.

62. Schubert, U., Chemistry and Fundamentals of the Sol–Gel Process. The Sol-Gel Handbook, 2015.

63. Kumar, D., et al., Hydrophobic sol-gel coatings based on polydimethylsiloxane for self-cleaning applications. Materials & Design, 2015. 86: p. 855-862.

64. Dadsetan, M., et al., Effect of hydrogel porosity on marrow stromal cell phenotypic expression. Biomaterials, 2008. 29(14): p. 2193-2202.

65. Dawson, E.R., et al., Increased Internal Porosity and Surface Area of Hydroxyapatite Accelerates Healing and Compensates for Low Bone Marrow Mesenchymal Stem Cell Concentrations in Critically-Sized Bone Defects. Applied Sciences-Basel, 2018. 8(8): p. 11.

66. Ramires, P.A., et al., The influence of titania/hydroxyapatite composite coatings on in vitro osteoblasts behaviour. Biomaterials, 2001. 22(12): p. 1467-1474.

67. Advincula, M.C., et al., Osteoblast adhesion and matrix mineralization on sol-gel-derived titanium oxide. Biomaterials, 2006. 27(10): p. 2201-2212.

68. Tranquillo, E. and F. Bollino, Surface Modifications for Implants Lifetime extension: An Overview of Sol-Gel Coatings. Coatings, 2020. 10(6).

69. Kim, H.-W., et al., Hydroxyapatite and titania sol–gel composite coatings on titanium for hard tissue implants; Mechanical and in vitro biological performance. Journal of Biomedical Materials Research Part B: Applied Biomaterials, 2005. 72B(1): p. 1-8.

70. Amaravathy, P., et al., Bioactive HA/TiO2 coating on magnesium alloy for biomedical applications. Ceramics International, 2014. 40(5): p. 6617-6630.

71. Milella, E., et al., Preparation and characterisation of titania/hydroxyapatite composite coatings obtained by sol-gel process. Biomaterials, 2001. 22(11): p. 1425-1431.

72. Yun, Y.J., et al., Low-temperature coating of sol-gel anatase thin films. Materials Letters, 2004. 58(29): p. 3703-3706.

73. Kondalkar, V.V., et al., Microwave-assisted rapid synthesis of highly porous TiO2 thin films with nanocrystalline framework for efficient photoelectrochemical conversion. Electrochimica Acta, 2014. 143: p. 89-97.

74. Andrade-Guel, M., et al., Microwave assisted sol–gel synthesis of titanium dioxide using hydrochloric and acetic acid as catalysts. Boletín de la Sociedad Española de Cerámica y Vidrio, 2019. 58(4): p. 171-177.

75. Shimizu, K., et al., Low-temperature synthesis of anatase thin films on glass and organic substrates by direct deposition from aqueous solutions. 2nd International Conference on Coatings on Glass, Iccg: High-Performance Coatings for Transparent Systems in Large-Area and/or High-Volume Applications, 1999: p. 323-327.

76. Miron, R.J. and Y.F. Zhang, Osteoinduction: A Review of Old Concepts with New Standards. Journal of Dental Research, 2012. 91(8): p. 736-744.

77. Friedenstein, A.J., et al., HETEROTOPIC TRANSPLANTS OF BONE MARROW - ANALYSIS OF PRECURSOR CELLS FOR OSTEOGENIC AND HEMATOPOIETIC TISSUES. Transplantation, 1968. 6(2): p. 230-+.

78. Vemuri, M.C., L.G. Chase, and M.S. Rao, Mesenchymal Stem Cell Assays and Applications, in Mesenchymal Stem Cell Assays and Applications, M. Vemuri, L.G. Chase, and M.S. Rao, Editors. 2011, Humana Press: Totowa, NJ. p. 3-8.

79. Placencio, V.R., et al., Bone Marrow Derived Mesenchymal Stem Cells Incorporate into the Prostate during Regrowth. Plos One, 2010. 5(9).

80. Primary Culture. Culture of Animal Cells, 2010: p. 163-186.

81. Stacey, G., Primary Cell Cultures and Immortal Cell Lines. eLS, 2006.

82. Ramakrishnan, A., B. Torok-Storb, and M.M. Pillai, Primary Marrow-Derived Stromal Cells: Isolation and Manipulation. Stem Cell Niche: Methods and Protocols, 2013. 1035: p. 75-101.

83. James, S., et al., Multiparameter Analysis of Human Bone Marrow Stromal Cells Identifies Distinct Immunomodulatory and Differentiation-Competent Subtypes. Stem Cell Reports, 2015. 4(6): p. 1004-1015.

84. Subculture and Cell Lines. Culture of Animal Cells, 2010: p. 187-206.

85. Kaur, G. and J.M. Dufour, Cell lines: Valuable tools or useless artifacts. Spermatogenesis, 2012. 2(1): p. 1-5.

86. McGillicuddy, N., et al., Examining the sources of variability in cell culture media used for biopharmaceutical production. Biotechnology Letters, 2018. 40(1): p. 5-21.

87. Gottipamula, S., et al., Serum-free media for the production of human mesenchymal stromal cells: a review. Cell Proliferation, 2013. 46(6): p. 608-627.

88. Shanbhag, S., et al., Efficacy of Humanized Mesenchymal Stem Cell Cultures for Bone Tissue Engineering: A Systematic Review with a Focus on Platelet Derivatives. Tissue Engineering Part B-Reviews, 2017. 23(6): p. 552-569.

89. Karnieli, O., et al., A consensus introduction to serum replacements and serum-free media for cellular therapies. Cytotherapy, 2017. 19(2): p. 155-169.

90. Eriksson, L., et al., Design of experiments. Principles and Applications, Learn ways AB, Stockholm, 2000.

91. Design and Analysis of Experiments: Sections 2.1–2.2, in Design of Experiments in Chemical Engineering. 2004. p. 157-262.

92. Kleijnen, J.P.C., et al., A user's guide to the brave new world of designing simulation experiments. Informs Journal on Computing, 2005. 17(3): p. 263-289.

93. Weissman, S.A. and N.G. Anderson, Design of Experiments (DoE) and Process Optimization. A Review of Recent Publications. Organic Process Research & Development, 2015. 19(11): p. 1605-1633.

94. Moser, S., Effective Run-In and Optimization of an Injection Molding Process. Some Critical Issues for Injection Molding, 2012: p. 33.

95. Jones, B. and C.J. Nachtsheim, A Class of Three-Level Designs for Definitive Screening in the Presence of Second-Order Effects. Journal of Quality Technology, 2011. 43(1): p. 1-15.

96. Xiao, L.L., D.K.J. Lin, and F.S. Bai, Constructing Definitive Screening Designs Using Conference Matrices. Journal of Quality Technology, 2012. 44(1): p. 2-8.

97. Jones, B. and C.J. Nachtsheim, Effective Design-Based Model Selection for Definitive Screening Designs. Technometrics, 2017. 59(3): p. 319-329.

98. Jones, B. and C. Nachtsheim, Definitive Screening Designs, in Wiley StatsRef: Statistics Reference Online. p. 1-6.

99. Pituch, K.A. and J.P. Stevens, Applied Multivariate Statistics for the Social Sciences: Analyses with SAS and IBM‘s SPSS. 6th Edition ed. 2015: Routledge.

100. Tarpey, T., A note on the prediction sum of squares statistic for restricted least squares. American Statistician, 2000. 54(2): p. 116-118.

101. Haasters, F., et al., Morphological and immunocytochemical characteristics indicate the yield of early progenitors and represent a quality control for human mesenchymal stem cell culturing. J Anat, 2009. 214(5): p. 759-67.

102. Melke, J., Environmental stimuli for controlled bone tissue engineering applications. 2019, Eindhoven University of Technology. p. 172.

103. Haack-Sorensen, M., et al., Mesenchymal Stromal Cell Phenotype is not Influenced by Confluence during Culture Expansion. Stem Cell Reviews and Reports, 2013. 9(1): p. 44-58.

104. Bhat, S., et al., Expansion and characterization of bone marrow derived human mesenchymal stromal cells in serum-free conditions. Scientific Reports, 2021. 11(1).

105. Ullah, I., R.B. Subbarao, and G.J. Rho, Human mesenchymal stem cells - current trends and future prospective. Bioscience Reports, 2015. 35.

106. Trivedi, S., et al., A quantitative method to determine osteogenic differentiation aptness of scaffold. Journal of Oral Biology and Craniofacial Research, 2020. 10(2): p. 158-160.

107. Qassim, D.A., BONE TISSUE ENGINEERING FOR CORRECTING OF CLEFT PALATE DURING ORAL AND MAXILLOFACIAL SURGERY. 2021, University of Sheffield.

108. PromoCell, Mesenchymal Stem Cell Media - Instruction Manual. 2018. p. 2.

109. Samavedi, S., A.R. Whittington, and A.S. Goldstein, Calcium phosphate ceramics in bone tissue engineering: A review of properties and their influence on cell behavior. Acta Biomaterialia, 2013. 9(9): p. 8037-8045.

110. Zhang, Z.W., J.D. Wang, and X.Y. Lu, An integrated study of natural hydroxyapatite-induced osteogenic differentiation of mesenchymal stem cells using transcriptomics, proteomics and microRNA analyses. Biomedical Materials, 2014. 9(4).

111. Landi, E., et al., Synthetic biomimetic nanostructured hydroxyapatite. Bioceramics 17, 2005. 284-286: p. 949-952.

112. Kolodziejska, B., N. Stepien, and J. Kolmas, The Influence of Strontium on Bone Tissue Metabolism and Its Application in Osteoporosis Treatment. International Journal of Molecular Sciences, 2021. 22(12).

113. Reginster, J.Y., Cardiac concerns associated with strontium ranelate. Expert Opinion on Drug Safety, 2014. 13(9): p. 1209-1213.

114. Curtis, E.M., C. Cooper, and N.C. Harvey, Cardiovascular safety of calcium, magnesium and strontium: what does the evidence say? Aging Clinical and Experimental Research, 2021. 33(3): p. 479-494.

115. Rehman, I. and W. Bonfield, Characterization of hydroxyapatite and carbonated apatite by photo acoustic FTIR spectroscopy. Journal of Materials Science-Materials in Medicine, 1997. 8(1): p. 1-4.

116. Berry, E.E. and C.B. Baddiel, INFRA-RED SPECTRUM OF DICALCIUM PHOSPHATE DIHYDRATE (BRUSHITE). Spectrochimica Acta Part a-Molecular Spectroscopy, 1967. A 23(7): p. 2089-&.

117. Ham, D., et al., Effect of pH on the Structure of Calcium Phosphate Crystals Synthesized using a Hydrothermal Process. Journal of the Korean Physical Society, 2019. 75(7): p. 514-518.

118. Al-Qasas, N.S. and S. Rohani, Synthesis of pure hydroxyapatite and the effect of synthesis conditions on its yield, crystallinity, morphology and mean particle size. Separation Science and Technology, 2005. 40(15): p. 3187-3224.

119. Vinogradoff, V., et al., THERMAL EVOLUTION OF INTERSTELLAR ICE ANALOGUES CONTAINING FORMALDEHYDE. Ecla: European Conference on Laboratory Astrophysics, 2013. 58: p. 337-+.

120. El-Ghannam, A. and P. Ducheyne, 1.109 - Bioactive Ceramics, in Comprehensive Biomaterials, P. Ducheyne, Editor. 2011, Elsevier: Oxford. p. 157-179.

121. Bates, R.G., V.E. Bower, and E.R. Smith, CALCIUM HYDROXIDE AS A HIGHLY ALKALINE PH STANDARD. Journal of Research of the National Bureau of Standards, 1956. 56(6): p. 305-312.

122. Danks, A.E., et al., Mechanistic insights into the formation of porous carbons from gelatin. Journal of Materials Chemistry A, 2017. 5(23): p. 11644-11651.

123. Magnesium chloride hexahydrate. [cited 2022 15-09-2022]; Available from: https://www.merckmillipore.com/GB/en/product/Magnesium-chloride-hexahydrate,MDA_CHEM-102367.

124. Prathap Padappayil , R. and J. Borger Ammonia Toxicity. 2022 [cited 2022 15-09-2022]; Available from: https://www.ncbi.nlm.nih.gov/books/NBK546677/.

125. Zhao, Z., et al., Ion-doping as a strategy to modulate hydroxyapatite nanoparticle internalization. Nanoscale, 2016. 8(3): p. 1595-1607.

126. Mehrjoo, M., et al., Effect of magnesium substitution on structural and biological properties of synthetic hydroxyapatite powder. Materials Express, 2015. 5(1): p. 41-48.

127. Shannon, R.D., REVISED EFFECTIVE IONIC-RADII AND SYSTEMATIC STUDIES OF INTERATOMIC DISTANCES IN HALIDES AND CHALCOGENIDES. Acta Crystallographica Section A, 1976. 32(SEP1): p. 751-767.

128. Geng, Z., et al., Synthesis, characterization and biological evaluation of strontium/magnesium-co-substituted hydroxyapatite. Journal of Biomaterials Applications, 2016. 31(1): p. 140-151.

129. Huynh, V., N.K. Ngo, and T.D. Golden, Surface Activation and Pretreatments for Biocompatible Metals and Alloys Used in Biomedical Applications. International Journal of Biomaterials, 2019. 2019.

130. Xue, T., et al., Surface Modification Techniques of Titanium and its Alloys to Functionally Optimize Their Biomedical Properties: Thematic Review. Frontiers in Bioengineering and Biotechnology, 2020. 8.

131. Peltola, T., et al., Effect of aging time of sol on structure and in vitro calcium phosphate formation of sol-gel-derived titania films. Journal of Biomedical Materials Research, 2000. 51(2): p. 200-208.

132. Areva, S., et al., Use of sol-gel-derived titania coating for direct soft tissue attachment. Journal of Biomedical Materials Research Part A, 2004. 70A(2): p. 169-178.

133. Shimizu, T., et al., Bioactivity of sol-gel-derived TiO2 coating on polyetheretherketone: In vitro and in vivo studies. Acta Biomaterialia, 2016. 35: p. 305-317.

134. Parker, D., et al., Polymers, High-Temperature, in Ullmann's Encyclopedia of Industrial Chemistry.

135. Kizuki, T., T. Matsushita, and T. Kokubo, Apatite-forming PEEK with TiO2 surface layer coating. Journal of Materials Science-Materials in Medicine, 2015. 26(1): p. 9.

136. Amano, N., et al., Transferability and Adhesion of Sol-Gel-Derived Crystalline TiO2 Thin Films to Different Types of Plastic Substrates. Langmuir, 2017. 33(4): p. 947-953.

137. Yang, Y.J., et al., Enhancement of bioactivity on medical polymer surface using high power impulse magnetron sputtered titanium dioxide film. Materials Science & Engineering C-Materials for Biological Applications, 2015. 57: p. 58-66.

138. Tsou, H.K., et al., Improved osteoblast compatibility of medical-grade polyetheretherketone using arc ionplated rutile/anatase titanium dioxide films for spinal implants. Journal of Biomedical Materials Research Part A, 2012. 100A(10): p. 2787-2792.

139. Anatase R060277. [cited 2022 19-10-2022]; Available from: https://rruff.info/Anatase/R060277.

140. Shahramian, K., et al., Sol-gel derived bioactive coating on zirconia: Effect on flexural strength and cell proliferation. Journal of Biomedical Materials Research Part B-Applied Biomaterials, 2017. 105(8): p. 2401-2407.

141. Rossi, S., et al., Comparison between sol-gel-derived anatase- and rutile-structured TiO2 coatings in soft-tissue environment. Journal of Biomedical Materials Research Part A, 2007. 82A(4): p. 965-974.

142. Shimizu, T., et al., In vivo experimental study of anterior cervical fusion using bioactive polyetheretherketone in a canine model. Plos One, 2017. 12(9): p. 13.

143. Hayashi, M., et al., Optimizing the layer thickness of sol-gel-derived TiO2 coating on polyetheretherketone. Scientific Reports, 2021. 11(1).

144. Simonsen, M.E., Z.S. Li, and E.G. Sogaard, Influence of the OH groups on the photocatalytic activity and photoinduced hydrophilicity of microwave assisted sol-gel TiO2 film. Applied Surface Science, 2009. 255(18): p. 8054-8062.

145. Wu, Y.C. and Y.C. Tai, Effects of alcohol solvents on anatase TiO2 nanocrystals prepared by microwave-assisted solvothermal method. Journal of Nanoparticle Research, 2013. 15(6).

146. Wiranwetchayan, O., et al., Effect of alcohol solvents on TiO2 films prepared by sol-gel method. Surface & Coatings Technology, 2017. 326: p. 310-315.

147. John, A.K. and S. Palaty, Influence of solvent and pH on the synthesis of visible light active titanium dioxide nano particles. Journal of Sol-Gel Science and Technology, 2018. 87(2): p. 391-399.

148. Alphonse, P., A. Varghese, and C. Tendero, Stable hydrosols for TiO2 coatings. Journal of Sol-Gel Science and Technology, 2010. 56(3): p. 250-263.

149. Grinter, D.C., M. Nicotra, and G. Thornton, Acetic Acid Adsorption on Anatase TiO2(101). Journal of Physical Chemistry C, 2012. 116(21): p. 11643-11651.

150. Liao, L.F., C.F. Lien, and J.L. Lin, FTIR study of adsorption and photoreactions of acetic acid on TiO2. Physical Chemistry Chemical Physics, 2001. 3(17): p. 3831-3837.

151. Robert, D., F. Rohr, and J.V. Weber, Influence of some factors on the photocatalytic degradation of acetic acid in an aqueous suspension of TiO2. Comptes Rendus De L Academie Des Sciences Serie Ii Fascicule B-Mecanique Physique Astronomie, 1997. 325(12): p. 733-738.

152. Heintz, O., D. Robert, and J.V. Weber, Comparison of the degradation of benzamide and acetic acid on different TiO2 photocatalysts. Journal of Photochemistry and Photobiology a-Chemistry, 2000. 135(1): p. 77-80.

153. Dai, Z., et al., Sterilization techniques for biodegradable scaffolds in tissue engineering applications. Journal of Tissue Engineering, 2016. 7.

154. Quan, Y.L., Photodegradation and Mineralization of Acetic Acid by Titanium Dioxide Films. Proceedings of the 2015 2nd International Conference on Machinery, Materials Engineering, Chemical Engineering and Biotechnology (Mmeceb), 2016. 49: p. 613-616.

155. Leyva-Porras, C., et al., Low-temperature synthesis and characterization of anatase TiO2 nanoparticles by an acid assisted sol-gel method. Journal of Alloys and Compounds, 2015. 647: p. 627-636.

156. Muniz-Serrato, O. and J. Serrato-Rodriguez, Nanostructuring anatase through the addition of acetic acid by the sol gel low temperature aqueous processing. Ceramics International, 2014. 40(6): p. 8631-8635.

157. Pagacova, J., et al., The influence of "small molecules" on crystallization of TiO2 xerogels. 20th International Conference Machine Modeling and Simulations, Mms 2015, 2016. 136: p. 280-286.

158. Uchiyama, H. and T. Bando, Water-assisted crystallization and densification of sol-gel-derived TiO2 films during low-temperature heating. Journal of Asian Ceramic Societies, 2022. 10(1): p. 253-261.

159. Terabe, K., et al., MICROSTRUCTURE AND CRYSTALLIZATION BEHAVIOR OF TIO(2) PRECURSOR PREPARED BY THE SOL-GEL METHOD USING METAL ALKOXIDE. Journal of Materials Science, 1994. 29(6): p. 1617-1622.

160. Rymuszka, D., et al., Time-dependent changes of surface properties of polyether ether ketone caused by air plasma treatment. Polymer International, 2016. 65(7): p. 827-834.

161. Colovic, B., et al., Wetting properties of titanium oxides, oxynitrides and nitrides obtained by DC and pulsed magnetron sputtering and cathodic arc evaporation. Materials Science-Poland, 2019. 37(2): p. 173-181.

162. Son, Y., M.K. Lee, and Y.C. Park, Contact Angle Relaxation on Amorphous, Mixed-Phase (Anatase plus Rutile), and Anatase TiO2 Films and Its Mechanism. Langmuir, 2021. 37(5): p. 1850-1860.

163. Rad, A.T., et al., Improved bio-physical performance of hydroxyapatite coatings obtained by electrophoretic deposition at dynamic voltage. Ceramics International, 2014. 40(8): p. 12681-12691.

164. Aronov, D., et al., Tunable hydroxyapatite wettability: Effect on adhesion of biological molecules. Process Biochemistry, 2006. 41(12): p. 2367-2372.

165. Zhao, D.P., et al., Macro-micron-nano-featured surface topography of Ti-6Al-4V alloy for biomedical applications. Rare Metals, 2018. 37(12): p. 1055-1063.

166. Kadhim, M.A., et al., Experimental and Theoretical Investigation of Droplet Evaporation on Heated Hydrophilic and Hydrophobic Surfaces. Langmuir, 2019. 35(19): p. 6256-6266.

167. Shi, J.Z., et al., Application of magnetron sputtering for producing bioactive ceramic coatings on implant materials. Bulletin of Materials Science, 2008. 31(6): p. 877-884.

168. Lu, Y.P., et al., Plasma-sprayed hydroxyapatite plus titania composite bond coat for hydroxyapatite coating on titanium substrate. Biomaterials, 2004. 25(18): p. 4393-4403.

169. Terpilowski, K. and D. Rymuszka, Surface properties of glass plates activated by air, oxygen, nitrogen and argon plasma. Glass Physics and Chemistry, 2016. 42(6): p. 535-541.

170. Pizzorni, M., et al., Effect of process gases in vacuum plasma treatment on adhesion properties of titanium alloy substrates. International Journal of Adhesion and Adhesives, 2018. 86: p. 113-122.

171. Jama, C., et al., TREATMENT OF POLY(ETHER ETHER KETONE) (PEEK) SURFACES BY REMOTE PLASMA DISCHARGE - XPS INVESTIGATION OF THE AGING OF PLASMA-TREATED PEEK. Surface and Interface Analysis, 1992. 18(11): p. 751-756.

172. Wyrwoll, A.J., et al., Size matters - The phototoxicity of TiO2 nanomaterials. Environmental Pollution, 2016. 208: p. 859-867.

173. Kim, I.Y., et al., Titanium Dioxide Induces Apoptosis under UVA Irradiation via the Generation of Lysosomal Membrane Permeabilization-Dependent Reactive Oxygen Species in HaCat Cells. Nanomaterials, 2021. 11(8).

174. Jimenez-Becerril, J., A. Moreno-Lopez, and M. Jimenez-Reyes, Radiocatalytic degradation of dissolved organic compounds in wastewater. Nukleonika, 2016. 61(4): p. 473-476.

175. Hoertz, P.G., et al., Photocatalytic and radiocatalytic nanomaterials for the degradation of organic species. Radiation Physics and Chemistry, 2013. 84: p. 51-58.

176. Olivares-Navarrete, R., et al., Osteoblasts exhibit a more differentiated phenotype and increased bone morphogenetic protein production on titanium alloy substrates than on poly-ether-ether-ketone. Spine Journal, 2012. 12(3): p. 265-272.

177. Torstrick, F.B., et al., Do Surface Porosity and Pore Size Influence Mechanical Properties and Cellular Response to PEEK? Clinical Orthopaedics and Related Research, 2016. 474(11): p. 2373-2383.

178. You, C.K., S. Oh, and S. Kim, Influences of heating condition and substrate-surface roughness on the characteristics of sol-gel-derived hydroxyapatite coatings. Journal of Sol-Gel Science and Technology, 2001. 21(1-2): p. 49-54.

179. Li, X.Z., et al., Effects of titanium surface roughness on the mediation of osteogenesis via modulating the immune response of macrophages. Biomedical Materials, 2018. 13(4).

180. Keddie, J.L. and E.P. Giannelis, EFFECT OF HEATING RATE ON THE SINTERING OF TITANIUM-DIOXIDE THIN-FILMS - COMPETITION BETWEEN DENSIFICATION AND CRYSTALLIZATION. Journal of the American Ceramic Society, 1991. 74(10): p. 2669-2671.

181. Lotz, E.M., et al., Osteogenic response of human MSCs and osteoblasts to hydrophilic and hydrophobic nanostructured titanium implant surfaces. Journal of Biomedical Materials Research Part A, 2016. 104(12): p. 3137-3148.

182. Kwon, Y.S. and J.W. Park, Osteogenic differentiation of mesenchymal stem cells modulated by a chemically modified super-hydrophilic titanium implant surface. Journal of Biomaterials Applications, 2018. 33(2): p. 205-215.

183. Laudone, G., G. Matthews, and P.A.C. Gane, Coating shrinkage during evaporation: Observation, measurement and modelling within a network structure. TAPPI Advanced Coating Fundamentals Symposium, 2003: p. 191-208.

184. Surmenev, R.A., M.A. Surmeneva, and A.A. Ivanova, Significance of calcium phosphate coatings for the enhancement of new bone osteogenesis - A review. Acta Biomaterialia, 2014. 10(2): p. 557-579.

185. Wang, B.C., et al., THE SHEAR-STRENGTH AND THE FAILURE MODE OF PLASMA-SPRAYED HYDROXYAPATITE COATING TO BONE - THE EFFECT OF COATING THICKNESS. Journal of Biomedical Materials Research, 1993. 27(10): p. 1315-1327.

186. Mohseni, E., E. Zalnezhad, and A.R. Bushroa, Comparative investigation on the adhesion of hydroxyapatite coating on Ti-6Al-4V implant: A review paper. International Journal of Adhesion and Adhesives, 2014. 48: p. 238-257.

187. Baheiraei, N., et al., Effects of strontium ions with potential antibacterial activity on in vivo bone regeneration. Scientific Reports, 2021. 11(1).

188. Ravi, N.D., R. Balu, and T.S.S. Kumar, Strontium-Substituted Calcium Deficient Hydroxyapatite Nanoparticles: Synthesis, Characterization, and Antibacterial Properties. Journal of the American Ceramic Society, 2012. 95(9): p. 2700-2708.